RESEARCH REPORT DOCUMENTATION PAGE

1. Report No.	2. Report Date	3. Contract No.	4. Project No.
UND 21-03	June, 2023	91211002	

5. Title and Subtitle	6. Report Type	7. Project No.
Generating Binder and Mixture Inputs in Pavement ME for North Dakota's Conditions.	Work Plan ☐ Construction ☐ Evaluation ☐ Final ☒	8. Project No. 9. Project No. 10. Project No.

11. Author(s)/Principle Investigator(s)
Dr. Duncan Oteki, Dr. Dabe Gedafe, Dr. Nabil Suleiman

12. Performing Organization Name and Address	13. Sponsoring Agency Name and Address
NDDOT M+R ☐ NDDOT OTHER* ☐ NDSU ☐ UND ☒ UGPTI ☐ OTHER* ☐ *see supplementary notes North Dakota DOT Materials and Research Division 300 Airport Road Bismarck ND 58504-6005	North Dakota DOT Materials and Research Division 300 Airport Road Bismarck ND 58504-6005

14. Supplementary Notes

15. Abstract

Objective

The main goal of this study was to provide binder and asphalt mix input parameters to facilitate the implementation of Pavement ME in North Dakota.

Scope

This goal was achieved by sampling ten asphalt mixtures and binders typically used in the region. Asphalt binder rheological tests were conducted using the dynamic shear rheometer (DSR): the complex shear modulus (|G*|) and phase angle (δ), multiple creep stress recovery (MSCR) test, and linear amplitude sweep (LAS) test. Binder viscosity was also determined at 1350C. Asphalt mixture tests included the dynamic moduli (|E*|) test, flow number (FN) test, incremental repeated loading permanent deformation (iRLPD) test, and simplified viscoelastic continuum damage (SVECD) test. Prediction models and interconversion procedures were also used to estimate dynamic modulus and creep compliance [D(t)].

Summary

All the binders performed satisfactorily according to their binder grading; however, binders with the same performance grades displayed varying |G*| values, illustrating the importance of local binder characterization. A good agreement was observed between measured and predicted |G*| values for all binders (R2>0.9). Some binders displayed a poor agreement between measured and predicted δ values. Generating local A and VTS parameters X was recommended. There was a poor agreement between the binder grading results and the MSCR and LAS results, which needs further investigation.

This study evaluated the dynamic modulus (|E*|) of asphalt mixes across various temperatures (40°C–350°C) and loading frequencies (0.01–10Hz), comparing lab results with predictions from the Witczak, modified Witczak, and Hirsch models. The Witczak model showed the highest accuracy (R^2 > 0.9) but tended to over-predict |E*| at low temperatures and under-predict at high ones. Rutting resistance was assessed using Flow Number (FN) and iRLPD tests at 54°C, with HWY 35_PG58S-28 showing the best performance and HWY 28_PG58S-28 the worst. Fatigue cracking was evaluated using the S-VECD test at 12°C, revealing that mixes with higher stiffness had lower fatigue resistance, with HWY 35 and HWY 32 being most susceptible. Creep compliance [D(t)] was derived from |E*| data to support thermal cracking predictions in pavement design.

16. Key Words	17. Distribution Statement	18. No. of Pages	19. File type/Size
Pavement Me Design(MEPDG), Asphalt mixtures, Asphalt Binders, Local Calibration, Performance Grading, PG Binder grades, RAP, ESALs	No restrictions. This document is available to the public from: North Dakota Department of Transportation Materials and Research Division: 300 Airport Road Bismarck ND 58504-6005 Office: (701) 328-6900	91	Pdf/ 0.5mb

UNIVERSITY OF NORTH DAKOTA
Grand Forks

Generating Binder and Mixture Inputs in Pavement ME for North Dakota's Conditions

Final Report

June 02, 2023

Civil Engineering Department
College of Engineering

University of North Dakota
Department of Civil Engineering

Generating Binder and Mixture Inputs in Pavement ME for North Dakota's Conditions

Draft Final Report Submitted to the

North Dakota Department of Transportation
Bismarck, ND

By:

Duncan Oteki, Ph.D. Student
Andebut Yeneneh, MS
Dr. Daba Gedafa, Principal Investigator
Dr. Nabil Suleiman, Co-Principal Investigator

June 02, 2023

Disclaimer

The contents of this report reflect the views of the authors who are responsible for the facts and accuracy of the data presented herein. The contents do not reflect the official views of the North Dakota Department of Transportation or the Federal Highway Administration. This report does not constitute a standard, specification, or regulation.

ACKNOWLEDGMENT

The authors appreciate the funding provided by the NDDOT, which made this research study possible. They also wish to thank the Materials and Research Division staff for sampling and delivering the materials and for their valuable insights.

TABLE OF CONTENTS

List of Figures

List of Tables

EXECUTIVE SUMMARY

The main goal of this study was to provide binder and asphalt mix input parameters to facilitate the implementation of Pavement ME in North Dakota. This goal was achieved by sampling ten asphalt mixtures and binders typically used in the region. Asphalt binder rheological tests were conducted using the dynamic shear rheometer (DSR): the complex shear modulus (|G*|) and phase angle (δ), multiple creep stress recovery (MSCR) test, and linear amplitude sweep (LAS) test. Binder viscosity was also determined at 135^0C. Asphalt mixture tests included the dynamic moduli (|E*|) test, flow number (FN) test, incremental repeated loading permanent deformation (iRLPD) test, and simplified viscoelastic continuum damage (SVECD) test. Prediction models and interconversion procedures were also used to estimate dynamic modulus and creep compliance [D(t)].

The binder properties were measured at unaged, short-term aged, and long-term aged conditions. Short-term aging was simulated using the Rolling Thin Film Oven (RTFO) followed by measuring |G*| and phase angle values, which are required inputs in levels 1 and 2 of the Mechanistic-Empirical Pavement Design Guide (MEPDG). Viscosity was measured at all three aging conditions; the results are provided in this report. The modified ASTM Ai-VTSi model was used to predict |G*| and δ values. MSCR and LAS tests were also conducted to rank the binders according to their rutting and fatigue cracking resistance.

All the binders performed satisfactorily according to their binder grading; however, binders with the same performance grades displayed varying |G*| values, illustrating the importance of local binder characterization. A good agreement was observed between measured and predicted |G*| values for all binders (R^2>0.9). Some binders displayed a poor agreement between measured and predicted δ values. Generating local A and VTS parameters

was recommended. There was a poor agreement between the binder grading results and the MSCR and LAS results, which needs further investigation.

|E*| testing was conducted at 4^0C, 21^0C, and 35^0C, and the loading frequencies were 0.01Hz, 0.1Hz, 1Hz, and 10Hz. Master curves were developed to extrapolate the measured |E*| data over a wider range of temperatures and loading frequencies. Pavement projects have varying reliability requirements, and laboratory experiments are costly and time-intensive; therefore, this study investigated the effectiveness of using existing models to predict |E*|. The Witczak, modified Witczak, and Hirsch models were used to predict |E*| values at the same conditions as the laboratory tests. |E*| predictions showed that the Witczak model performed better than the other two with R^2 values above 0.9 and low standard error values for the ten asphalt mixes. However, the Witczak model over-predicted and under-predicted |E*| values at low and high temperatures, respectively.

FN tests were conducted at an elevated temperature of 54^0C to rank the mixes according to their rutting resistances. iRLPD tests were conducted at 54^0C combined with a 69 kPa confining pressure. Results from the FN, |E*|, and iRLPD tests were compared. HWY 35 with binder grade PG 58S-28 had the highest |E*|values at slow loading frequencies, indicating better rutting resistance at elevated temperatures. In contrast, I-94 with PG58H-34 had the lowest |E*| values at fast loading frequencies, indicating better fatigue cracking resistance at low temperatures. FN results indicated that HWY 32 with binder grade PG58H-34 had the highest FN value at 348, meaning it can withstand traffic loads between 10 to <30 million Equivalent Single Axle Loads (ESALs). The iRLPD test results corroborated the FN test results by revealing that HWY 28_PG58S-28_0%RAP and HWY 6_PG58S-34_20%RAP exhibited high rutting susceptibility, while HWY 32_PG58H-34_15%RAP and HWY 35_PG58S-34_20%RAP exhibited the best rutting performance.

Fatigue cracking was characterized using the simplified viscoelastic continuum damage model *(*S-VECD*)* test. Testing was conducted at a temperature of 12^0C and a loading frequency of 10Hz for eight mixes. Damage characteristic curves were developed to illustrate the relationship between material integrity (C) and damage (S). The results reveal that asphalt mixes that displayed a higher stiffness from earlier dynamic modulus testing had higher material integrity at failure. Out of the eight mixes tested, HWY 35_PG58S-34_20%RAP and HWY 32_PG58S-28_15%RAP were more susceptible to fatigue cracking.

The interconversion procedure developed from earlier studies was used to obtain creep compliance [D(t)] from measured |E*| data, thus providing MEPDG input data that can be used to predict the mixes' resistance to thermal cracking

Chapter One - Introduction

1.1 General

There is a wide consensus that the mechanistic-empirical (ME) approach to designing pavement structures is an improvement from the earlier empirical-based design approaches; however, important implementation challenges remain. One of them is the lack of comprehensive material input databases for bound and unbound layers. Developing such databases requires extensive laboratory tests, which are usually costly and time-consuming for state highway agencies (SHAs). The effective implementation of the ME design approach requires the characterization of properties for typical binders and hot mix asphalt (HMA) mixes used in a particular region. This exercise will be a vital step toward the application of the ME design approach in North Dakota.

1.2 Problem Statement

The American Association of State Highway Officials (AASHO) conducted road tests in Ottawa, Illinois, in the late 1950s to establish a fair tax system for different vehicle classes based on fuel usage. AASHTO used the test section's data and performance history to develop the 1972 AASHO design guide. The organization then updated its guides into its1986 and 1toAmerican Association of State Highway and Transportation Officials (AASHTO) guides for the design of pavement structures. The design equations adopted in the 1993 design guide are based on the original AASHO road test conditions. The experimental nature of these equations is a major limitation since fundamental material properties are not considered. Additionally, the AASHO road tests were conducted under single climatic conditions and subgrade types of Ottawa City, with materials specifications, mixture designs, and traffic inputs bounded to Illinois and 1950s engineering practice. The National Cooperative Highway Research Program (NCHRP) project 1-37A was initiated to address these limitations by developing a new pavement design guide for new and rehabilitated pavements. This guide defines the use

of mechanistic–empirical (ME) methods that consider specific conditions predominant at the road site and related to the fundamental material properties used in construction.

Adopting the ME approach signals a significant shift in pavement design. The ME approach's capacity to directly estimate key pavement performance indicators that affect user comfort and ride quality while providing the scientific rationale behind pavement deterioration makes it an effective tool that can ensure strong, durable, reliable, safe, and comfortable pavements. Libraries of level 1 inputs must be developed by state highway agencies (SHAs) for typical binder and HMA mixes before this procedure can be successfully adopted.

1.3 Purpose/Outcome

This study aimed to develop Level 1 libraries of inputs for typical binders and HMA mixes in North Dakota. The database and designated pavement sections will be used to calibrate and validate Pavement ME for North Dakota's conditions. There are three levels of input in Pavement ME. Level 1, which is the most accurate, involves measuring the properties of asphalt binders and mixes in controlled laboratory conditions. A combination of laboratory-determined and predicted mix and binder properties are used at Level 2. Predicted and default values are used at Level 3, which is the least accurate. Prediction models that provide estimated properties comparable to laboratory binder and mix test results were recommended for future use to reduce the number of laboratory tests.

1.4 Proposed Innovation

The main objective of this project was to develop a database for typical binders and HMA mixes used in North Dakota.

- Evaluate the viscosity, complex modulus, and phase angle data at 10 rad/sec for the binders used in typical HMA mixes in North Dakota.
- Estimate dynamic shear modulus, phase angle, and viscosity of binders in the mixes and compare them to laboratory test results.

- Evaluate the effectiveness of Linear Amplitude Sweep (LAS) and Multiple Sweep Creep Recovery (MSCR) tests in measuring fatigue cracking and rutting resistance, respectively.
- Determine the dynamic modulus, rutting resistance using flow number and incremental repeated load permanent deformation (iRLPD), and a number of cycles until fatigue failure for typical HMA mixes in North Dakota.
- Predict dynamic modulus based on the volumetric properties of the mixes and compare them to laboratory dynamic modulus to select the best model.
- Use interconversion procedures to determine creep compliance (D[t]) from the laboratory dynamic modulus.

1.5 Report Organization

The research approach used to achieve the specified objectives is described under four different tasks. Each task is described in the following sections. The following discussion presents a literature review on important elements of binders and HMA mixes that were evaluated during this project.

Chapter Two- Literature Review

2.1 Binder Properties

Asphalt binder properties are key in governing the mechanical performance of asphalt concrete, making its characterization an important requirement in the ME design approach (Yu & Shen, 2013). Asphalt binder is categorized as a thermoplastic material that displays linear viscoelastic (LVE) behaviour under in-service pavement operating conditions (Dondi et al., 2014). The LVE properties of asphalt binders are usually presented in the form of both the complex modulus |G*| and the phase angle (δ), which are measurements of the relationship between stress and strain of the binder under varying temperatures and loading times (Dondi et al., 2014). These two parameters are indicators of the susceptibility of the asphalt binder to rutting and fatigue under these varying conditions. Viscosity is another important property of the asphalt binder that indicates its pumpability, workability, and mixability, all of which are integral in producing desirable asphalt concrete.

2.1.1 Viscosity

The viscosity of an asphalt binder indicates the behaviour of asphalt concrete during production and construction. Specifically, the viscosity of the asphalt binder governs the pumpability, mixability, and workability of an asphalt mix (Colbert & You, 2012).

The viscosity of an asphalt binder can be measured in the laboratory through various techniques; however, the rotational viscometer was preferred due to its advantages in measuring the viscosity of materials that display viscoelastic properties, such as asphalt binders (Colbert & You, 2012). The viscosity of original, RTFO-aged, and PAV-aged binders following AASHTO T 316-19 (AASHTO, 2019).

2.1.2 Complex Modulus |G*| and Phase Angle (δ)

|G*| is a parameter that indicates a binder's resistance to deformation; as defined by Eq. 2-1:

$$|G^*| = \frac{\tau_{Max}}{Max} \tag{2-1}$$

where τ_{Max} is the absolute value of the peak-to-peak shear stress and γ_{Max} is the absolute value of the peak-to-peak shear strain (Dondi et al., 2014). The phase angle (δ) is the time lag (Δt) between the applied shear stress and the resulting shear strain converted into degrees (Eq. 2-2):

$$\delta = \frac{\Delta t}{t} .360 \tag{2-2}$$

where t is the loading time.

Studies have emphasized the importance of the |G*| and δ values in providing early indications of the strength and durability of the asphalt mix to be produced (Dondi et al., 2014; Yusoff et al., 2011; Li et al., 2019), and others. The general agreement is that these two parameters are key inputs in the application of the ME pavement design approach and, therefore, need to be determined during the earlier stages of the design.

|G*| and δ values can be determined using laboratory experiments, experimental regression equations, or numerical simulations (Yu & Shen, 2013). Level 1 library inputs need to be measured; therefore, laboratory experiments were carried out to determine the |G*| and δ values of the sample asphalt binders provided by the NDDOT. The dynamic shear rheometer (DSR) is the recommended equipment for determining the viscoelastic properties of an asphalt binder because of its ability to measure |G*| and δ values under varying temperatures and frequencies (Yusoff et al., 2011). The DSR test was used to measure the |G*| and δ values

according to AASHTO T315 for level 1 and 2 inputs (Li et al., 2019). A-VTS viscosity-temperature susceptibility parameters were determined for level 3 inputs.

2.1.3 Prediction of Viscosity, Complex Shear Modulus, and Phase Angle

The MEPDG uses asphalt binder viscosity as a primary input parameter in all three hierarchical input levels (Bari & Witczak, 2007). The ASTM A_i-VTS_i viscosity model (Eq. 2-3) is used to obtain the design viscosity when applying the MEPDG. The model relates the binder's absolute viscosity to the temperature in the Rankine scale as shown:

$$loglog(\eta) = A + VTS.\log(T_R) \quad (2\text{-}3)$$

where,

η= viscosity (cP),

T_R= temperature (degree Rankine),

A= regression intercept, and

VTS= regression slope (viscosity-temperature susceptibility parameter).

For levels 1 and 2, binder characterization data measured in the laboratory are converted to viscosity and fitted into the model using statistical regression methods (Bari & Witczak, 2007). For level 3, the MEPDG uses default A and VTS values to estimate binder viscosity. Overall, the MEPDG procedure adopts a constant binder viscosity at varying loading frequencies which is inaccurate, especially at low to intermediate temperature ranges (Bari & Witczak, 2007).

Bari and Witczak (2007) developed a modified version of the ASTM Ai-VTSi model considering the effect of loading frequency on viscosity. By using two frequency adjustment factors the regression intercept A and the slope VTS were modified for loading frequency and

introduced into Eq. 2-3. The modified ASTM A_i-VTS_i equation (Eq. 2-4) was thus presented in its final form as follows:

$$loglog\ \eta_{f_{s,T}} = c_0 f_s^{c_1} xA + d_0 f_s^{d_1} xVTS.\log(T_R) \quad (2\text{-}4)$$

where,

$\eta_{fs,\,T}$= viscosity of asphalt binder as a function of both loading frequency (f_s) and temperature (T), (cP);

f_s= loading frequency in dynamic shear modulus as used in the G_b^* testing (H_z);

A= regression intercept from the conventional ASTM A_i -VTS_i equation (Equation 2-3);

VTS= regression slope (viscosity-temperature susceptibility parameter) (Equation 2-3);

c_0 and c_1 = frequency adjustment factor for A, functions of f_s and T;

d_0 and d_1 = frequency adjustment factor for VTS, functions of f_s and T; and

T_R= temperature (degree Rankine)

Apart from the modified ASTM A_i -VTS_i model, Bari and Witczak (2007) developed two other models: one for estimating the binder's shear modulus (|Gb*|), and the other for estimating the associated phase angle (δb). The final forms of the models are presented as Eqs. 2-5 and 2-6 respectively:

$$|G_b^*| = 0.0051 f_s \eta_{f_{s,T}} (sin\delta)^{7.1542 - 0.4929 f_s + 0.0211 f_s^2} \quad (2\text{-}5)$$

where,

$|G_b^*|$= dynamic shear modulus (Pa),

f_s= dynamic shear loading frequency to be used with $|G_b^*|$ and δ_b (Hz),

$\eta_{fs,T}$= viscosity of asphalt binder as a function of both loading frequency (f_s) and temperature (T), (cP),

δ_b= phase angle (deg).

$$\delta_b = 90 + (b_1 + b_2 VTS')x log\left(f_s x \eta_{f_{s,}T}\right) + (b_3 + b_4 VTS')x\{\log\left(f_s x \eta_{f_s T}\right)\}^2 \qquad (2\text{-}6)$$

where,

δ_b= phase angle (deg),

f_s= dynamic shear loading frequency to be used with $|G_b^*|$ and δ_b (Hz),

VTS'= adjusted VTS,

$\eta_{fs,\,T}$= viscosity of asphalt binder as a function of both loading frequency (f_s) and temperature (T), (cP),

b_1, b_2, b_3, and b_4 = fitting parameters = -7.3146, -2.6162, 0.1124, and 0.2029.

Eqs. 2-4, 2-5, and 2-6 have shown the capability to predict binder characteristics accurately. The revised ASTM Ai–VTSi viscosity model was used to forecast binder viscosity, dynamic shear modulus, and associated phase angle at specific temperatures and loading frequencies.

2.2 Rutting

Rutting is a type of pavement distress that manifests as a depression along the wheelpath of an asphalt pavement and is likely to occur under repeated heavy traffic loading coupled with high temperatures (Figure 2.1). Binder stiffness plays a significant role in rutting resistance, and its characterization helps select the suitable binder corresponding to a region's traffic and environmental loading (Wang et al., 2021).

Figure 2.1: Rutting Distress in Asphalt Pavements (Wang et al., 2021).

2.2.1 Binder Grading for Rutting Resistance

A rutting-resistant asphalt binder is characterized by stiffness and elasticity, which enables it to resist deformation while rebounding to its original shape. The |G*|/sinδ is a parameter obtained from binder rheological testing that indicates the stiffness and elastic components of the asphalt binder. Eq. 2-7 depicts an interpretation of the |G*|/sinδ parameter where rutting is viewed as a resultant of cyclic loading. The work done to deform the asphalt pavement is partly regained by the elastic rebound of the pavement and partly dissipated by rutting. The |G*|/sinδ parameter should be maximized to minimize rutting (Yao et al., 2012).

$$W_c = \pi\sigma_0^2 \left[1/(\frac{G^*}{\sin\delta})\right] \quad (2\text{-}7)$$

where,

W_c = work dissipated per load cycle,

σ = stress applied during load cycle,

G^* = complex modulus,

δ = phase angle.

Superpave PG system specifies a minimum threshold value for |G*|/sinδ at 1.0 kPa and 2.2 kPa for unaged and RTFO-aged asphalt binders, respectively (AASHTO, 2020a).

2.2.2 Multiple Stress Creep Recovery (MSCR) Test

Researchers have revealed that the |G*|/sinδ parameter is inaccurate in grading the high-temperature performance of modified asphalt binders (Zeiada et al., 2022; D'Angelo et al., 2007) resulting in the development of the multiple stress creep recovery (MSCR) test, which employs the creep and recovery model to examine the binder's ability to resist permanent deformation. The DSR is used to apply a 1s creep load to the binder specimen, followed by a 9s recovery period. Figure 2.2 illustrates the typical behavior during the MSCR testing cycle. Testing commences by applying a low stress 0.1 kPa for 10 creep/recovery cycles, which is later raised to 3.2 kPa and repeated for an additional 10 cycles.

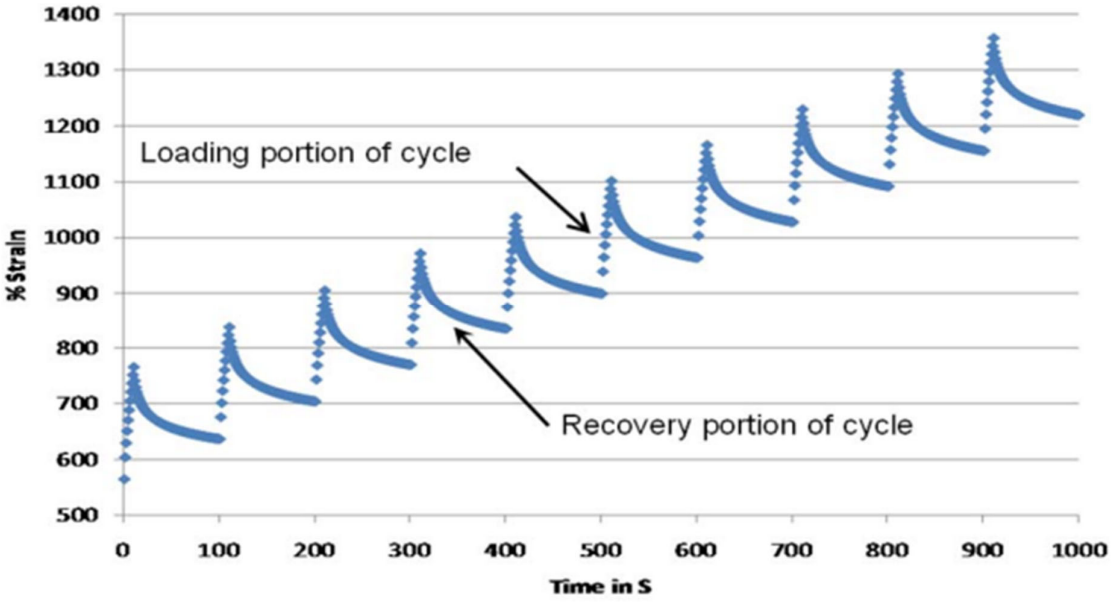

Figure 2.2: Evolution of Shear Strain with Time in the MSCR Test (AASHTO, 2014a).

The MCSR test's primary benefit is subjecting the asphalt binder to higher stress and strain levels compared to the PG test parameter |G*|/sinδ; thereby capturing the stiffening behavior of the binder and delayed elastic effects (Zeiada et al., 2022). The MSCR test parameter "J_{nr}" is termed the non-recoverable creep compliance and is obtained by dividing the residual shear strain at the end of the recovery portion by the applied stress during the creep portion, as shown in Eq. 2-8:

$$J_{nr}(\tau, N) = \frac{\Delta\gamma}{\tau} \quad (2\text{-}8)$$

where,

J_{nr} = non-recovered creep compliance,

τ = creep stress,

$\Delta\gamma$ = residual shear strain.

The MSCR parameter J_{nr} has been shown to be an improved indicator of the rutting response of most binders as compared to |G*|/sinδ. This study evaluated the output of these two rutting indicators and ranked North Dakota's binders accordingly.

2.3 Fatigue Cracking

Fatigue cracking, commonly called alligator cracking, is a type of pavement distress caused by repeated traffic loading. Fatigue cracking is a common phenomenon in thin pavements, where cracking starts at the bottom of the asphalt layer due to higher tensile stresses, which gradually propagate to the top, forming one or multiple longitudinal cracks (Zeiada et al., 2022). This phenomenon is termed "bottom-up" cracking. This continuously repeated loading results in the interconnection of the cracks.

2.3.1 Binder Grading for Fatigue Cracking Resistance

An asphalt binder needs to be elastic and moderately stiff to prevent cracking under repeated loading. The Superpave parameter |G*|. sinδ needs to be minimized to prevent fatigue cracking. Eq. 2-9 shows that the relationship between the work dissipated for every cycle is directly proportional to the |G*|. sinδ parameter. Therefore, to prevent cracking, the |G*|.sinδ parameter needs to be minimized, which will correspondingly reduce the energy dissipated (Hintz & Bahia, 2013).

$$W_c = \pi\varepsilon_0^2[(G^*)(sin\delta)] \quad (2\text{-}9)$$

Superpave specifies a maximum value of 5000 kPa for G*.sinδ values measured from DSR tests conducted on long-term aged asphalt binders.

2.3.2 Linear Amplitude Sweep (LAS) Test

The Superpave G*.sinδ parameter has a disadvantage since it can only evaluate the asphalt binder's fatigue resistance within the viscoelastic range. Therefore, the accurate evaluation of binders that display nonlinearity, especially modified binders, cannot be evaluated using the G*.sinδ parameter. Johnson and Bahia (2010) developed the LAS test, which incorporates the concept of damage accumulation to measure fatigue resistance. The LAS test is performed by applying oscillating shear loads, increasing the strain amplitude, and controlling the strain. The viscoelastic continuum damage (VECD) analyses the results. The analysis is carried out based on fatigue law parameters A and B. These two parameters are model coefficients that depend on asphalt binder properties. Binders with high fatigue resistance display higher A and lower B values. The repetition of cycles to failure is determined using Eq. 2-10, which calculates the fatigue failure of the asphalt binder (Hintz & Bahia, 2013):

$$Nf = A(\gamma max)\, B \tag{2-10}$$

where, Nf measures variation in pavement structure with changing maximum strain γmax. The strain level corresponds to traffic loading. Reports show the binders' predicted fatigue resistance correlates well with fatigue cracking field measurements. The LAS test laid out in AASHTO TP 101 (AASHTO, 2014b) was used in this research to evaluate the fatigue resistance of long-term aged binders and compare the outcome with those from the G*.sinδ parameter.

2.4 Asphalt Mix Properties

Hot mix asphalt (HMA) is a type of asphalt mix that derives its name from the high temperatures (between 300 and 350 ^{0}F) at which it is prepared and placed on site. The

properties of the asphalt binder and aggregates are important factors that affect HMA performance; however, the HMA by itself has unique properties that are related but not identical to the physical properties of its components (Dondi et al., 2014). The determination of HMA properties is key in determining the performance of the asphalt mix when subjected to in-service operating conditions.

An HMA's resistance to rutting and fatigue cracking is a vital performance requirement that should be investigated before using it for road construction. In this project, typical field mixes will be selected to determine the effects of FAA (43 and 45), RAP content (0-25%), binder grade (PG 58S-28, 58H-28, and 58H-34), and aggregate sources on HMA performance. The laboratory dynamic modulus, flow number, and incremental repeated load permanent deformation (iRLPD) will be used to determine the performance of the typical HMA mixes in North Dakota. The discussion that follows provides deeper insight into the significance of these testing methods.

2.4.1 Dynamic Modulus |E*|

The dynamic modulus, |E*|, is a fundamental property that defines the relationship between stress and strain under sinusoidal loading at various temperatures and loading frequencies for linear viscoelastic materials such as asphalt concrete (Brown et al., 2009). |E*| is a key input in all three hierarchical levels of the Pavement ME (AASHTO, 2008) . The dynamic modulus is mathematically defined by Eq. (2-11). Figure 2.3 illustrates typical stress and strain curves during |E*| testing and are defined by Eqs. (2-12) and (2-13):

$$|E^*| = \frac{\sigma_0}{_0} \tag{2-11}$$

$$\sigma = \sigma_0 \sin(\omega t) \tag{2-12}$$

$$\varepsilon = \varepsilon_0 \sin(\omega t - \emptyset) \tag{2-13}$$

where,

σ_0 = applied steady-state stress amplitude,

ε_0 = measured strain amplitude,

ω = angular frequency ($2\pi f$, where f = frequency), and

$\emptyset$ = phase angle in radians ($\omega\Delta t$, where Δt = time lag between stress and strain.

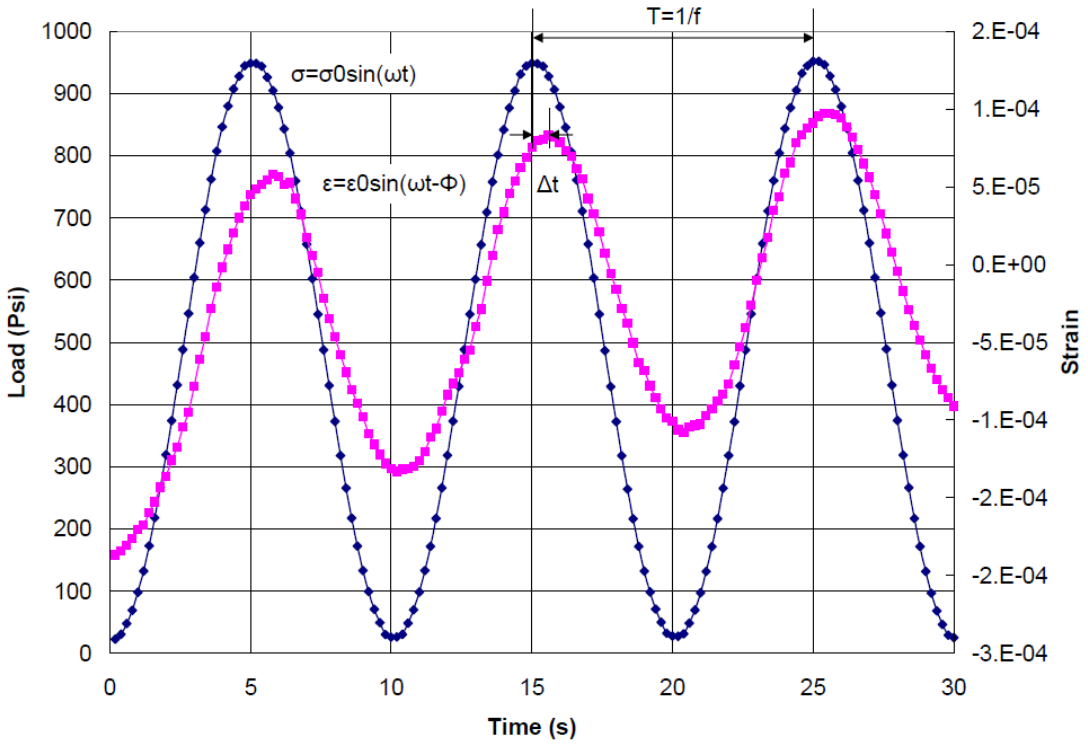

Figure 2.3: Illustration of Typical Stress and Strain Curves in a |E*| Test (Kutay & Jamrah, 2013).

|E*| and $\emptyset$ are two parameters obtained from dynamic modulus testing. $\emptyset$ ranges from zero to 90 degrees with the former indicating a purely elastic material and the latter indicating a purely viscous material. |E*| is a complex number, as shown by Eq. 2-14, that constitutes a real part, storage modulus (E') that can be estimated by Eq. 2-15, and an imaginary part, loss modulus (E") that can be calculated as shown in Eq. 2-16. Figure 2.4 illustrates these two components, which represent the elastic and viscous components of a viscoelastic material, respectively:

$$|E^*| = E' + iE'' \quad (2\text{-}14)$$

$$E' = |E^*|cos(\emptyset) \quad (2\text{-}15)$$

$$E'' = |E^*| + \sin(\emptyset) \quad (2\text{-}16)$$

where,

E' = storage modulus,

E'' = loss modulus, and

i $= \sqrt{-1}$.

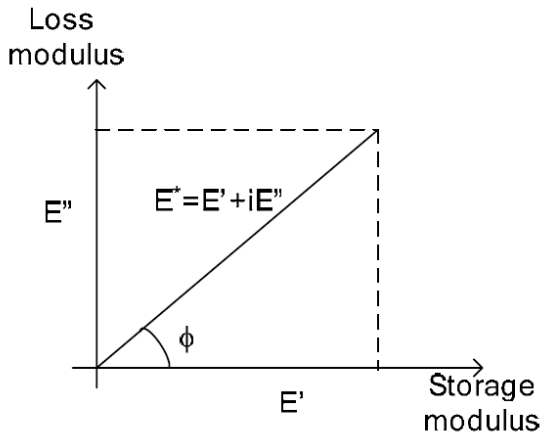

Figure 2.4: Loss and Storage Modulus (Kutay & Jamrah, 2013).

Studies have shown that the |E*| values obtained from laboratory tests correlate well with in-situ permanent deformation and fatigue cracking observed in field test sections (Pellinen, 2001; Al-Khateeb et al., 2006). However, these tests' perceived high cost and time-consuming nature have limited their widespread adoption in the industry. The Strategic Highway Research Program (SHRP) developed the Superpave Shear Tester (SST) as a Simple Performance Tester (SPT) that would correlate well with pavement performance through mechanistic models. However, tests performed using the SST were time-consuming and necessitated developing a more advanced SPT (Diaz & Archilla, 2013).

Reducing the testing time for |E*| tests has been the focus of several studies (Bonaquist, 2008; Bonaquist & Christensen, 2005; Dougan et al., 2003*)*. As a result, the Asphalt Mixture

Performance Tester (AMPT) was developed to conduct |E*| testing under NCHRP Project 9-29 and was widely adopted by the asphalt industry (Bonaquist, 2008). Many agencies have used the AMPTs to develop a catalog for |E*| inputs in the ME design method (Bhasin et al., 2005; Kim et al., 2004; Mohammad et al., 2005; Pellinen, 2001; Williams et al., 2007; Witczak et al., 2002). |E*| tests obtained from the AMPT are within a limited range of temperatures and loading frequencies; therefore, master curves are used to extrapolate the data to capture extreme conditions that are likely to be experienced by field mixes.

2.4.2 Master Curves

The |E*| of HMA is usually characterized over a loading frequency that ranges between 10^{-4} to 10^{4} Hz. However, equipment capacity limits |E*| testing to 25Hz. The time-temperature superposition principle can be used to construct a master curve that extrapolates the limited range of testing frequency. The principle applies to HMA because time and temperature similarly affect its linear viscoelastic properties. The procedure involves shifting the measured |E*| values with respect to the frequency axis to form a sigmoidal curve at a reference temperature, usually 20^{0}C. Pellinen and Witczak (2002) developed a sigmoidal function that can be used to fit the |E*| test data using a regression analysis, and its final form is presented in Eq. 2-17 and Eq. 2-18 for calculating the shift factor. The procedure for selecting |E*| testing temperatures and developing a master curve is laid out in AASHTO R84-17 (AASHTO, 2017b).

$$\log|E^*| = \delta + \frac{(Max- \ )}{1+e^{\beta+\gamma\left(\log f+\frac{\Delta E_a}{19.14714}\left[\left(\frac{1}{T}\right)-\left(\frac{1}{T_r}\right)\right]\right)}} \tag{2-17}$$

$$\log[a(T)] = \frac{\Delta E_a}{19.14714}\left[\left(\frac{1}{T}\right)-\left(\frac{1}{T_r}\right)\right] \tag{2-18}$$

where,

$\log|E^*|$ = log of the dynamic modulus,

δ, β, and γ = the fitting parameters,

Max = the limiting maximum modulus (psi),

$a(T)$ = the shift factor at Temperature T,

ΔE_a = the activation energy,

T = the test temperature (^{0}K),

T_r = the reference temperature (^{0}K).

2.4.3 Predicted dynamic modulus (E^*)

The laboratory dynamic modulus is a mandatory input parameter in level 1 of the MEPDG. More reliability is required at level 1 due to the higher traffic volume subjected to the pavement. In addition, safety and financial considerations for premature failure are a concern in such high-priority pavements. Level 2 requires an intermediate level of accuracy, and the standard of accuracy decreases further at level 3. Undertaking laboratory experiments to determine the dynamic modulus at these two lower levels of design is deemed costly and time-intensive. Instead, predicting the dynamic modulus using models is commonly used to generate inputs in ME design at levels 2 and 3.

Researchers have formulated several dynamic modulus predictive models. The original Witczak, modified Witczak, and Hirsch predictive models were used to predict the dynamic modulus in this project**.**

I. Original Witczak Model

The Witczak predictive equation is a comprehensive model for predicting the dynamic modulus. The Witczak equation utilizes available data from material specifications and data from mix design to predict mixture stiffness under varying temperatures, loading frequency, and aging conditions. Eq. 2-19 was determined from 2750 dynamic modulus measurements obtained from 205 different asphalt mixes measured for more than 30 years. (Andrei et al., 1999):

$$\log|E^*| = 3.750063 + 0.02932_{\rho_{200}} - 0.001767(\rho_{200})^2 - 0.002841_{\rho_4} - 0.058097V_a - 0.802208\left(\frac{V_{beff}}{V_{beff}+V_a}\right) + (3.871977 - 0.0021\rho_4 + 0.003958\rho_{38} - 0.000017(\rho_{38})^2 + 0.00547\rho_{34)}/(1 + e^{(-0.603313-0.313351\log(f)-0.393532\log(\eta))}) \quad (2\text{-}19)$$

where,

|E*| = dynamic modulus, psi

η= bitumen viscosity, 10^6 Poise

f = loading frequency, Hz

V_a = air void content, %

V_{beff} = effective bitumen content, % by volume

ρ_{34} = cumulative % retained on the 19-mm (3/4) sieve

ρ_{38} = cumulative % retained on the 9.5-mm (3/8) sieve

ρ_4 = cumulative % retained on the 4.76-mm (No. 4) sieve

ρ_{200} = % passing the 0.075-mm (No. 200) sieve.

II. Hirsch Model

An existing law of mixtures that blends series and parallel elements of phases to asphalt mixes is the basis of the Hirsch model (Christensen et al., 2003). The equation was based on a database of 18 asphalt mixes with eight different binders, five different aggregate sizes, and gradation. Eqs. 2-20 and 2-21 illustrate the model's use of the dynamic shear modulus of the binder (G_b^*) and the volumetric properties of the mix. The equations are given as follows:

$$|E^*|_{mix} = Pc\left[4{,}200{,}000\left(1 - \frac{VMA}{100}\right) + 3|G^*|_{binder}\left(\frac{(VFA*VMA)}{10{,}000}\right)\right] + (1 - Pc)^*[\frac{1-VMA/100}{4{,}200{,}000} + \frac{VMA}{3*VFA*|G|^*_{binder}}]^{-1} \quad (2\text{-}20)$$

$$Pc = \frac{(20+\frac{VFA*3|G^*|_{binder}}{VMA})^{0.58}}{(650+\frac{VFA*3|G^*|_{binder}}{VMA})^{0.58}} \quad (2\text{-}21)$$

where,

$|E^*|_{mix}$= dynamic modulus of the mixture (psi),

$|G^*|_{binder}$= shear modulus of the binder (psi),

VMA = void in the mineral aggregates (%),

VFA = percent of VMA filled with a binder (%), and

Pc = aggregate contact factor.

The complex shear modulus can be measured in the laboratory or estimated from existing mathematical models. This study used the dynamic shear rheometer (DSR) to measure the |G*| and δ values according to level 1 and 2 inputs. Nationally calibrated A-VTS viscosity-temperature susceptibility parameters were used for estimating |G*| and δ for input level 3.

III. Modified Witczak Model

Bari and Witczak (2006) modified the Witczak (2002) equation to replace viscosity with the dynamic shear modulus ($|G_b|$) and phase angle (δ_b) of the asphalt binder (Eq. 2-22). The modification used a database of 7,400 data points from 346 HMA specimens. The readily available mix design volumetric parameters were maintained from the previous equation. The revised Witczak model is given as:

$$Log_{10}E^* = -0.349 + 0.754(|G_b^*|^{-0.0052})$$

$$x(6.65 - 0.032\rho_{200} + 0.0027\rho_{200}^2 + 0.011\rho_4 - 0.0001\rho_4^2 + 0.006\rho_{38}$$

$$- 0.00014\rho_{38}^2 0.08V_a - 1.06(\frac{V_{beff}}{V_a + V_{beff}}))$$

$$+(2.558 + 0.032V_a + 0.713\,V_{beff}/(V_a + V_{beff}) + 0.0124\rho_{38} - 0.0001\rho_{38}^2 - 0.0098\rho_{34})/$$

$$(1 + e^{(-0.7814 - 0.5785\log|G_b^*| + 0.8834log\ _b)}) \quad (2\text{-}22)$$

The Witczak equation has been shown to overestimate the dynamic modulus at high temperatures according to findings by (Birgisson et al. 2004; Gedafa et al. 2009; Kim et al. 2005; Mohammad et al. 2005; Tran & Hall 2005). The modified Witczak model has displayed comparable results with increasing errors, especially at high or low temperatures (Bari & Witczak, 2006; Ceylan et al., 2009; Gedafa et al., 2009). Evaluations of the Hirsch model have shown that the model under-predicted the dynamic modulus compared with laboratory-measured values

In summary, model performance is essential when using dynamic modulus predictive models. We compared the performance of these three models with laboratory-measured results for North Dakota mixtures to determine one that suited the mixes typical to the region.

2.5 Flow Number (F_N) and Flow Time (F_T) Test Set-Up

The flow number (F_N) and the flow time (F_T) are two of the three tests that make up the simple performance tests (SPTs) recommended by the NCHRP Project 9-19; the other being the dynamic modulus (Witczak et al., 2002). The flow tests are carried out by applying a uniaxial compressive load to a cylindrical HMA specimen that is 100 mm (4 in.) in diameter and 150 mm (6 in.) in height at a temperature of 54°C. For F_N, a repeated compressive haversine loading (1 cycle with 0.1 s loading time and 0.9 s resting time) is applied to the specimen, and the cumulative deformation as a function of the number of load cycles is recorded. For F_T testing, a static compressive load is applied for a maximum of 10,000 seconds or until a deformation of 50,00 macrostrains is reached.

Studies have shown that during uniaxial compression tests, the relationship between loading time (or the number of load applications) and creep compliance displays three phases:

primary flow, secondary flow, and tertiary flow, as shown in Figure 2.5 (Kaloush et al., 2002; Zhou et al., 2004). During the primary flow stage, a decrease in the strain with time is observed. As the repeated load application is continued, the specimen enters the secondary phase, whereby a constant strain is observed. The tertiary flow is the final stage, which displays an increase in strain rate as the test progresses. Tertiary flow is an indication that the specimen is starting to deform considerably and that the individual aggregates in the specimen's matrix are moving past each other. F_N and F_T are based on the onset of tertiary flow.

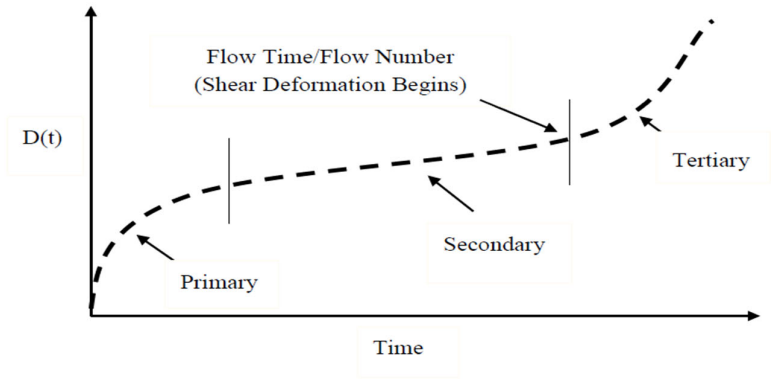

Figure 2.5: Creep compliance vs. time (Williams et al., 2007).

The loading sequence used in the flow number test tries to replicate the loading conditions a pavement is subjected to during operating conditions, making it a suitable indicator of its rutting performance.

2.5.1 Flow Number (F_N) and Flow Time (F_T) Literature Review

Witczak (2002) sought to establish standard performance tests (SPTs) for permanent deformation of HMA mixes. The study involved the collection of HMA mixes from three different locations and carrying out predetermined laboratory tests to determine the rutting resistance of the HMA mixes. The flow number was among the tests under investigation. The flow number parameters exhibited a good correlation with the measured rut depths, with a coefficient of determination, R^2, of 0.9 and above for all test sections except for two. The

discrepancy in the two sites was observed in all test methods undertaken in the study and was attributed to inaccurate reported volumetric properties. The study concluded that the flow number should be adopted as a deformation performance SPT from the overall results.

Bhasin et al. (2005) We used the flow number, flow time, dynamic modulus, and simple shear at constant height (SSCH) to compare the rutting susceptibility of HMA mixtures with APA rut depths and Hamburg rut depths as bases. The flow number and flow time showed a higher correlation with the measured rut depths than other tests. Consequently, these two tests were recommended as suitable for indicating the rutting behavior of HMA mixtures.

Williams et al. (2007) carried out a study of pavements in Wisconsin. They compared HMA pavements designed according to the AASHTO 1972 guidelines and the same ones based on the new mechanistic-empirical pavement design guide (MEPDG). To do so, they first had to obtain the mechanical properties of the HMA mixtures as required by the MEPDG. The dynamic modulus and flow number for 21 field mixtures were measured. The most significant findings from the study are as follows:

1. An increase in air voids in the test specimens decreased the flow number values correspondingly.
2. The nominal maximum aggregate size was a statistically significant factor affecting the flow number values.
3. The flow number value increased with traffic level; this was attributed to the effect of increased aggregate angularity and a decrease in air voids.
4. The 1972 AASHTO Pavement Design Guide provided designs that were able to resist permanent deformation. However, the thicknesses provided by the 1972 guideline were insufficient to resist longitudinal cracking for 3 and 10 million ESAL traffic levels, according to the newer MEPDG.

Bonaquist (2012) undertook a structured study to investigate how the changes in mixture composition affect the flow number. The study also sought to develop flow number criteria for mixtures used at intersections. The first part of the study investigating the effect of changes in asphalt and filler content was conducted by conducting 180 flow number tests on a variation of six mixtures. The second part involved the evaluation of flow numbers for six mixtures to determine their performance at intersections. The noteworthy findings were as follows:

1. Data from the first part of the experiment confirmed that flow numbers consistently decreased with increasing binder content for all mixtures tested. Mixed results were obtained with a variation in filler content, whereby an increase in filler content resulted in an improved rutting resistance. However, for almost half of the mixtures tested, rutting resistance increased with a decrease in filler content.
2. For the second part of the experiment, intersection mixtures with flow numbers 4 to 26 times greater than the rest exhibited good performance. Therefore, it was recommended that flow numbers for intersection mixtures be 6 times greater than those for normal traffic speeds.

Several tests are used to determine the rutting resistance potential of HMA mixes. Researchers investigated the correlation between these tests to find out if one test could be used instead of the others. Zhang et al. (2013) compared the flow number, dynamic modulus, and uniaxial repeated load permanent deformation (RLPD) laboratory tests. Their findings noted that the flow number test ranked highest in terms of its ability to predict the rutting performance of HMA mix designs. In addition, the study demonstrated that unconfined tests such as the ones carried out in their study are unsuitable for permeable friction courses (PFC) mixes. This result was attributed to the high air void content. Confined loading tests were recommended for PFC mixes.

Islam et al. (2019) investigated how sensitive the flow number is to the mix factors in HMA. The flow numbers of 105 specimens from 11 categories of HMA mixes were obtained and analyzed statistically. Their findings showed that the same mix might vary statistically regardless of the contractor. This was attributed to variations in aggregate structures. The variation of air voids between mixes resulted in mixed results, with some HMA mixes exhibiting an increase in flow number with a decrease in air voids, while some mixes exhibited a decrease in the flow number. This was contradictory to the findings of (Williams et al., 2007) and others. Islam et al. (2019) attributed this contradiction in their results to the fact that the air void proportions were between 3% and 6% in their study.

In summary, there is a consensus that F_N and F_T tests are good indicators of the rutting resistance performance of HMA mixes. The flow number has been shown to increase with a decrease in air void and an increase in binder content. Filler has been shown to increase the flow number and improve the rutting resistance performance of an HMA mix. Gradation, temperature, asphalt binder, and air voids are important factors affecting the flow number.

2.6 Incremental Repeated Load Permanent Deformation (iRLPD)

The incremental repeated load permanent deformation (iRLPD) test subjects asphalt mix samples to increasing repetitive cycles at several stresses. The minimum strain rate (MSR) is the test value that represents the permanent strain rate after each test level (Azari & Mohseni, 2013). At the end of the experiment, a set of MSR values at varying stress values is employed to form the MSR master curve(Azari & Mohseni, 2013). The master curve can explain the performance of asphalt mixtures at high temperatures in any climatic and loading conditions.

The iRLPD test has several advantages over the F_N test. The main advantage is that the iRLPD can be executed in a short duration (total testing time of 25 mins) while offering a more comprehensive range of data on the resistance of HMA to permanent deformation (Azari & Mohseni, 2013). The testing protocol for the iRLPD test is identical to the F_N test with respect

to test equipment, specimen fabrication, and load pulse requirements (Azari & Mohseni, 2013). The main difference arises from the fact that the iRLPD test applies a confining pressure and gives variations in the number of loads applied, test parameters, and analysis method. The tests in the research will be conducted according to the guidelines laid out in AASHTO TP 116 (AASHTO, 2020b).

2.7 Fatigue Test

Fatigue cracking is a critical distress that causes rapid deterioration in asphalt pavements. However, cracking in asphalt concrete is challenging to predict since it involves the analysis of complex material and structural factors. A mechanistic model that can simulate the cracking phenomenon of asphalt mixes over a wide range of field conditions will negate the need for conducting many experiments.

Kim and Little (1990) developed the viscoelastic continuum damage (VECD) theory that described the behavior of sand asphalt under controlled strain cyclic loading. Later studies established that a simplified VECD (S-VECD) form can characterize cyclic test results while maintaining mathematical rigor (Underwood et al., 2010). Additionally, linear viscoelastic (LVE) characterization from dynamic modulus tests was found suitable for characterizing the S-VECD model (Underwood et al., 2012). These findings are significant because agencies can use the AMPT to characterize asphalt mixes using the S-VECD model.

2.7.1 S-VECD Model

The damage characteristic curve is a fundamental function of the S-VECD model that provides a relationship between the damage accumulation (S) in a specimen to the pseudostiffness or material integrity (C). C represents the relationship between stress (σ) and pseudo strain (ε^R). An uncracked viscoelastic material exhibits a linear relationship between stress and strain under static loading. This relationship becomes non-linear at the onset of

microcrack damage, which reduces C, as shown in Figure 2.6. The S-VECD model assumes that a decline in C signifies the material's internal damage (Cao et al., 2016). AASHTO TP 107-18 provides the test protocol and computation steps, culminating in developing the damage curve for asphalt mix specimens (AASHTO, 2020c).

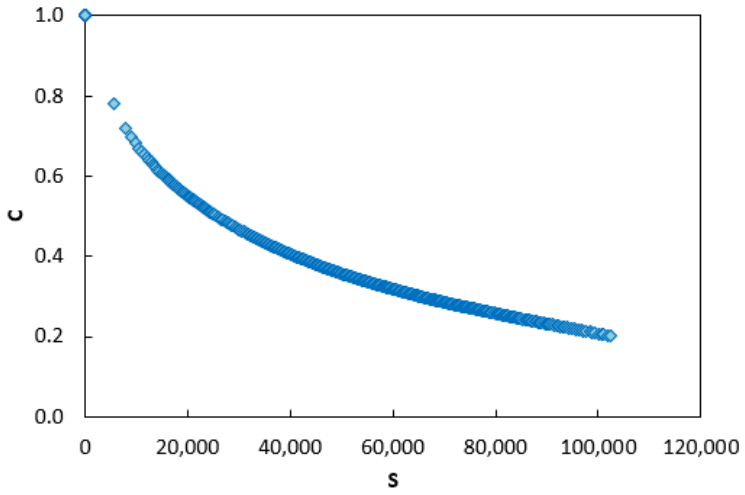

Figure 2.6: Damage Characteristic Curve.

2.8 Thermal Cracking

Thermal cracking is a vital pavement distress in regions with cold climates, such as North Dakota. Asphalt mixes experience extreme thermal contraction when exposed to low temperatures, causing thermal stresses that are higher than the mixture's tensile strength, eventually resulting in transverse cracks that appear at regular intervals on the flexible pavement (Jamrah & Kutay, 2015).

2.8.1 Creep Compliance

Creep is a type of material deformation that occurs when a material is subjected to static loading over time. Creep compliance, $D(t)$, is simply the reciprocal of the modulus of a material as shown by Eq. 2-23. Asphalt mixes display viscoelastic behavior, and creep compliance allows the splitting of its response over time into time-dependent and time-

independent components, making it a better parameter for predicting pavement stresses, strains, and distresses (Witczak et al., 2002):

$$D(t) = \frac{(t)}{\sigma_0} \tag{2-23}$$

where,

$D(t)$ = creep compliance,

t = testing time,

$\varepsilon(t)$ = strain at a given time, and

σ_0 = constant stress.

2.8.2 Relaxation Modulus

When a viscoelastic material is subjected to an instant constant strain, the stress required to maintain that particular strain level reduces over time. This phenomenon is known as stress relaxation, which is computed as the relaxation modulus, $E(t)$, shown in Eq. 2-24:

$$E(t) = \frac{\sigma(t)}{\epsilon_0} \tag{2-24}$$

where,

$E(t)$ = relaxation modulus,

$\sigma(t)$ = stress at a given time, and

ε_0 = instantaneous strain.

$E(t)$ is used to predict thermal stress in asphalt pavements by applying Boltzmann's superposition principle for linear viscoelastic materials.

2.8.3 Interconversion

$D(t)$ can be measured by uniaxial, triaxial, or indirect tensile testing modes. Additionally, studies have shown that $D(t), E(t),$ and $|E^*|$ can be converted to each other analytically since they constitute essentially the same information. This study measured $|E^*|$ values that were later converted to $E(t)$, and then to $D(t)$ using the interconversion method proposed by Park and Schapery (1999).

Eq. 2-25 is an approximate interconversion method that was used in this study to convert $|E^*|$ to $E(t)$. Eq. 2-26 is subsequently used to convert the $E(t)$ to $D(t)$:

$$E(t) \cong \frac{1}{\lambda'} E'(\omega) \tag{2-25}$$

where,

λ' = adjust function ($\Gamma(1-n)\cos(n\pi/2)$),

Γ = gamma function ($\Gamma(n) = \int_0^\infty u^{n-1} e^{-u} du$), and

n = the local log-log slop of the storage modulus $\left(\left|\frac{d \log E'}{d \log}\right|\right)$.

$$E(t)D(t) = \frac{\sin n\pi}{n\pi} \tag{2-26}$$

where,

n = the local log-log slop of the relaxation modulus $\left(\left|\frac{d \log E(t)}{d \log t}\right|\right)$.

Chapter Three- Materials and Methods

3.1 Materials Sampling and Collection

Loose field mixes were collected from ten projects during the summertime, five from 2021 and the other five from 2022. All samples were collected in coordination with the NDDOT materials and research team, district coordinators, and contractors. Figure 3.1 shows the locations of the projects.

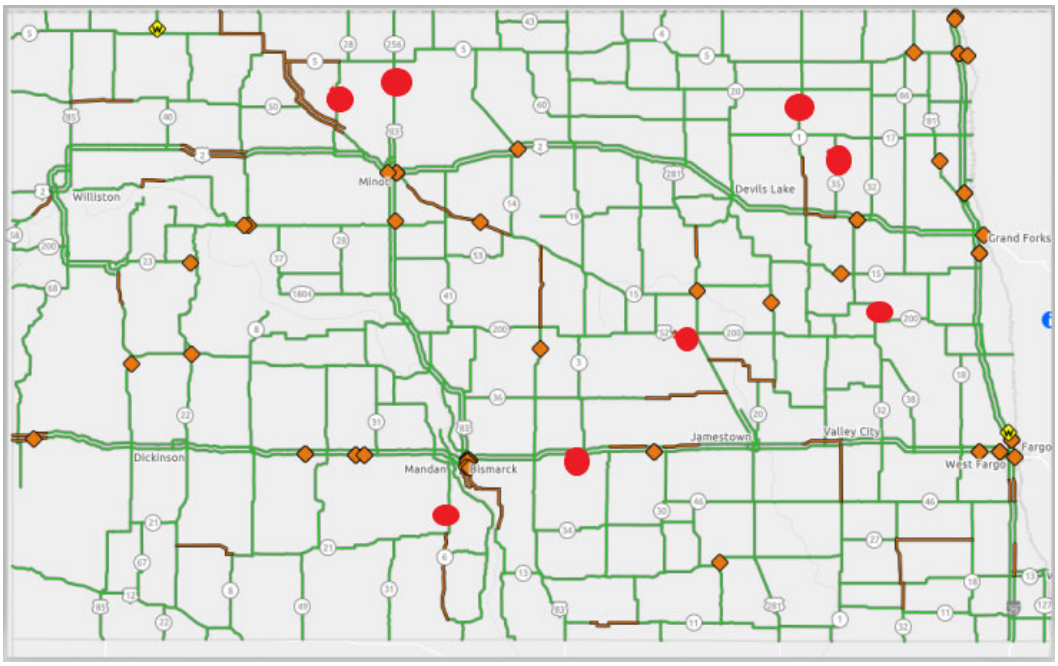

Figure 3.1: Project Locations Marked in Red.

The collected field mixes represent typical mixes used in North Dakota. Table 3.1 shows the job mix formula (JMF) details, including binder grade, volumetrics, gradation, and (reclaimed asphalt pavement) RAP content. The binders used in these projects were PG 58S-28 (2 projects), 58H-34 (4 projects), and PG58S-34 (4 projects). Binders used in the nine projects were collected for rheological characterization. The binder used in HWY 6 for the year 2022 paving season was unavailable. Table 3.3 shows that different binder grades were used in HWY 32, PG 58S-28, and PG58H-34, while the gradation and volumetrics remained the same. The HWY 32 project provided an opportunity to evaluate the performance of these two mixes based on laboratory

experiments. Figure 3.2 presents a summary of the gradation, where it can be observed that I-94 and HWY 83 had finer gradations among the ten mixes.

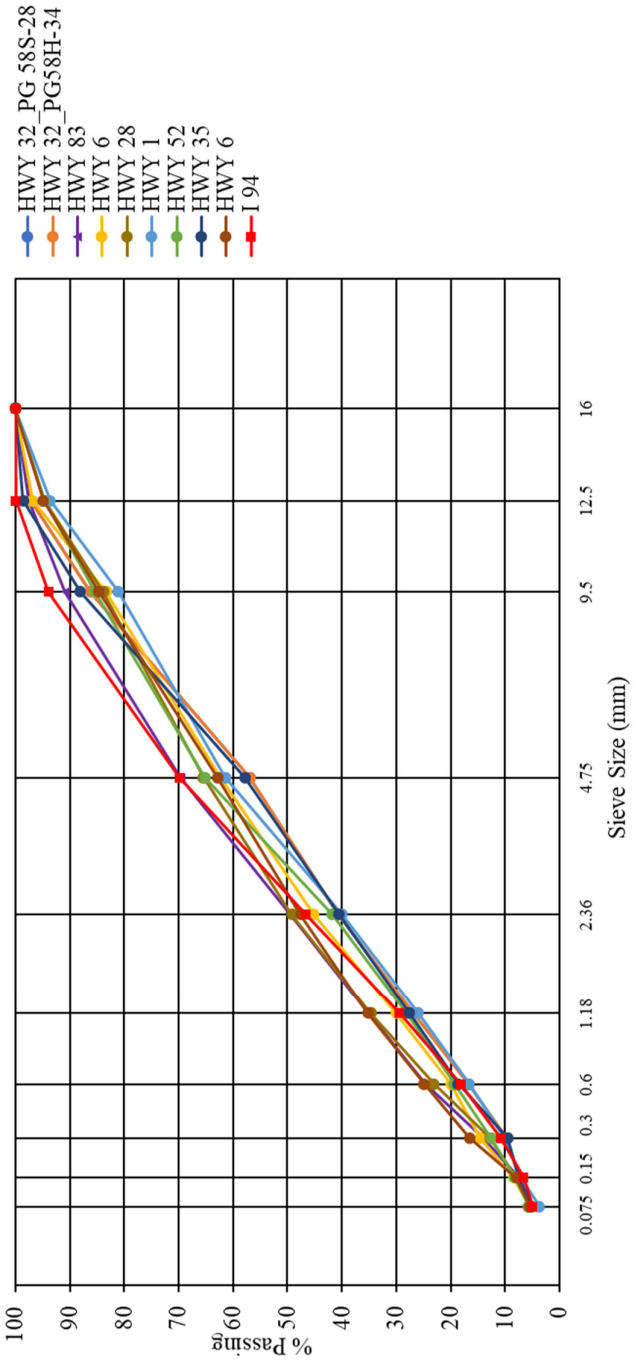

Figure 3.2: Gradation for the Mixtures under Investigation

Table 3.1: Summary of Mix Properties from JMFs

Year		2021					2022				
Highway Project		HWY 32	HWY 32	HWY 83	HWY 6	HWY 28	HWY 1	HWY 52	HWY 35	HWY 6	I 94
Project Location (District)		**Finley**	**Finley**	**Minot**	**Bismarck**	**Minot**	**Grand Forks**	**Devils Lake**	**Grand Forks**	**Bismarck**	**Bismarck**
NMAS		**12.5**	**12.5**	**12.5[a]**	**12.5**	**12.5**	**12.5**	**12.5**	**12.5**	**12.5**	**12.5[a]**
Gradation, % passing	Sieve size										
	5/8" (16mm)	100	100	100	100	100	100	100	100	100	100
	1/2" (12.5mm)	97.2	97.2	97.6	96.9	94.6	93.6	94.7	98.6	94.9	99.9
	3/8" (9.5mm)	86.2	86.2	90.9	83.3	83.9	81.1	85.4	88.1	84.7	93.9
	#4 (4.75mm)	56.9	56.9	69.7	62.4	65.5	61.4	65.2	57.8	62.9	69.9
	#8 (2.36mm)	40.7	40.7	49.4	45.2	49.2	40	41.8	40.5	47.6	46.6
	#16 (1.18mm)	26.9	26.9	35.1	30	34.7	26	28	27.6	35.2	29.4
	#30 (0.6mm)	16.7	16.7	24.7	20	23.1	16.6	19.3	18.6	24.9	18.2
	#50 (0.3mm)	9.7	9.7	14	14.6	12.8	10.1	12.6	9.5	16.5	10.8
	#100 (0.15mm)	7.5	7.5	7.5	8.5	8	7.1	8.2	7.5	7.9	6.6
	#200 (0.075mm)	5.2	5.2	5	5.5	5.7	3.7	5.6	5.3	5.4	5
Asphalt content, %		6	6	5	5.5	5.5	6.5	5.5	6.2	5.4	5.3
RAP, %		15%	15%	25%	25%	0%	15%	0%	20%	20%	20%
Design traffic level, MESAL		<3	<3	<3	<3	<3	<3	<3	<3	<3	<3
Binder grade		58S-28	58H-34	58H-34	58S-34	58S-28	58S-34	58H-34	58S-34	58S-34	58H-34
Coarse aggregate angularity, %		90.2	90.2	98.5	94	96.7	88.9	97	92.3	89.3	95.7
Fine aggregate angularity, %		44	44	45.4	42.5	45.6	43.5	47.1	43.8	42.5	45.8
Flat and elongated, %		0	0	0	0.3	4.3	2.2	0.9	0	0.2	0
Sand equivalent		46	46	81.4	43.4	65.3	68.6	74.4	48.8	54.7	65.9
Design gyration level		75	75	75	75	75	75	75	75	75	75
Design air voids, %		4	4	4	4	4	4	4	4	3.9	4
Design VMA, %		15.1	15.1	14.2	14.5	15.1	14.5	15	14.5	14.9	14
Design VFA, %		73.7	73.7	71.9	72.2	73.6	72.6	71	72.2	73.5	73.1
Filler to effective binder content ratio		1	1	1.1	1.2	1.2	0.8	1.2	1.1	1.1	1.2
a = HWY 83 and I 94 mixes are technically NMAS 9.5mm but meet NDDOT 12.5 mm mix specifications											
Note: MESAL = million equivalent single axle loads; VMA = voids in mineral aggregate; VFA = voids filled with asphalt											

3.2 Material Preparation and Testing

3.2.1 Binder Preparation

This study investigated binder properties in unaged, short-term aged, and long-term aged conditions. Steric hardening occurs to asphalt when stored at room temperature over time; therefore, the binders were heated at 290 ºF for 4 hours before testing the binder for unaged conditions.

Figures 3.3 and 3.4 show the equipment and process used in simulating short-term aging. The Rolling Thin Film Oven (RTFO) was used whereby 35±0.5 g of the binder was placed in the oven for 85 minutes at 163 ºC (325ºF) according to AASHTO T240 (AASHTO, 2021b).

Figure 3.3: Rolling Thin-Film Oven (RTFO)

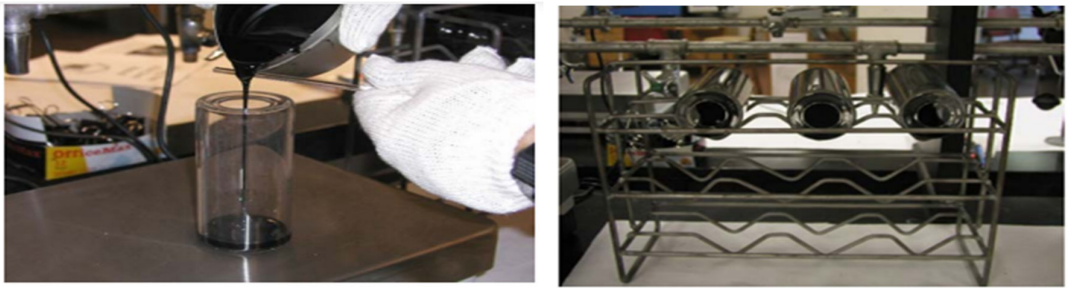

Figure 3.4: Pouring 35 ± 0.5g of Binder into each Container and Container Cooling on Sample Rack

Long-term aging is simulated in the laboratory by further aging of the short-term aged binder. A specimen weighing 50±0.5g is placed in the Pressure Aging Vessel (PAV) for 20h ± 10 minutes and subjected to a temperature of 100 ºC (212ºF) at an air pressure of 2.1 ± 0.1 MPa according to AASHTO R28 (AASHTO, 2021a). Figure 3.5 shows the PAV used in this study.

Figure 3.5: Pressurized Aging Vessel (PAV)

3.2.2 Binder Rheological Testing

I. Viscosity

Figure 3.6 shows the viscometer used to perform the viscosity tests. The viscosities of the unaged, short-term aged, and long-term aged binders were measured at 135 ºC in accordance with AASHTO T 316 (AASHTO, 2019).

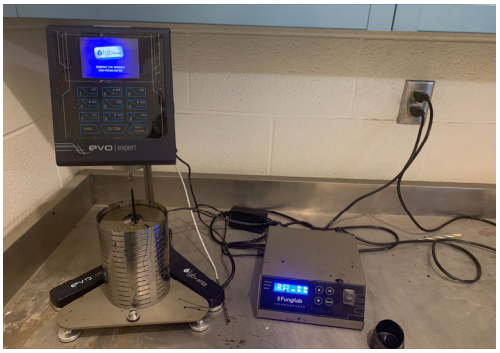

Figure 3.6: Viscometer

II. Complex Modulus |G| and Phase Angle (δ)*

Figure 3.7 shows the dynamic shear rheometer (DSR) used to measure |G*| and δ. The |G*| and δ values were measured at 10 rads/sec for the unaged, short-term, and long-term aged binders according to AASHTO T 315(AASHTO, 2020a).

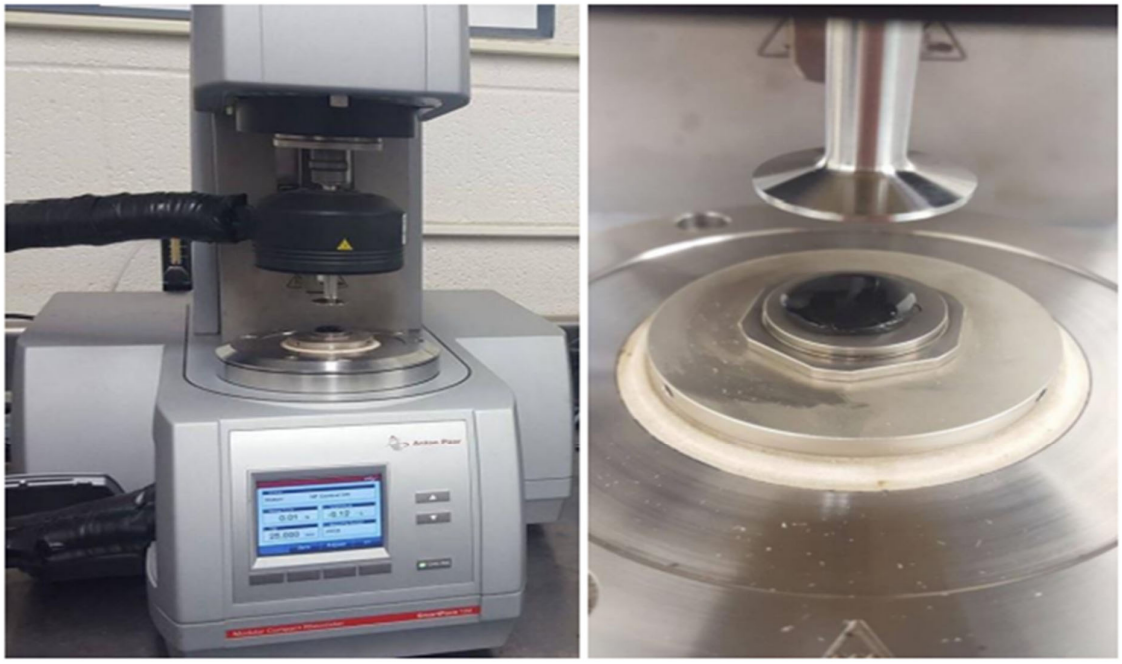

Figure 3.7: Dynamic Shear Rheometer (DSR)

3.2.3 Binder Prediction

The MEPDG requires measured values of |G*| and δ as level 1 and 2 inputs, while viscosity (μ) is required as a level 3 input. Pavement projects have varying reliability requirements and measuring the |G*| and (δ) of asphalt binders is costly and time-consuming. Predicting these parameters using existing models can provide a valuable tool for pavement engineers, especially for low-priority roads.

The binder |G*| and δ were predicted using models developed by Bari and Witczak (2007). These models employ the revised ASTM A_i-VTS viscosity models to calculate viscosity. Default A and VTS parameters based on the Superpave Performance Grade (PG) system, as shown in Table 3.2, were used to achieve this goal.

Table 3.2: Default Values of A and VTS Based on Asphalt PG (Kutay & Jamrah, 2013)

PG	A	VTS
58-28	11.01	-3.701
58-34	10.035	-3.35
64-34	9.461	-3.134

3.2.4 Multiple Stress Creep Recovery (MSCR)Test

The MSCR test was conducted on RTFO-aged binders at a specified temperature to characterize the rutting response in asphalt binders. A DSR with a 25-mm parallel plate and a 1-mm gap was used. The test was conducted at 58 ºC for the seven binders. The asphalt binder was tested in creep at a percent of the recovery, followed by nonrecoverable creep compliance. The two stress levels used were 0.1 KPa and 3.2 KPa; 20 cycles ran at the 0.1 KPa stress level, followed by 10 cycles at the 3.2 KPa stress level for a total of 30 cycles. The creep portion of this test lasts for 1s, followed by 9s of the recovery period as per AASHTO TP 70 (AASHTO, 2014a). The nonrecoverable creep compliance (J_{nr}) was subsequently obtained.

3.2.5 Linear Amplitude Sweep (LAS) Test

LAS test was conducted according to AASHTO TP 101 (AASHTO, 2014b), which is based on the simplified viscoelastic continuum damage (S-VECD) analysis method and performed using the DSR. This test was performed on PAV-aged asphalt binder residue. A DSR 8mm parallel plate geometry was used with a 2 mm gap at a temperature of 19 ºC.

The LAS test consists of a frequency sweep for estimating undamaged asphalt binder properties and an amplitude sweep. The first test applied oscillatory shear loadings at twelve various frequencies to measure |G*| and δ. The second test determined the asphalt binder's damage characteristics.

3.3 |E*| Testing

The ten HMA mixes collected in the field were prepared into test specimens, and their |E*| and δ measured over a range of temperatures and loading frequencies. The results were later used to develop a |E*| database for typical HMAs in North Dakota and to evaluate the practicality of using existing models for local applications.

3.3.1 Specimen Fabrication

This project required the |E*| testing to be conducted on 100 mm diameter by 150 mm tall specimens with a standard air void content of 7±1%. The procedure for estimating the mass required to produce test specimens at the target air void is laid out in AASHTO R 83 (AASHTO, 2017a). Once the required mass was determined, the mixes were heated to 1350C, and a Superpave gyratory compactor (SGC) was used to compact the loose mixes to achieve 100mm diameter by 180mm tall gyratory specimens, as shown in Figure 3.8.

The gyratory specimens were later cored and cut using the equipment shown in Figure 3.9 to achieve test specimens with evenly distributed air voids. Figure 3.10 shows the final test specimen.

Figure 3.8: SGC with Compacted Gyratory Specimen.

Figure 3.9: Cutting and Coring machines.

Table 3.3 presents the mass of loose mix compacted for each project and the percentage of air voids achieved; all test species were within the target air void of 7±1%. Three test specimens were prepared for each asphalt mix.

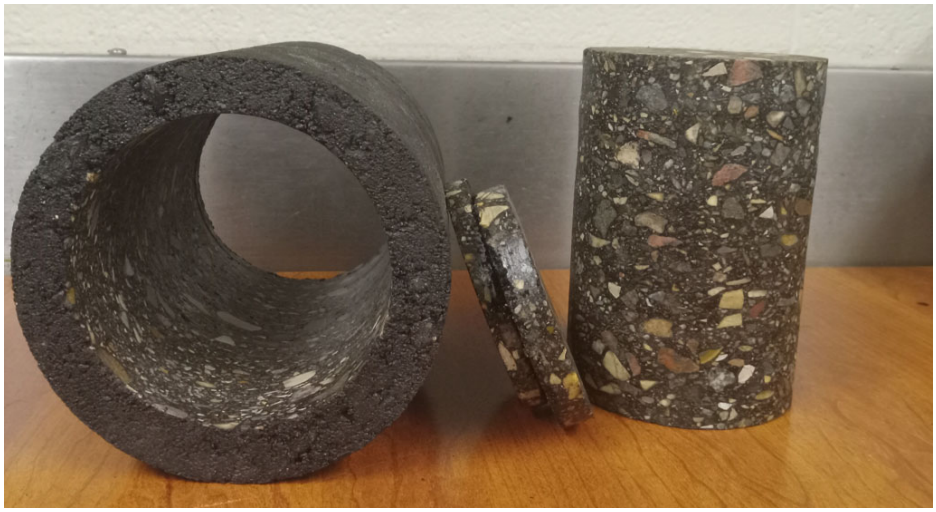

Figure 3.10: Test Specimen after Cutting and Coring.

Table 3.3: Summary of the Air Voids Achieved for the 10 Mixes.

Project	Specimen Name	Mass Compacted[a] (g)	Air Void[b] (%)
HWY 35_PG58S-34_20%RAP	35-1	7026	7.1
	35-2		6.9
	35-3		7.3
HWY 32_PG58S-28_15%RAP	32S-1	6954	6.7
	32S-2		7.0
	32S-3		6.8
HWY 32_PG58H-34_15%RAP	32H-1	6953	6.8
	32H-2		6.6
	32H-3		6.6
HWY 83_PG58H-34_10%RAP	83-1	7209	7.2
	83-2		7.3
	83-3		7.0
HWY 28_PG58S-28_0%RAP	28-1	7203	6.8
	28-2		7.0
	28-3		7.0
HWY 1_PG58S-34_15%RAP	1-1	7064	7.2
	1-2		7.4
	1-3		7.7
HWY 6_PG58S-34_25%RAP	6-1	7021	6.6
	6-2	6990	7.1
	6-3		7.0
HWY 52_PG52H-34_25%RAP	52-1	7170	6.6
	52-2		7.1
	52-3		6.9
I-94_PG58H-34_20%RAP	94-1	7089	7.1
	94-2		7.4
	94-3		7.1
HWY 6_PG58S-34_20%RAP	6-1	7057	6.9
	6-2		7.1
	6-3		7.1
a = Mass of gyratory specimen, b = Air void of test specimen			

3.3.2 Testing Apparatus

Figure 3.11 shows the AMPT used in this project to conduct the |E*| testing; it is a computer-controlled electro-mechanical servo-actuated system capable of applying static and dynamic loads over a range of temperatures and frequencies. The AMPT is equipped with a

confining chamber, a temperature-control unit, and a data-collection unit. Once the test is completed, the data collection and analysis are automatically processed, and |E*| and δ values are generated.

Figure 3.11: AMPT Set-up

3.3.3 |E*| Testing Procedure

Table 3.2 shows the |E*| testing temperatures and loading frequencies. These testing regimens were selected according to AASHTO R 84 (AASHTO, 2017b). Before testing, the specimens were placed in a temperature-conditioning chamber. A dummy specimen with a thermocouple inserted at its center was used to monitor the conditioning process. Figure 3.12 shows the temperature-conditioning set-up.

Figure 3.12: Test Specimens with Dummy Specimen Before Temperature Conditioning.

|E*| testing was conducted in descending order, beginning with the lowest temperature and highest frequency, as shown in Table 3.4. According to AASHTO T 378, all frequencies were tested in descending order before proceeding to the higher test temperature (AASHTO, 2017c).

Table 3.4: Testing Temperature and Loading Frequencies.

Temperature (^{0}C)	Frequency (Hz)
4	10, 1, 0.1
20	10, 1, 0.1
35	10, 1, 0.1. 0.01

The strains occurring at each testing temperature and loading condition were measured through LVDTs attached to holding brackets, which are mounted on studs. Figure 3.13 shows the mounting studs fixing jig, and an LVDT attached to the holding bracket. The data-acquisition system collected the measurements and determined the |E*| and δ.

Figure 3.13: Mounting Studs on Test specimen and LVDT Attached to Holding Brackets

3.4 Verification of |E*| Predictive Models

Three models, the original Witczak (Eq. 2-19), the modified Witczak (Eq. 2-20), and the Hirsch (Eq. 2-22) models, were used to predict |E*| values in an attempt to evaluate their

applicability for local applications. For level 3, default binder properties and mix volumetrics were used as inputs.

3.4.1 Model Verification for Level 2

In level 2 of the Pavement ME, measured short-term (RTFO) aged binder rheological properties combined with mix volumetrics obtained from the JMF were used as inputs into these models. Table 3.5 presents the model inputs for level 2 prediction. |G*| and δ values obtained from earlier binder testing were converted into viscosity (η) using Eq. 3-1, which is a required input in the original Witczak model (ARA, 2004).

$$\eta = \frac{G^*}{10}\left(\frac{1}{sin}\right)^{4.8628} \quad (3\text{-}1)$$

Table 3.5: Model Inputs for Level 2 Verification

			Required Inputs		
Model	Description	Units	Original Witczak	Modified Witczak	Hirsch
Binder Properties	η	10^6 Poise	√		
	f	Hz	√		
	|G*|	psi		√	√
	δ	degrees		√	
Mix Volumetric Properties	Vbeff	%	√	√	
	Va	%	√	√	
	VMA	%			√
	VFA	%			√
	ρ¾	%	√	√	
	ρ⅜	%	√	√	
	ρ4	%	√	√	
	ρ200	%	√	√	

3.4.2 Model Verification for Level 3

For level 3, default binder properties and mix volumetrics from the JMF were used as inputs, as shown in Table 3.6. The binder grade was used to select default A and VTS values based on Table 3.2. These default parameters were then used to generate viscosity (η) (Eq. 2-4), |G*| (Eq. 2-5), and δ (Eq. 2-6) values.

Table 3.6: Model Inputs for Level 3 Verification

			Required Inputs		
Model	Description	Units	Original Witczak	Modified Witczak	Hirsch
Binder Properties	PG		√	√	√[a]
Mix Volumetric Properties	Vbeff	%	√	√	
	Va	%	√	√	
	VMA	%			√
	VFA	%			√
	ρ¾	%	√	√	
	ρ⅜	%	√	√	
	ρ4	%	√	√	
	ρ200	%	√	√	

a =|G*| used in the Hisch model was obtained from the Modified Witczak |G*| predictive model

3.5 Flow Number (F_N) Tests

F_N tests were conducted to measure the rutting resistance of the 10 HMA mixes. The values obtained were compared to |E*| and iRLPD test results.

3.5.1 Specimen Fabrication

The same test specimens were used for the |E*| testing and the FN tests. Once the last |E*| loading sequence was completed at 35°C, the same test specimens were temperature-conditioned at 54°C and used for the FN test. |E*| testing is considered a non-destructive test, justifying the re-use of the test specimens for the FN test.

3.5.2 Testing Apparatus

The AMPT was used to measure F_N, and the test was conducted without the attached LVDTS, as shown in Figure 3.14.

Figure 3.14: Specimen before and after F_N Test

3.5.3 F_N Test Procedure

The F_N tests were carried out by applying a uniaxial compressive load to test specimens 100 mm (4 in.) in diameter and 150 mm (6 in.) in height at a temperature of 54°C. The compressive load is a repeated haversine loading (1 cycle with 0.1 s loading time and 0.9 s resting time) applied to the specimen, and the cumulative deformation as a function of the number of load cycles was recorded using the data-acquisition software.

3.6 Incremental Repeated Load Deformation (iRLPD) Test

Incremental repeated load permanent deformation (iRLPD) tests were conducted to measure the rutting resistance of the 10 sampled HMA mixes. The iRLPD test results were also compared to |E*| and F_N test results.

3.6.1 Specimen Fabrication

The iRLPD test specimens measured 100 mm in diameter by 150 mm in diameter with air void content of 7±1% fabricated according to AASHTO 83. Two replicates were prepared for each project, and the target air void content was within the range as illustrated in Table 3.7.

Table 3.7: Summary of the Air Voids Achieved for the 10 Mixes.

Project	Specimen Name	Mass Compacted[a] (g)	Air Void[b] (%)
HWY 35_PG58S-34_20%RAP	35-1	7026	7.1
	35-2		7.0
HWY 32_PG58S-28_15%RAP	32S-1	6954	7.8
	32S-2		7.4
HWY 32_PG58H-34_15%RAP	32H-1	6953	7.4
	32H-2		7.3
HWY 83_PG58H-34_10%RAP	83-1	7209	7.1
	83-2		7.1
HWY 28_PG58S-28_0%RAP	28-1	7203	7.1
	28-2		7.2
HWY 1_PG58S-34_15%RAP	1-1	7064	7.2
	1-2		7.1
HWY 6_PG58S-34_25%RAP	6-1	6990	7.4
	6-2		7.4
HWY 52_PG52H-34_25%RAP	52-1	7170	7
	52-2		7.1
I-94_PG58H-34_20%RAP	94-1	7089	6.9
	94-2		7
HWY 6_PG58S-34_20%RAP	6-1	7057	6.6
	6-2		7.1
a = Mass of gyratory specimen same as for |E*|fabrication, b = Air void of test specimen			

3.6.2 Testing Apparatus and Procedure

Figure 3.15 illustrates how the test specimens were wrapped in a rubber membrane to simulate field lateral support within pavement layers. The test specimens were then temperature-conditioned at 54^0C and monitored using a dummy specimen. Once ready, testing involved applying a load pulse that lasted 0.1s every 0.9s with 69kPa confining pressure in the AMPT. The iRLPD testing followed the rutting method B in AASHTO TP 116, where four stress levels were applied, 200 kPa (conditioning), 400 kPa, 600 kPa, and 800 kPa, each lasting 500 cycles (AASHTO, 2020b). The data-acquisition software automatically collected the readings to calculate the minimum strain rate (m*).

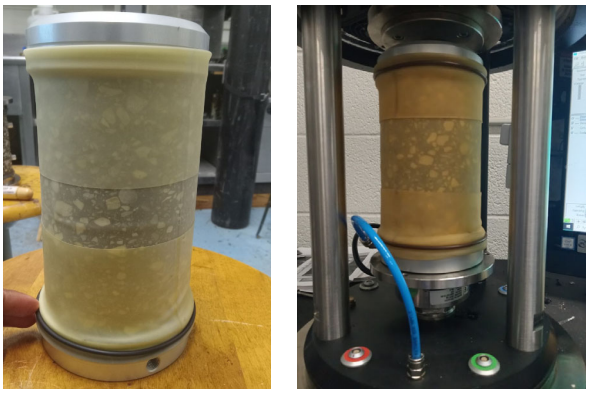

Figure 3.15: iRLPD Test Specimen Before Testing

3.7 Fatigue (S-VECD) Test

S-VECD tests were conducted to determine the damage characteristic curves of HMA mixes typically used in North Dakota. Due to insufficient material mixes, I-94_PG58H-34_20%RAP and HWY 6_PG58S-34_20%RAP were not included in the S-VECD testing. Therefore, test specimens were prepared for the remaining 8 projects.

3.7.1 Testing Apparatus

The AMPT was used to conduct the S-VECD tests. The test specimens needed to be secured, as shown in Figure 3.16, before being subjected to cyclic loading until failure.

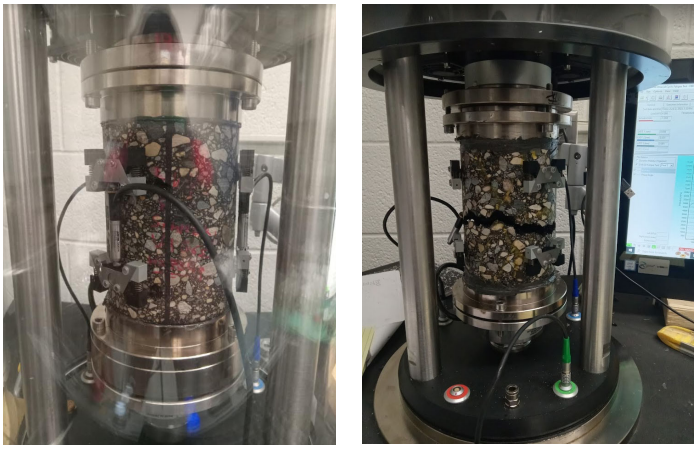

Figure 3.16: S-VECD Test Specimen Before and After Testing

3.7.2 Specimen Fabrication

The S-VECD test specimens were 100 mm in diameter by 130 mm tall and fabricated according to AASHTO 83, with an air void content of 7±1%. Three replicates were prepared for each project, and the air void content achieved for every specimen was within the target range, as shown in Table 3.8.

Figure 3.17 illustrates the next steps once the test specimens were found to be within the target air void content. First, mounting studs were fixed to facilitate strain measurement through LVDTs, as shown in Figure 3.6. Second, loading platens were attached to the test specimens using steel putty and a fixing jig. Finally, the test specimens were temperature-conditioned at 12^{o}C once the putty had fully cured. A dummy specimen was used to monitor the temperature conditioning process before transferring the test specimen to the AMPT for testing.

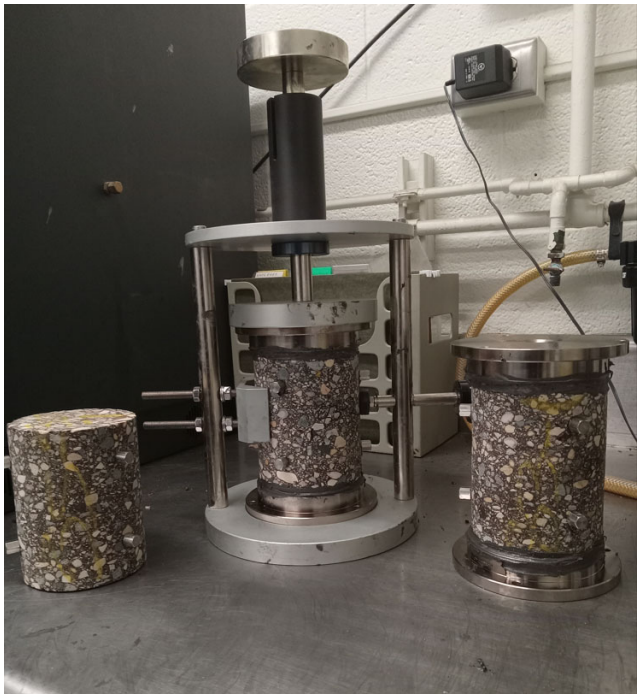

Figure 3.17: S-VECD Test Specimen Preparation

Table 3.8: Summary of the Air Voids Achieved for the 8 Mixes.

Project	Specimen Name	Mass Compacted[a] (g)	Air Void[b] (%)
HWY 35_PG58S-34_20%RAP	35-1	7026	7.0
	35-2		6.7
	35-3		6.7
HWY 32_PG58S-28_15%RAP	32S-1	6954	7.9
	32S-2		7.8
	32S-3		7.2
HWY 32_PG58H-34_15%RAP	32H-1	6953	7.1
	32H-2		7.3
	32H-3		6.8
HWY 83_PG58H-34_10%RAP	83-1	7209	7.3
	83-2		7.1
	83-3		7.0
HWY 28_PG58S-28_0%RAP	28-1	7203	6.9
	28-2		7.1
	28-3		6.6
HWY 1_PG58S-34_15%RAP	1-1	7064	7.0
	1-2		7.1
	1-3		7.1
HWY 6_PG58S-34_25%RAP	6-1	6990	6.9
	6-2		7.7
	6-3		7.7
HWY 52_PG58H-34_0% RAP	52-1	7170	6.8
	52-2		6.5
	52-3		6.5

a = Mass of gyratory specimen same as for |E*|fabrication, b = Air void of test specimen

3.7.3 S-VECD Test Procedure

Once secured to the AMPT, the test specimens were allowed to equilibrate to the testing temperature of 12^0C. The tests were conducted according to AASHTO TP-107-18 (AASHTO, 2020c). Once the specimen failed, the test was stopped automatically, and the parameters necessary for calculating the damage characteristic curve were obtained.

3.8 Creep Compliance Prediction

The creep compliance was estimated by converting the dynamic modulus, |E*|, to relaxation modulus, E(t), and finally to D(t). The three steps listed below were repeated for all the ten projects:

I. Eq. 2-15 was used to obtain the storage modulus E' from |E*| data, which was then plotted on a logarithmic scale, as shown in Figure 3.18. A sigmoidal function was used to fit the storage modulus data.

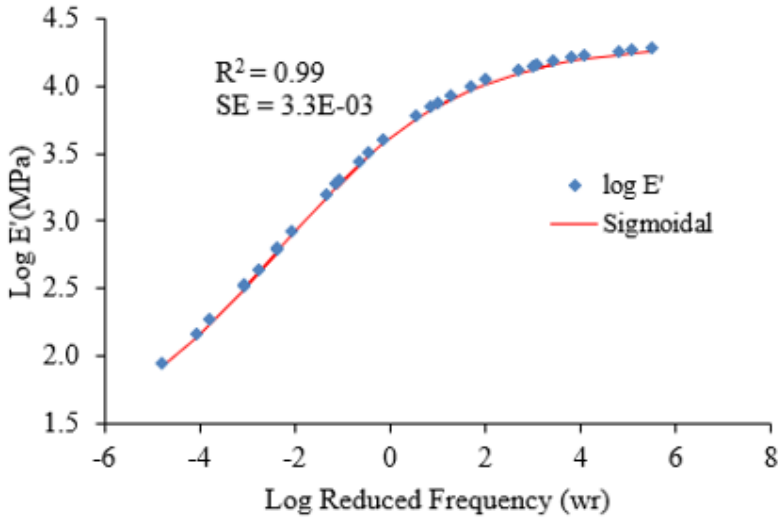

$$logE'(wr) = 4.30 - \frac{3.047}{(1 + \exp(1.226 + 0.522 logwr)}$$

Figure 3.18: Storage Modulus and Sigmoidal Fitting Curve (HWY32_PG58S-28_15%RAP)

II. The local logarithmic slope of the storage modulus (n) was then calculated over the specified frequency range. Eq. 2-25 was then used to compute the relaxation moduli, E(t) data, and plotted as shown in Figure 3.19. A sigmoidal function was used to fit the E(t) data.

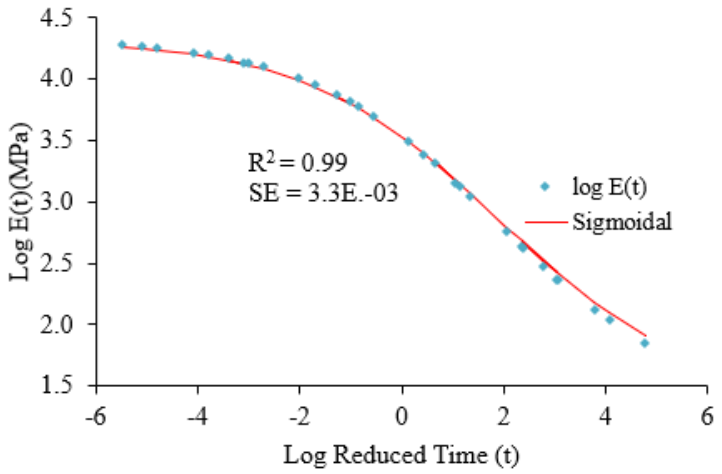

$$logE(t) = 1.371 + \frac{2.95}{(1 + \exp(-1.011 + 0.524logt)}$$

Figure 3.19: Predicted E (t)and Sigmoidal Fitting Curve (HWY32_PG58S-28_15%RAP)

III. The local derivative of the E(t) sigmoidal function was then used in Eq. 2-26 to calculate the creep compliance D(t). A sigmoidal function was then fitted to the D(t) data as shown in Figure 3.20.

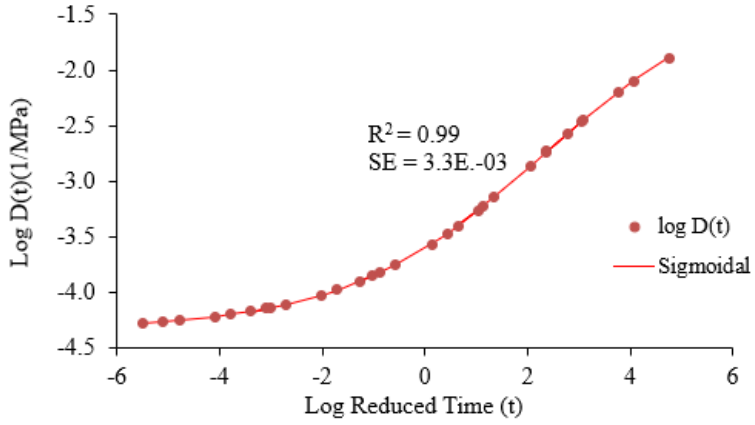

$$logD(t) = -4.321 - \frac{3.09}{(1 + \exp(1.193 - 0.525logt)}$$

Figure 3.20: Predicted D (t) and Sigmoidal Fitting Curve (HWY32_PG58S-28_15%RAP)

3.9 Summary of Tests Conducted

Tables 3.9 and 3.10 show the laboratory tests conducted on the binders and asphalt

mixes, including the number of samples prepared and the test standards used.

Table 3.9: Summary of Binder Tests

No.	Binder Test	Binder type	Sample preparation	Replicates	Test Standard
1.	Complex Shear Modulus and Phase angle	Unaged	-	18	AASHTO T315
		Short-term aged	RTFO	18	AASHTO T315, R28
		Long-term aged	PAV	18	AASHTO T315, T240
2.	Viscosity	Unaged	-	18	AASHTO T316
		Short-term aged	RTFO	18	
		Long-term aged	PAV	18	

Table 3.10: Summary of Mix Tests

No.	Mix Test	Specimen	The standard for sample preparation	Number of specimens	Test Standard
1.	Dynamic modulus	100 mm dia. x 150 mm tall	AASHTO R 83	30	AASHTO TP 378
2.	Flow number	100 mm dia. x 150 mm tall			AASHTO TP 378
3.	iRLPD	100 mm dia. x 150 mm tall	AASHTO R 83	20	AASHTO TP 116
4.	Number of cycles until fatigue failure	100 mm dia. x 130 mm tall	AASHTO R 83	24	AASHTO TP 107

Chapter Four- Results and Discussions

4.1 Binder Viscosity

Binder viscosity plays a fundamental role in all three levels of the MEPDG. In addition, the evaluation of a binder's viscosity as it ages indicates a pavement's performance throughout its design life. Table 4.1 illustrates that the viscosity of the eight binders increases with aging. Figure 4.1 presents the same data, which displays a similar trend. The viscosity of the binders was between the ranges of 0.170 ± 0.02 and 0.280 ± 0.03 Pa·s in all projects, indicating that the sampled binders will maintain their viscoelasticity even after undergoing long-term aging (ASTM, 2015). However, it was observed that binders with performance grade 58H-34 had higher viscosity values, especially after aging. The binders with PG grade 58H-34 are best suited to resist rutting because of their higher stiffness throughout the aging process.

Table 4.1: Binder Viscosities

Project Name	Location	Grading	Viscosity at 135°C (mPa.s)		
			Unaged	Short-term aged	Long-term aged
HWY 32	Finley	PG 58S-28	454	841	869
HWY 32	Finley	PG 58H-34	840	1601	2193
HWY 83	Minot	PG 58H-34	1602	2215	2379
HWY 6	Bismarck	PG 58S-34	785	1661	2217
HWY 28	Minot	PG 58S-28	464	837	1080
I 94	Bismarck	PG 58H-34	1507	1801	2976
HWY 52	Devil's Lake	PG 58H-34	1864	2305	3177
HWY 1	Grand Forks	PG 58H-34	624	892	1280
HWY 35	Grand Forks	PG 58S-34	1414	1576	2033

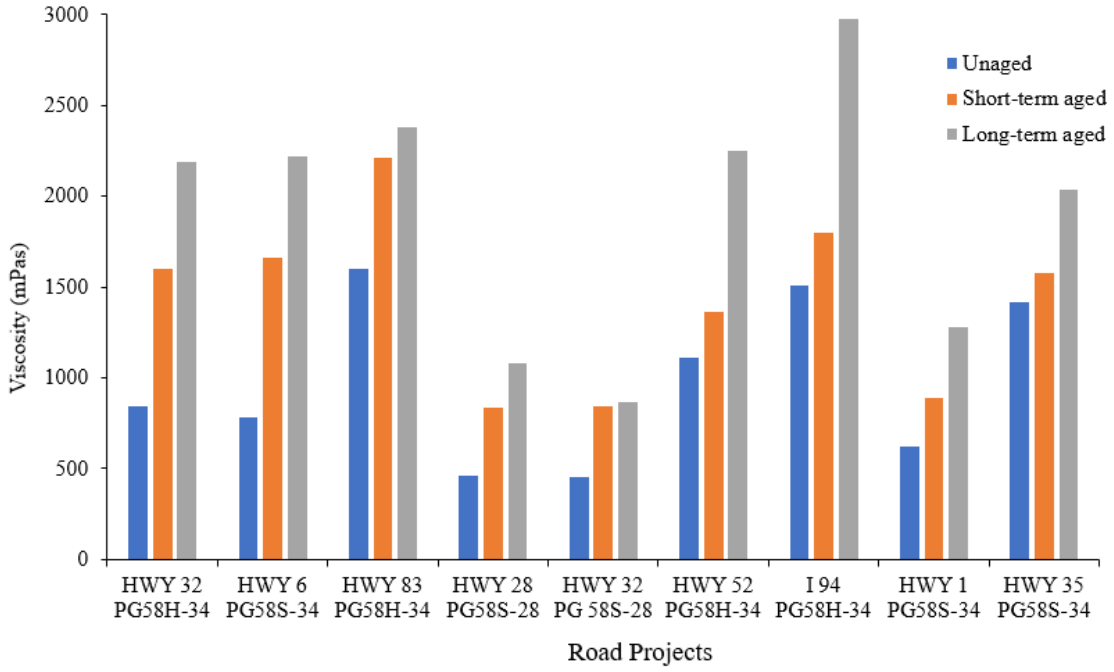

Figure 4.1: Binder Viscosity for the Nine Projects

4.2 Complex Shear Modulus |G*| and Phase Angle (δ)

The |G*| and associated δ of the eight binders in their original or unaged conditions were measured. DSR was used at a 10 rad/sec frequency according to AASHTO T315 specifications. Figure 4.2 illustrates that generally, |G*| decreases with an increase in temperature, which means that binders are stiffer at lower temperatures and begin to soften once the temperature increases. An asphalt binder should be stiff and elastic to resist rutting; the parameter G*/sinδ is used to indicate the rutting susceptibility of binders. The fatigue resistance of in-depth r is illustrated using the G*.sinδ parameter from DSR.

4.2.1 Original Binder

Figures 4.2 and 4.3 present the original binder DSR test results. For unaged binders, the |G*|/sin(δ) value should be higher than or equal to 1.0 kPa; otherwise, the binder is deemed to have failed at that temperature. Figure 4.4 shows that the unaged binders were above the threshold at 58ºC and below as expected. The asphalt binder used in HWY 83 PG58H-34 had

the highest |G*| values, indicating that it could resist rutting up to a temperature of 64ºC. A significant difference was observed with the other binder with the same performance grade of PG58H-34 from HWY 32; it had the lowest |G*| values out of all the binders. The results indicated that the PG58H-34-HWY 32 binder could resist rutting up to 58ºC. This discrepancy illustrates the importance of undertaking local binder characterization to ascertain their performance. It is important to note that all the binders performed satisfactorily at high temperatures according to their performance grade.

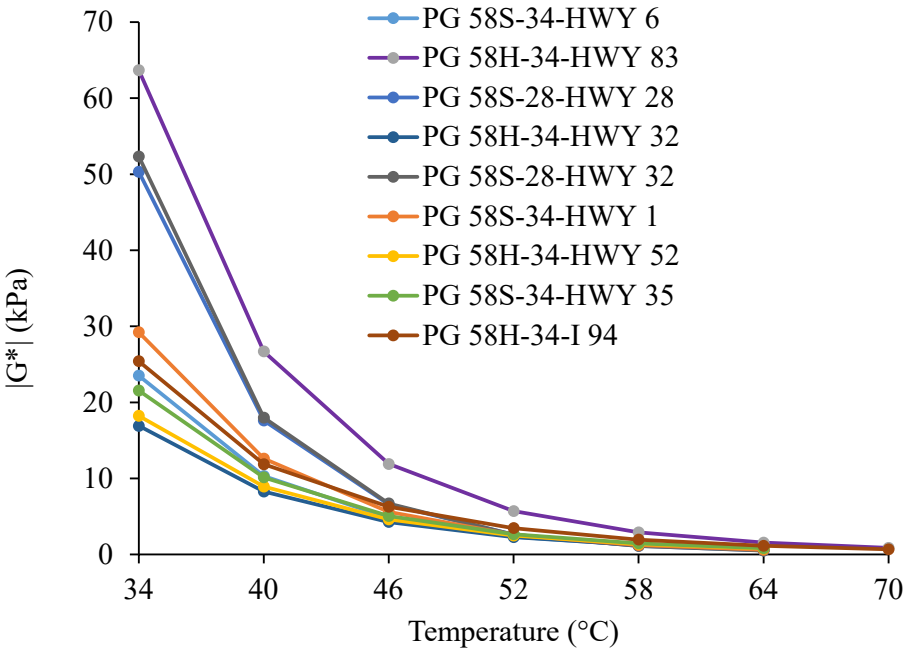

Figure 4.2: |G*| of the Unaged Binders

The phase angle (δ) is a parameter that measures a binder's elasticity. Figure 4.3 illustrates that binders designated as PG 58S-28 had higher δ values and were, therefore, less elastic than those designated as PG 58H-34.

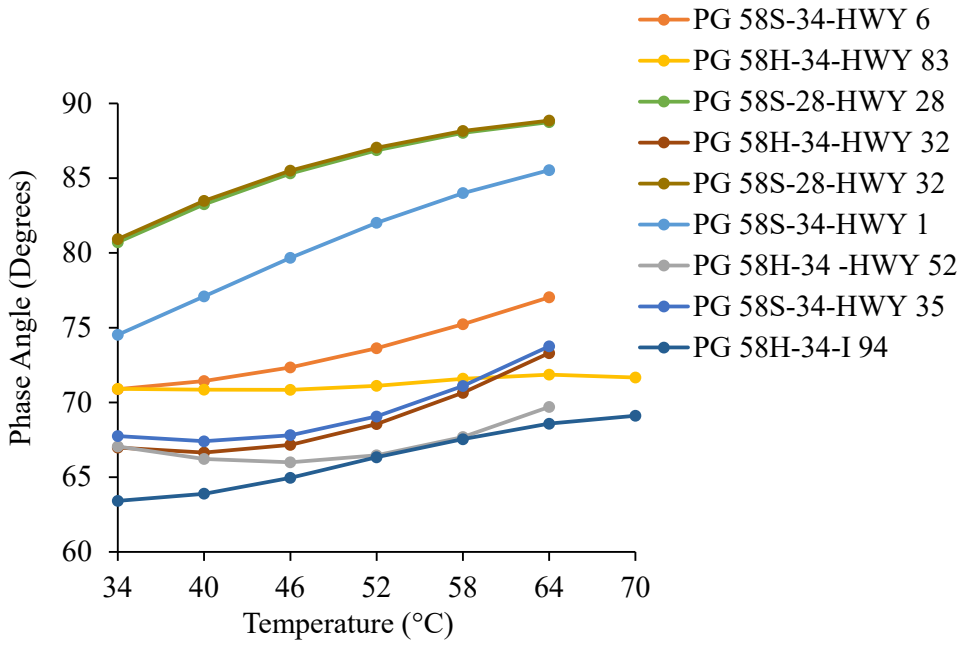

Figure 4.3: Phase Angles of the Unaged Binders

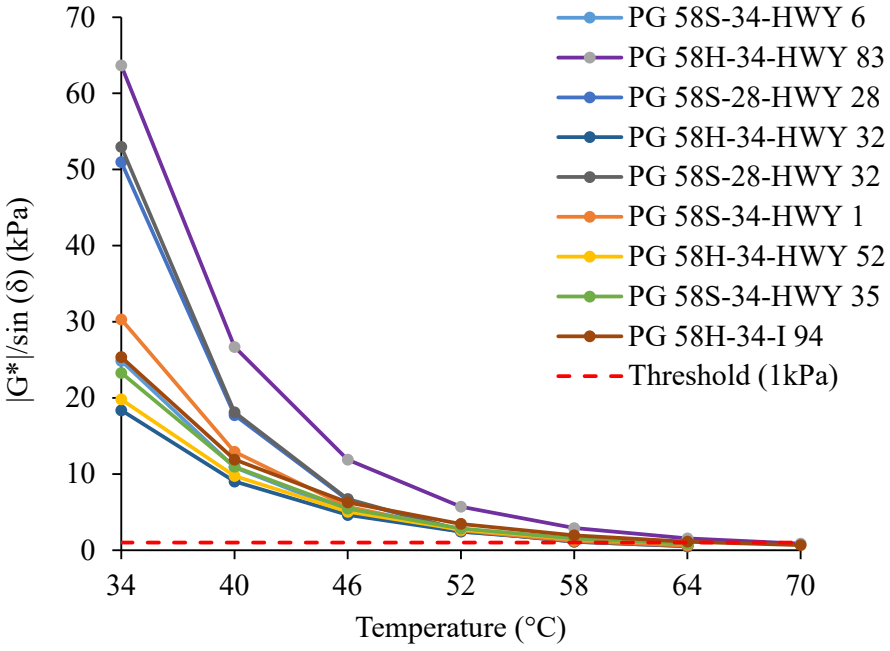

Figure 4.4: |G*|/sin(δ) values of the Unaged Binders

4.2.2 RTFO-Aged Binder

The RTFO, according to AASHTO T240, was used in the laboratory to simulate the binder's short-term aging. The RTFO simulates the aging that occurs on the binder during batching, mixing, transportation, and construction of the flexible pavement. The |G*| and δ of the RTFO-aged binders were determined as these are required design inputs in the MEPDG. Figure 4.4 presents the |G*| values of the RTFO-aged binder.

Figures 4.5 and 4.6 present the RTFO aged binder test results. The |G*|/sin(δ) value should be higher than or equal to 2.20 kPa for RTFO-aged binders; the threshold is highlighted in Figure 4.7. The results displayed a similar trend to those of the unaged binder. PG 58S-28-HWY 32, PG 58S-28-HWY 28, and PG 58H-34-HWY 83 displayed the highest |G*| values. PG58H-34-HWY 52 had the lowest |G*|. All the binders failed at the same temperatures as the unaged binder |G*| testing. This indicates that although short-term aging has a stiffening effect, the binders' rutting resistance properties remained consistent.

Figure 4.5 illustrates the δ of the RTFO-aged binders. The binders with higher δ values are generally less elastic, and it is apparent that these binders are the ones that displayed higher stiffness in Figure 4.5. For binders to resist rutting, they must have higher |G*| to indicate high stiffness and correspondingly lower δ as an indication of the ability to recover after deformation. These characteristics are especially important during an asphalt pavement's early life. PG 58H-34-HWY 83 displayed these characteristics and should be recommended for use in highways anticipating high traffic loads.

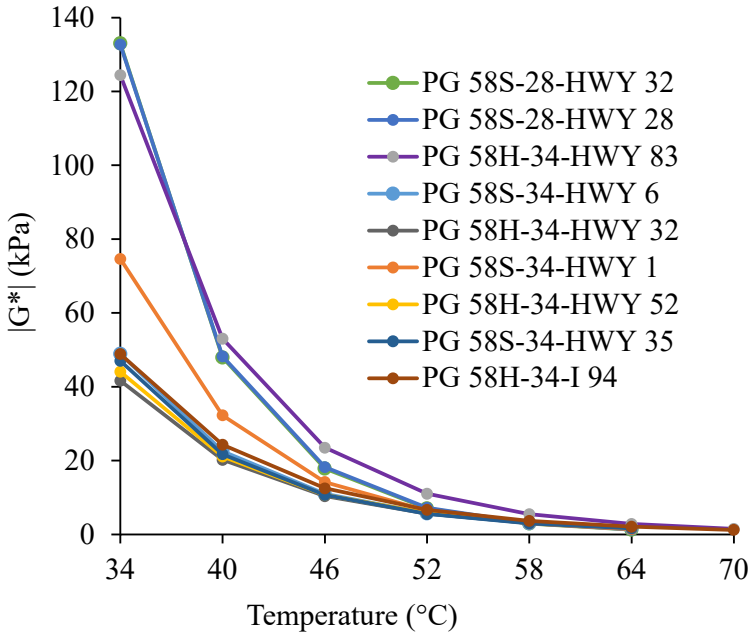

Figure 4.5: Complex Shear Modulus (|G*|) of the RTFO-Aged Binder

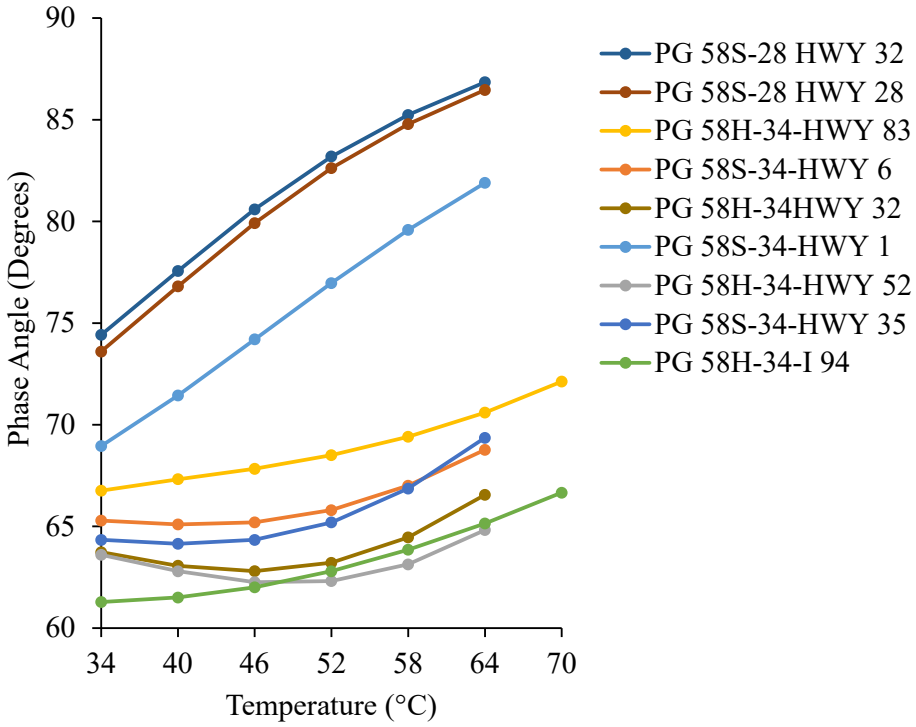

Figure 4.6: Phase Angles of the RTFO-Aged Binders

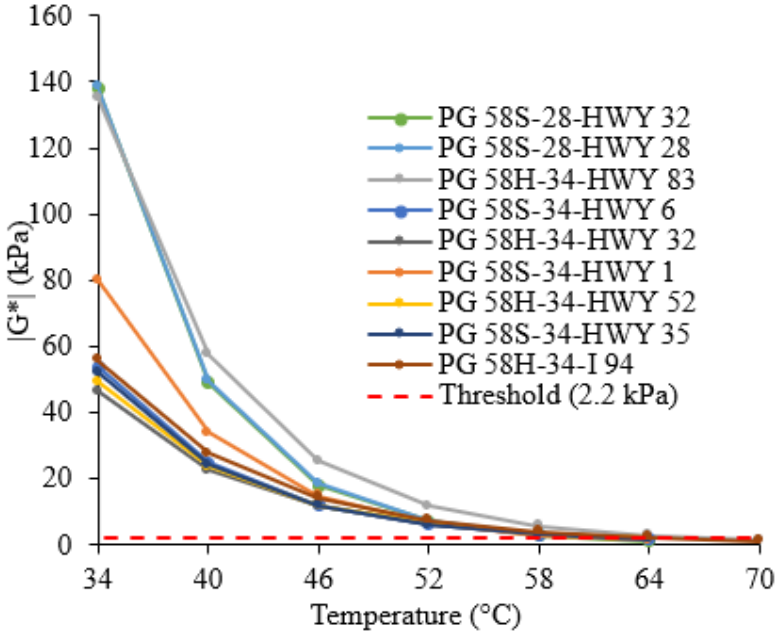

Figure 4.7: |G*|/sin(δ) values of the RTFO-Aged Binders

4.2.3 PAV-Aged Binder

Asphalt pavements begin to experience fatigue cracking at the later stages of their design life; therefore, it is important to determine and evaluate binder properties after undergoing long-term aging. The PAV is intended to simulate the long-term aging of the binder by exposing the binder to an elevated temperature in a pressurized chamber. The eight asphalt binders were first conditioned in the RTFO before the residues were conditioned further in the PAV. This long-term oxidative aging occurs in asphalt binders during pavement service. The PAV simulates 5 to 10 years of in-service aging of the asphalt binder (AASHTO, 2021a). The |G*| and δ of the PAV-aged binders are illustrated in Figures 4.8 to 4.9. The binder should be elastic and less stiff for PAV-aged binders to avoid cracking.

Figures 4.8 and 4.9 present the PAV-aged binder test results. The parameter used as a threshold value is the |G*|. sin(δ), which should be less than 5000 kPa, as highlighted in Figure 4.10.

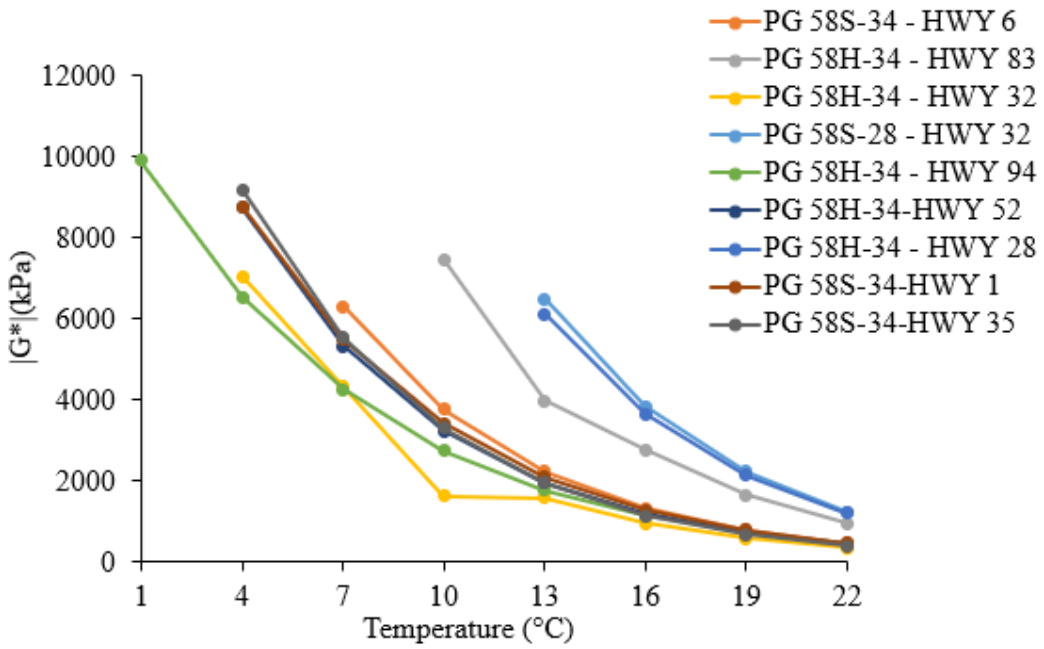

Figure 4.8: Complex Shear Modulus (|G*|) of the PAV-Aged Binder

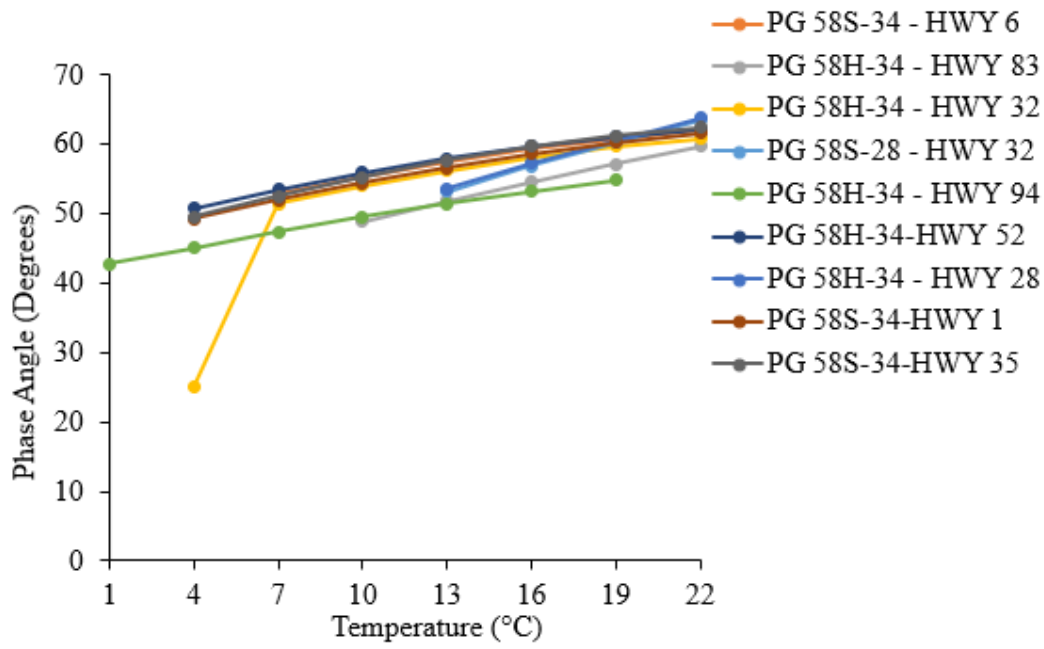

Figure 4.9: Phase Angle (δ) of the PAV-Aged Binder

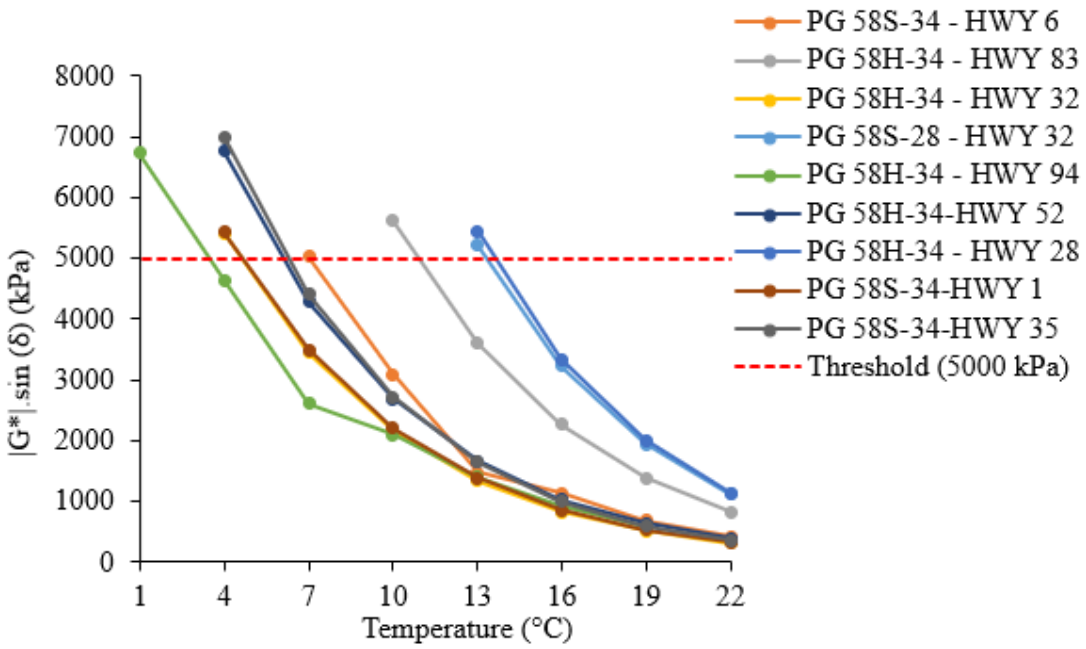

Figure 4.10: |G*|. sin(δ) values of the PAV-Aged Binder

PG 58H-34-HWY 52 had a |G*|. sin(δ) value that was less than 5000 kPa at -2ºC, PG 58H-34-HWY 94 at 1ºC and PG 58H-34-HWY 32 at 7ºC. The rest of the binders were above the threshold value at this temperature, indicating that PG 58H-34-HWY 52, PG 58H-34-HWY 94, PG 58S-34-HWY 1 and PG 58H-34-HWY 32 binders are the least susceptible to fatigue ranking. PG 58H-34 - HWY 28 and PG 58S-28 - HWY 32 failed to meet the threshold at 16ºC, indicating they are more susceptible to fatigue cracking.

4.3 Comparison of Measured and Predicted Binder Properties

|G*| and δ were predicted using predictive by inputting the default A and VTS values given in Table 2.1 into Eqs. 2-4, 2-5, and 2-6 to generate viscosity, |G*|, and δ. Then, the predicted results were compared with laboratory-measured |G*| and δ for the short-term aged binder.

Figure 4.11 compares the predicted |G*| with the RTFO-aged |G*| for nine binders under study. A good correlation was observed between the measured and predicted values with

an R^2 higher than 0.9 for all binders. However, the model consistently underestimated the |G*| values as indicated by the trendline, especially at higher temperatures.

Figure 4.12 compares the predicted and measured δ values. The results displayed a poor correlation, with R^2 values lower than 0.5. The model overpredicted the results.

Default A and VTS parameters were used to compute viscosity values, which were then used to predict |G*| and δ values; therefore, the accuracy of these parameters is a significant determinant of the model's output. In our case, the model underestimated the |G*| values and overestimated the δ values, with some binders displaying poor agreement with measured δ values. This could be attributed to using the default A and VTS parameters as inputs in the prediction equations.

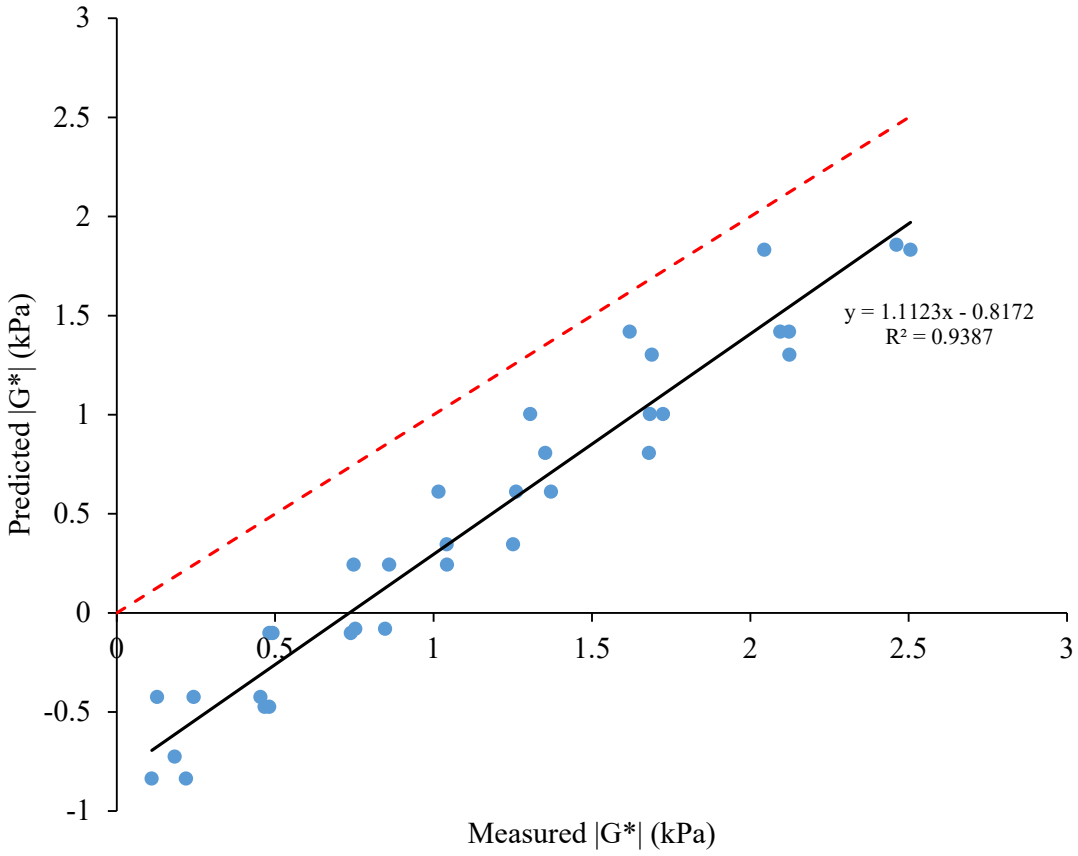

Figure 4.11: Predicted vs. Measured |G*|

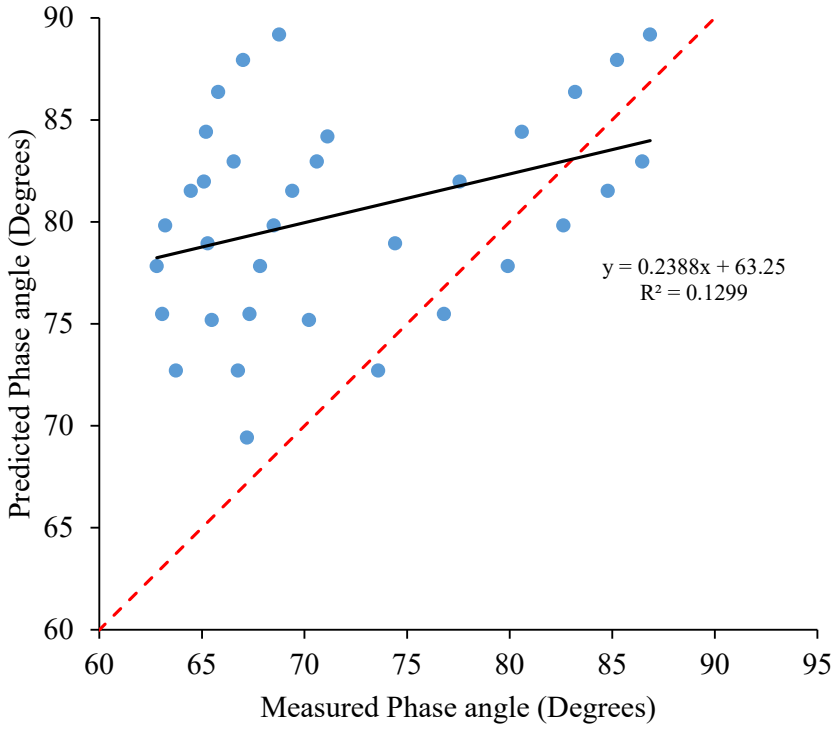

Figure 4.12: Predicted vs. Measured Phase angle

4.4 Binder Ranking

Table 4.2 presents results for five asphalt binders under four testing parameters. The first parameter specifies a maximum value of 5000 kPa for G*.sinδ values measured from DSR tests conducted on PAV-aged asphalt binders and measures fatigue resistance. The second parameter used the RTFO-aged binder test results to get the parameter |G*|/sin(δ) value, which should be higher than or equal to 2.20 kPa, indicating the binder's rutting resistance. The third and fourth parameters, MSCR and LAS, were used to evaluate the rutting and fatigue resistance of the asphalt binder, respectively. Table 4.2 shows all test results for five binders. Based on the test results in Table 4.2, the binders were ranked from A to E; the binders' rutting and fatigue resistance were ranked differently under different binder tests.

Table 4.2: Test Results of Five Binders

Tests	Important information	PG58H-34 HWY 32	PG58S-34 HWY 6	PG58H-34 HWY 94	PG58H-34 HWY 52	PG58S-34 HWY 1
LAS	Parameter A	24735970.49	4540515.55	66012308.37	25920029.00	215759.33
	Parameter B	-4.79	-4.70	-5.09	-4.99	-2.93
	Fatigue life at N_f=2.5%	304281.27	61390.50	622600.75	267818.40	14822.03
	Fatigue life at N_f=5%	10927.75	2367.32	18291.38	8426.45	1954.73
	Overall ranking	B	D	A	C	E
MSCR	Test temperature (°C)	58	58	58	58	58
	Percent non-recovery- J nr(0.1kpa)	0.65	1.21	0.31	0.36	2.51
	Percent non-recovery J_nr(3.2kpa)	1.10	2.47	0.63	1.01	3.28
	Percent difference of non-recoverable J_nr_diff	71.14	104.68	100.51	181.36	15.17
	Overall ranking	B	D	C	E	A
|G*|·sin(δ) (KPa)	Test temperature (°C)	4	7	1	-1	4
	|G*|·sin(δ)	5415.56	5031.12	6734.29	5137.37	5436.87
	Overall ranking	D	E	B	A	C
|G*|/sin(δ) (KPa)	Test temperature (°C)	64.00	64.00	64.00	64.00	64.00
	|G*|/sin(δ)	1.91	1.78	1.12	1.23	1.44
	Overall ranking	E	D	A	B	C

Note: Asphalt binders are ranked from A to E, A refers to the best, and E is the last one

4.4.1 Rutting Resistance of Binder Ranking

Rutting resistance |G*|/sin(δ) and MSCR test results were used for ranking the binders.

For |G*|/sin(δ), the correlation was done at 64ºC, PG 58H-34 - HWY 94 resisted rutting at 64ºC

better than the four binders and ranked A. PG 58H-34 HWY 32 performed poorly at 64^{o}C; therefore; it ranked E. MSCR test ranking shows that according to their rutting resistance, the percent difference of nonrecoverable result illustrate that PG 58S-34 HWY 1 has good resistance for rutting and ranked A while PG 58H-34 HWY 52 performed poorly the last and ranked E.

4.4.2 Fatigue Resistance of Binder Ranking

For fatigue resistance ranking |G*|. sinδ and LAS test results were used. |G*|. sinδ shows the temperature that corresponds to 5000 kPa. Generally, the lowest temperature indicated the best fatigue resistance. Table 4.2 illustrates that the binder used in PG 58H-34 - HWY 52 has good resistance to fatigue cracks and ranked the best, followed by PG 58H-34 - HWY 94, while PG 58S-34 - HWY 6 performed poorly and was ranked E.

LAS ranking was also used to rank the binders according to their fatigue resistance. Table 4.2 shows that the binder used in PG 58H-34 - HWY 94 has good resistance to fatigue cracks and is ranked the best, followed by PG 58H-34 - HWY 32. PG 58S-34 - HWY 1 performed poorly and was ranked E.

4.5 Dynamic Modulus Test Results

4.5.1 Dynamic Modulus

The |E*| test was performed at three temperatures (4, 20, and 35°C) and four loading frequencies (10, 1, 0.1, and 0.01 Hz). The results were averaged from the three replicates tested for each mixture.

Figures 4.13 to 4.15 present |E*| at three different temperatures. The measurements are from five HMA mixtures collected from the 2021 paving season. The values were plotted on a logarithmic scale. It can be observed that |E*| increases with an increase in loading frequency and temperature decrease. HWY 32_PG58S-28_15%RAP was observed to have the highest |E|

across all frequencies and temperatures, indicating that it had the highest stiffness. HWY 83_PG58H-34_10%RAP had the lowest |E| at 4° and 20°C, which was attributed to the mix having an NMAS of 9.5 mm, which was lower than n rest of the mixes, which all had NMAS of 12.5mm. At 35°C, HWY 28_PG58S-28_0% RAP had the lowest |E|, indicating that at higher temperatures, binder grading and percentage RAP content significantly contribute to the stiffness of the asphalt mix.

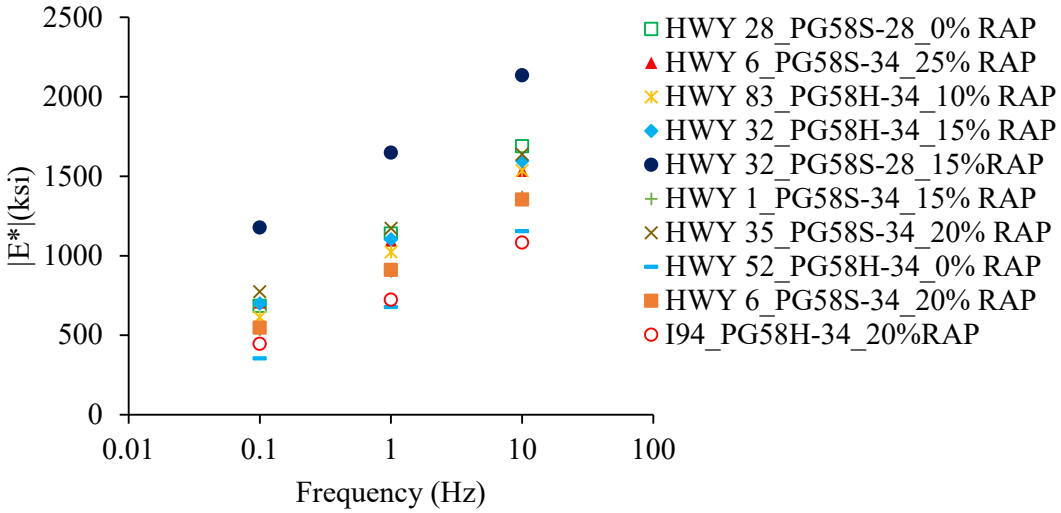

Figure 4.13: |E*| at 4°C

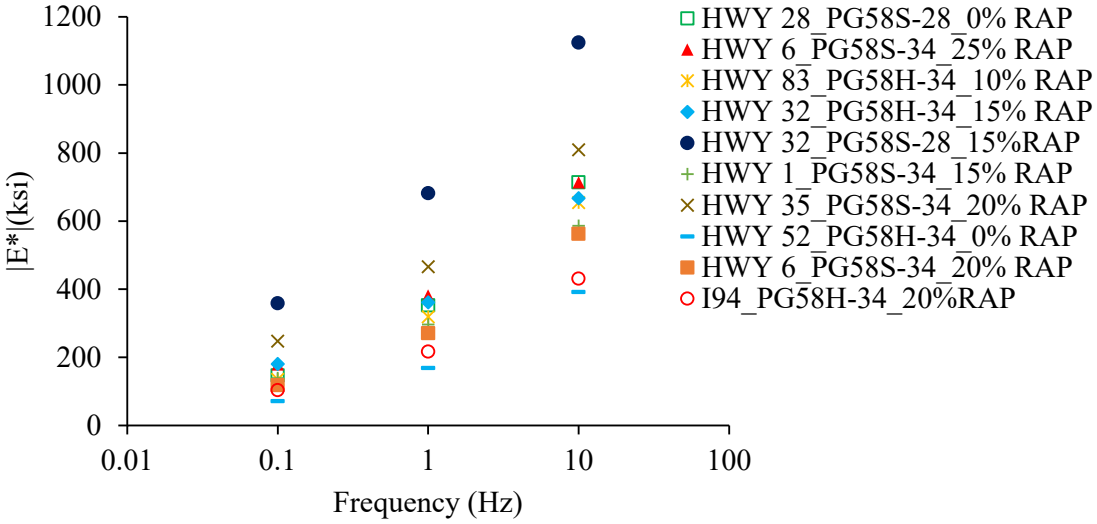

Figure 4.14: |E*| at 20°C

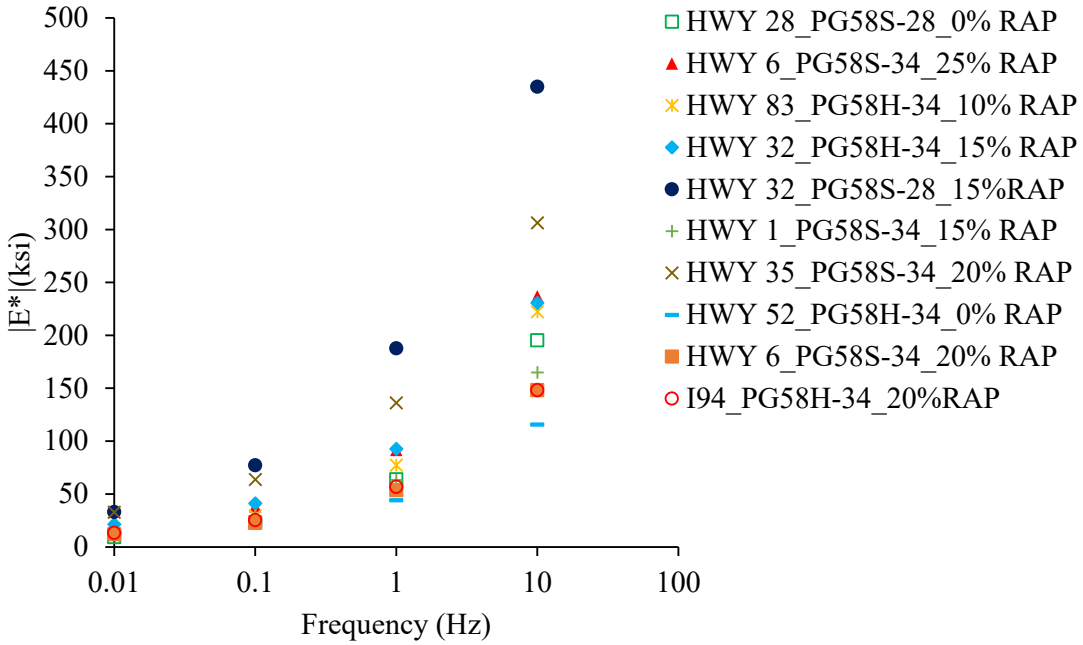

Figure 4.15: |E*| at 35°C

4.5.2 Phase Angle

The phase angle is measured simultaneously during the |E| tests as shown in Figure 4.16 to 4.18. The phase angle values varied from 9° and 40°. At 4° and 20°C, an increase in loading frequency corresponded with a decrease in phase angle. At 35°C, the trend shifted where the phase angle increased with loading frequency. These results have been observed in earlier research (Jamrah & Kutay, 2015; Mohammad et al., 2014; Pellinen, 2001). At temperatures lower than 35°C, asphalt binder determines the asphalt mixes' phase angle; at higher temperatures, the asphalt binder softens, and the aggregate skeleton determines the phase angle values (Zhao et al., 2017).

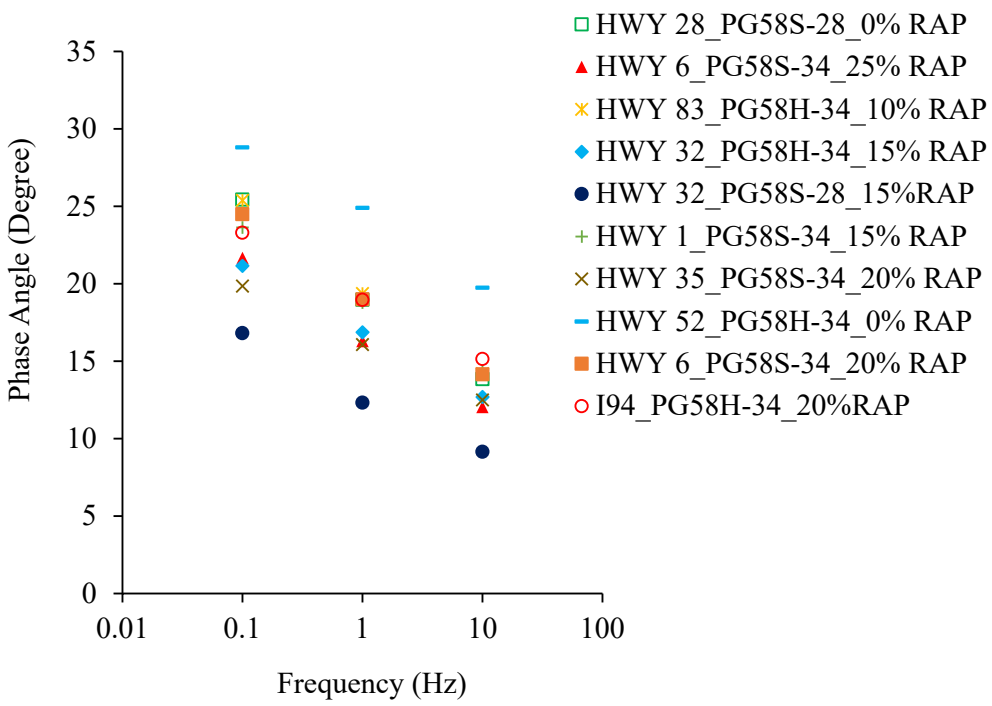

Figure 4.16: Phase Angle at 4°C

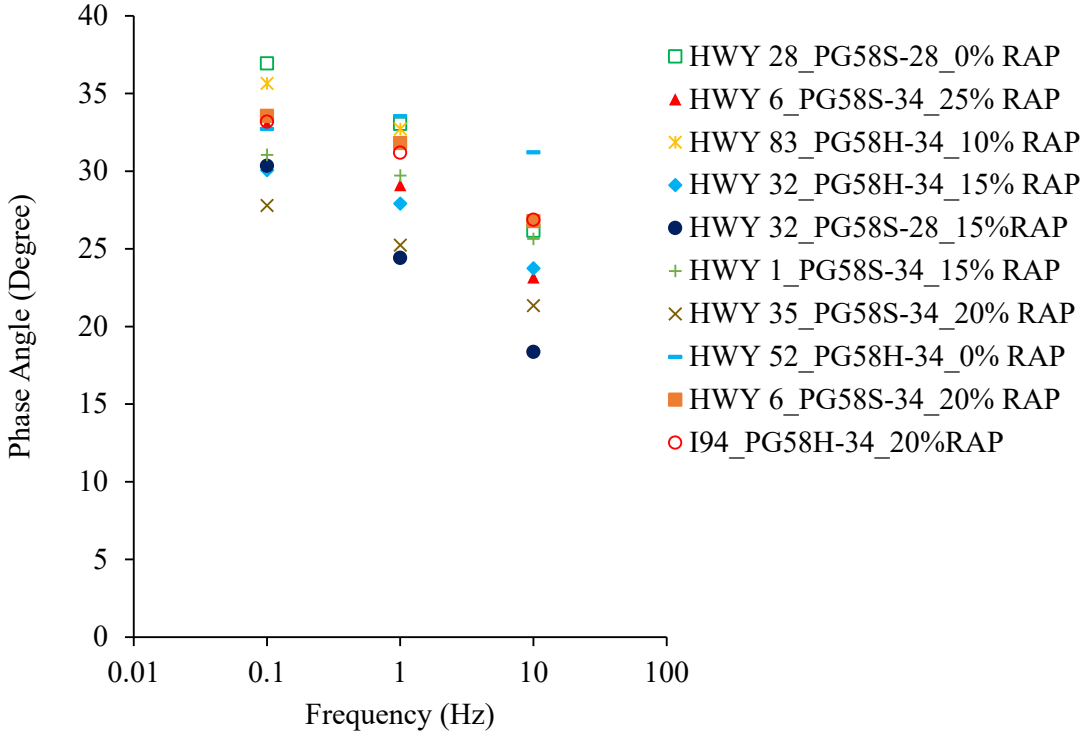

Figure 4.17: Phase Angle at 20°C

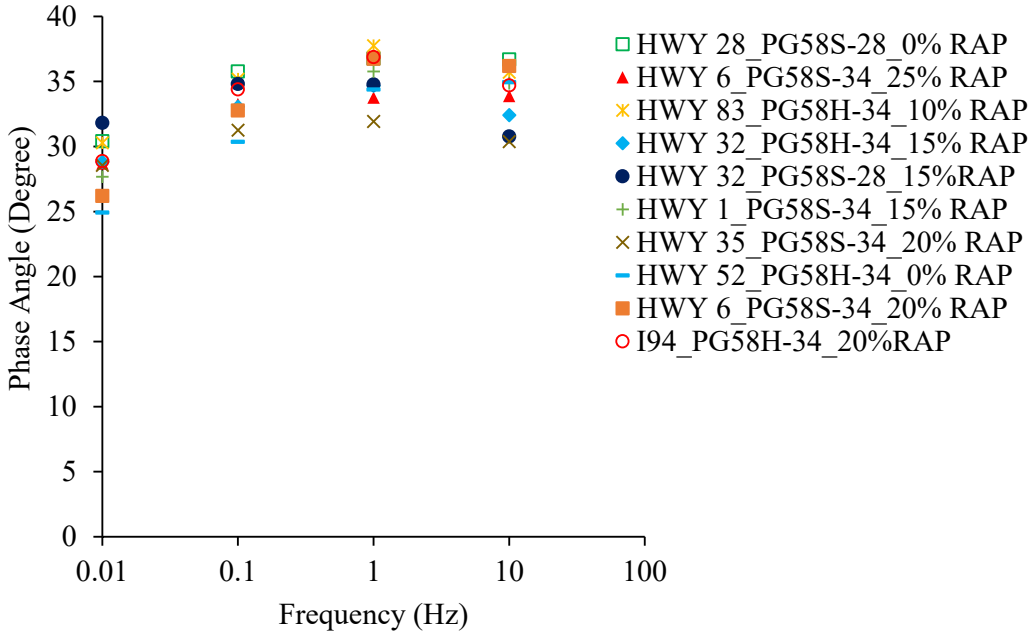

Figure 4.18: Phase Angle at 35°C

4.5.3 |E*| and Phase Angle Master Curves

HMA is a viscoelastic material; therefore, the limited range of loading frequency was extrapolated using the time-temperature superposition principle. The laboratory |E*| values were shifted with respect to the frequency/time axis using 20°C as the reference temperature. Figure 4.19 shows the |E| master curve obtained through this procedure. The |E*| master curve is a fundamental input for MEPDG structural analysis, which accounts for asphalt mix stiffness at a wide range of temperatures and loading frequencies.

From Figure 4.16, it was observed that HWY 28_PG58S-28_0% RAP HMA had the lowest |E*| at the lowest frequency, indicating a low rutting resistance, while HWY 32_PG58H-34_15% RAP and HWY 32_PG58S-28_15% RAP HMAs had the highest |E*| at the lowest frequency indicating a high rutting resistance. At high frequencies, the five mixes had almost similar |E*| values; thus, it was not possible to distinguish their resistance to fatigue cracking.

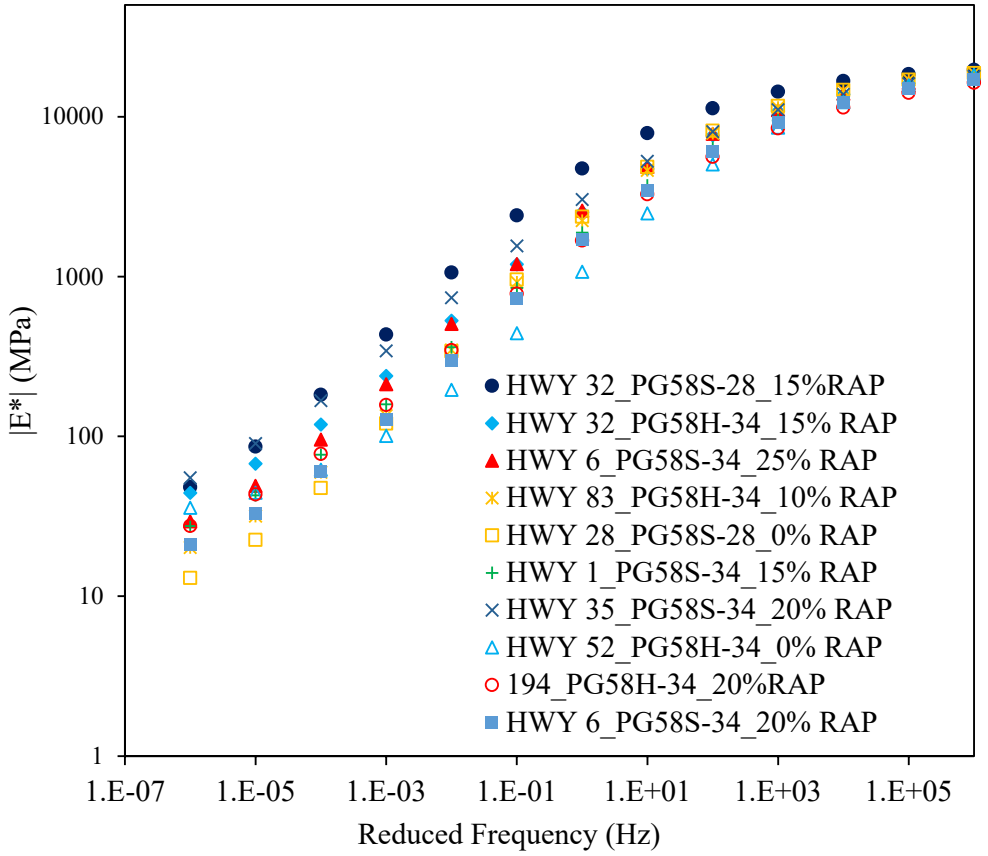

Figure 4.19: |E*| Master Curves (20°C reference temperature)

Figure 4.20 illustrates the master curve for the phase angle. The phase angle values are distributed in a parabolic manner because as loading frequency increases or temperature decreases, asphalt binder lends its elastic properties to the HMA, meaning that the phase angle decreases. However, as the frequency decreases or temperature increases, the phase angle increases up to 37°C, then it drops. This phenomenon implies that at high temperatures, the phase angle of the HMA is dependent on the aggregate skeleton. Although phase angle values are not required MEPDG inputs, studies have shown that they can be used to design low-noise asphalt mixes (Lou et al., 2022).

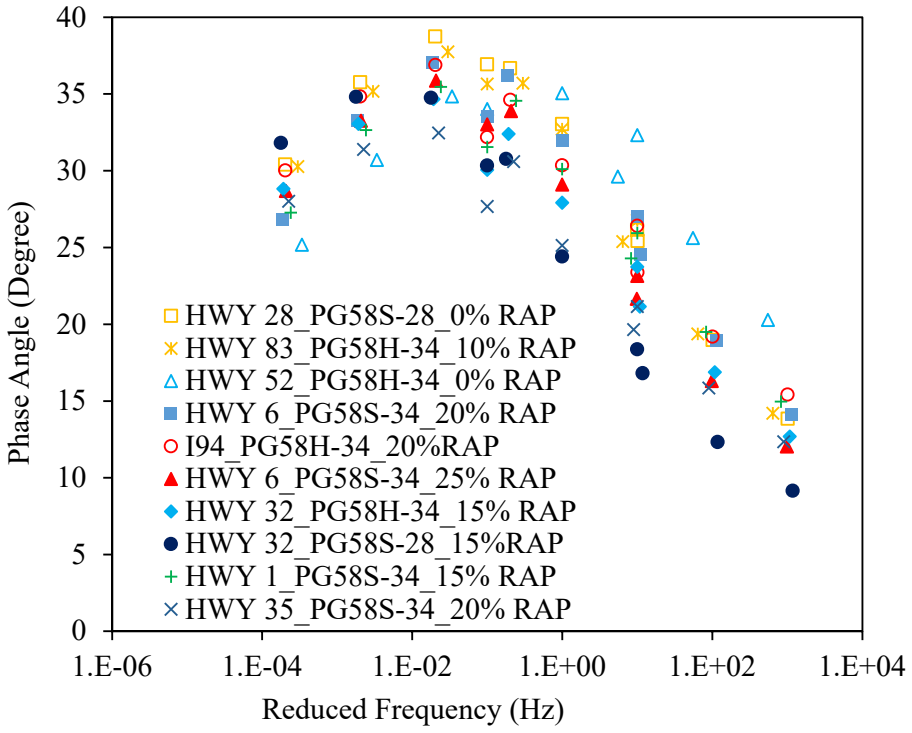

Figure 4.20: Phase Angle Master Curve (reference temperature 20°C)

4.5.4 Comparison of Laboratory and Level 2 Predicted Dynamic Moduli

Level 2 predictions were conducted using the original Witczak, modified Witczak, and Hirsch models given in Eqs. 2-19, 2-20, and 2-22, respectively. Laboratory-measured properties obtained from this project were used as model inputs. Figure 4.21 shows that the original Witczak model generally underpredicted |E*| values with an R^2 value of 0.923 and a S_e/S_y of 0.48. Figure 4.22 shows that the modified Witczak model had an R^2 value of 0.9146 and an S_e/S_y of 0.62 and similarly underpredicted at high |E*| values and overpredicted at lower |E*| values, suggesting a need for calibration. Figure 4.23 shows that the Hirsch model had an improved outcome with an R^2 value of 0.8373 and an S_e/S_y of 0.81. The Hirsch model had predictions on either side of the line of equality.

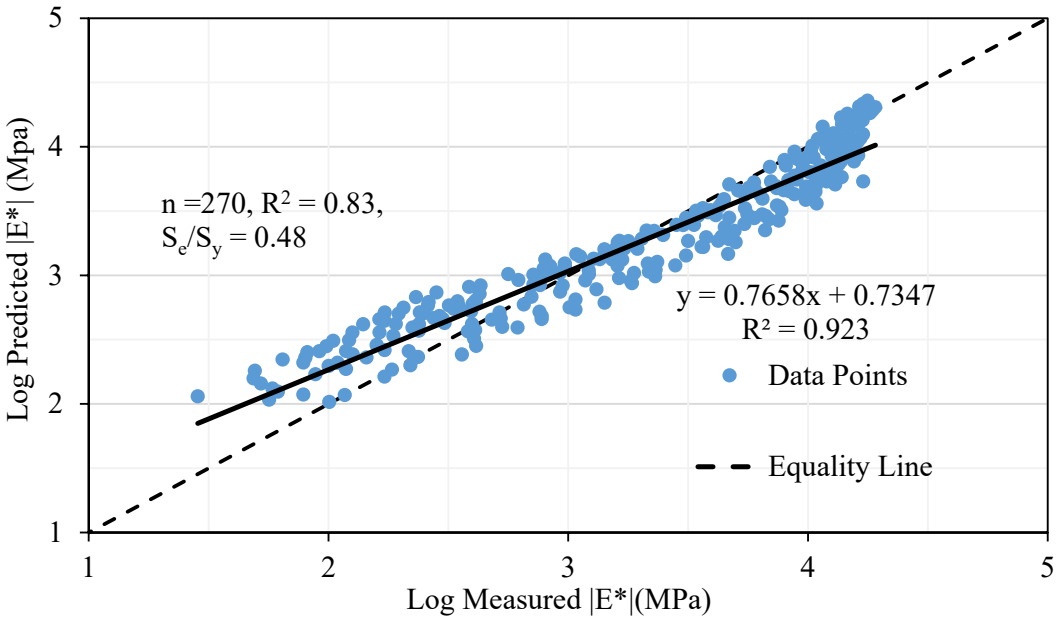

Figure 4.21: Predicted vs. Measured |E*| (Original Witczak Model)

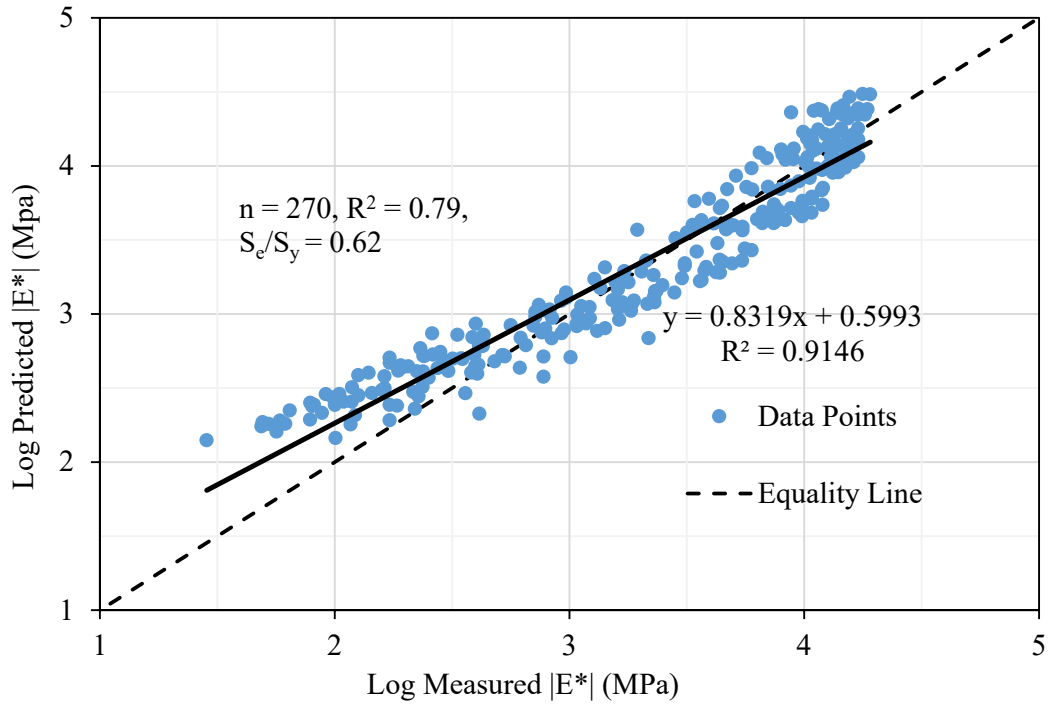

Figure 4.22: Predicted vs. Measured |E*| (Modified Witczak Model)

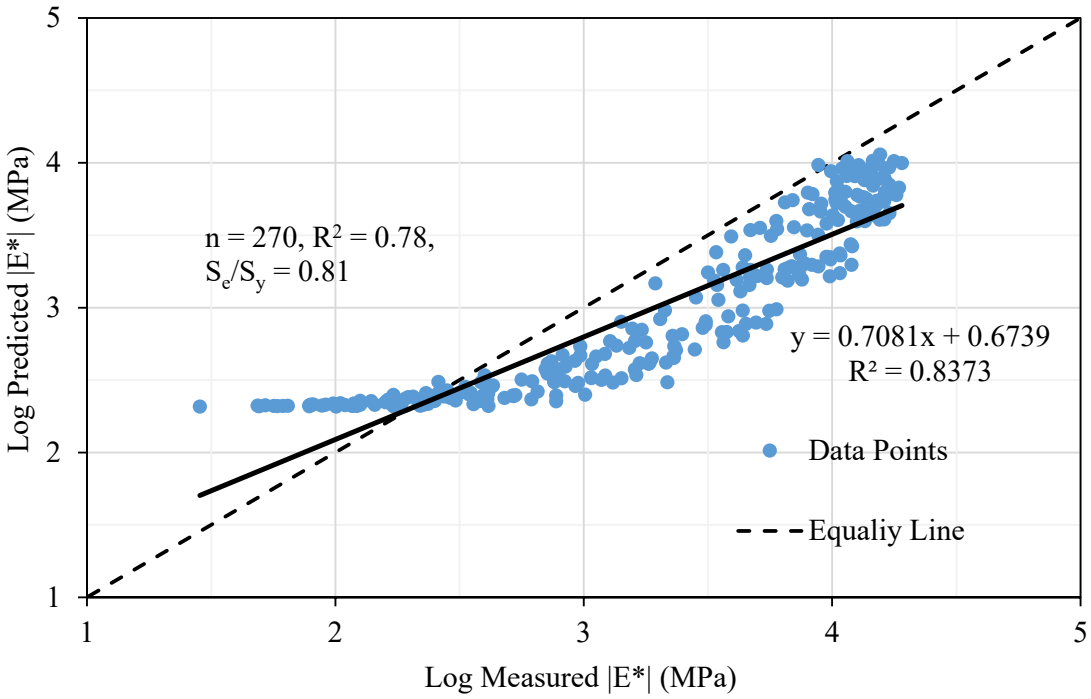

Figure 4.23: Predicted vs. Measured |E*| (Hirsch Model)

4.5.5 Comparison of Laboratory and Level 3 Predicted Dynamic Moduli

The same three models used for Level 2 predictions were used for Level 3 predictions. However, default binder properties were used as inputs according to MEPDG requirements. Figure 4.24 shows that the original Witczak model had an excellent match with measured |E*| values with an R^2 value of 0.939 and a low S_e/S_y of 0.29, meaning that the original Witczak model predictions can be used for pavement analysis of low-priority roads. Figure 4.25 shows that the modified Witczak model significantly overpredicted |E*|values with an R^2 value of 0.9376 and a high S_e/S_y of 0.82, meaning further investigation needs to be conducted to evaluate this model's performance. Figure 4.26 shows that the Hirsh model had a fair performance, with an R^2 value of 0.8373 and a S_e/S_y of 0.58. Generally, the original Witczak model is recommended for level 3 design.

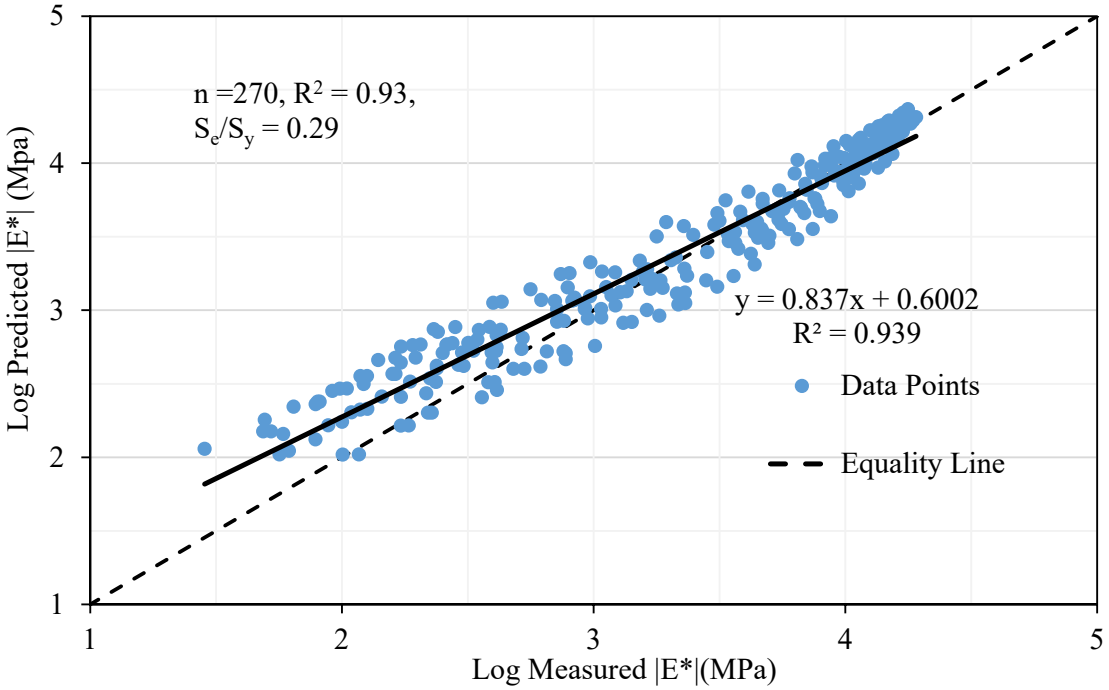

Figure 4.24: Predicted vs. Measured |E*| (Original Witczak Model)

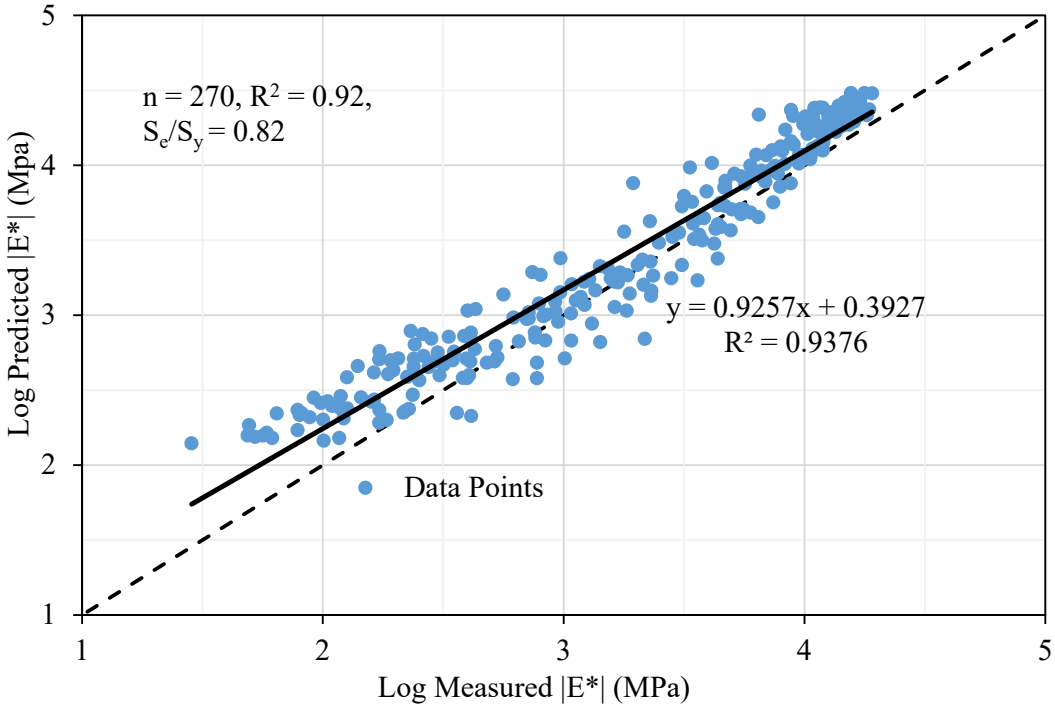

Figure 4.25: Predicted vs. Measured |E*| (Modified Witczak Model)

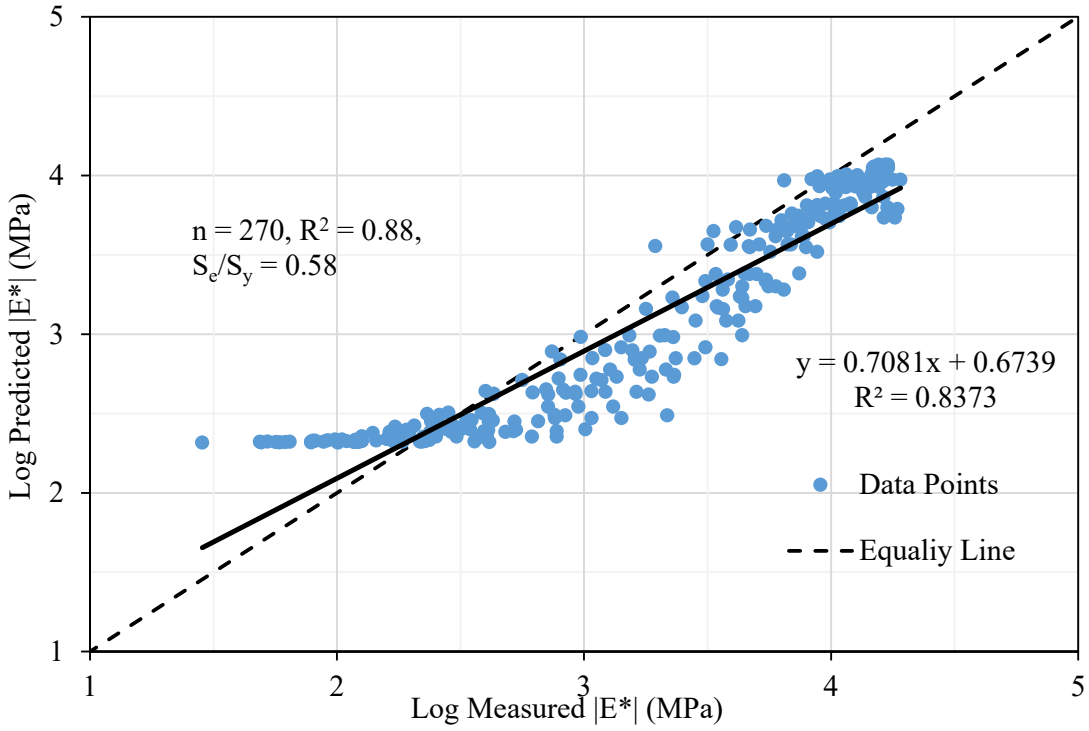

Figure 4.26: Predicted vs. Measured |E*| (Hirsch Model)

4.6 Flow Number Test Results

The flow number test indicates the rutting resistance of HMA at elevated temperatures. Table 4.4 and Figure 4.27 show the results of the Flow Number test. HWY 32_PG58H-34_15% RAP had the highest flow number, indicating that it can carry heavier traffic, as indicated in Table 4.3. HWY 28_PG58S-28_0% RAP had the lowest flow number, indicating a low rut resistance. These results indicate that the binder grading and the presence of RAP significantly affect the rut resistance of the HMA.

Table 4.3: Minimum Average Flow Number Requirements

Traffic level, million ESALs	HMA Minimum Average Flow Number
<3	
3 to <10	50
10 to <30	190
>=30	740

Table 4.4: Flow Number Results for the Ten Mixes

		Specimen				
Asphalt Mixture	ID	1	2	3	Average	Stdev
HWY 32_PG58H-34_15% RAP	HWY 32H	329	456	258	348	100.31
HWY 35_PG58S-34-20% RAP	HWY 35	285	385	236	302	75.94
I94_PG58H-34_20%RAP	I 94	153	88	100	114	34.59
HWY 32_PG58S-28_15% RAP	HWY 32S	115	105	81	100	17.47
HWY 83_PG58H-34_10% RAP	HWY 83	123	71	80	91	27.79
HWY 6_PG58S-34_25% RAP	HWY 6	75	52	57	61	12.10
HWY 52_PG58H-34_0% RAP	HWY 52	NA	55	62	59	4.95
HWY 1_PG58S-34_15% RAP	HWY 1	57	52	51	53	3.21
HWY 6_PG58S-34_20% RAP	HWY 6	44	36	42	41	4.16
HWY 28_PG58S-28_0% RAP	HWY 28	38	28	23	30	7.64

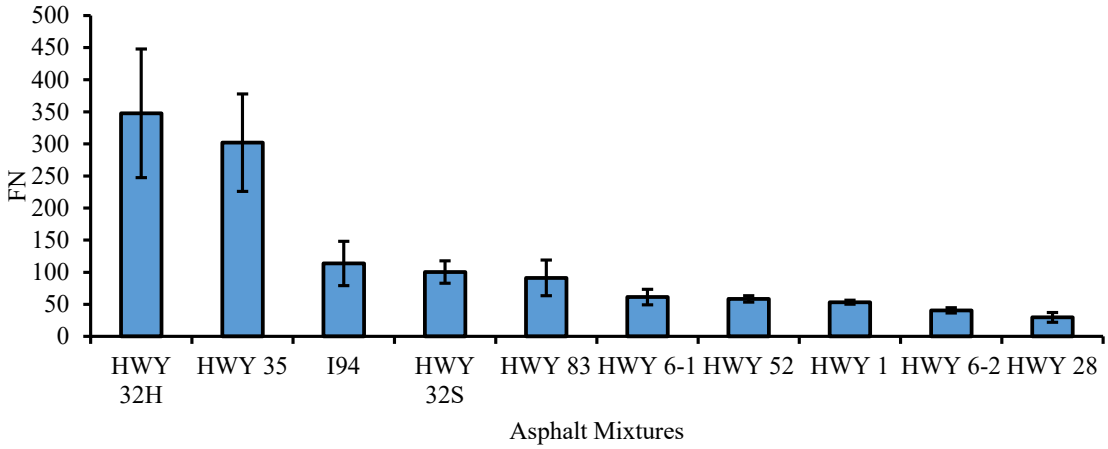

Figure 4.27: Flow Number Results for the Ten Mixes

4.7 iRLPD Test Results

The minimum strain rate (m^*) is the primary parameter measured by the iRLPD test. Table 4.5 lists the m^* values and power coefficients (b) for the ten asphalt mixtures under investigation. Plotting m^* against the product of the testing temperature (T) and deviator stress (P) produces the m^* master curve, as illustrated in Figure 4.28. The parameter b is a power function that describes the slope of the m* curves and can be calculated as shown in Eq. 4-1, where m^*_{600} is the minimum strain rate at 600 kPa and T is the test temperature.

$$b = \frac{log\ (m^{*}_{600} \times 1000)}{log\ (0.6 \times T)} \quad (4\text{-}1)$$

A steep slope corresponds with a larger b, indicating higher rutting susceptibility as exhibited by HWY 28_PG58S-28_0%RAP and HWY 6_PG58S-34_20%RAP. Conversely, HWY 32_PG58H-34_15%RAP and HWY 35_PG58S-34_20%RAP exhibit the best rutting performance, as their lower values indicate. Figure 4.29 illustrates the ranking of the mixtures based on b values, which typically range between 2 and 3, with the former indicating a very stiff material while the latter indicates a very soft material (AASHTO, 2020b). The higher rutting susceptibility exhibited by the HWY 28_PG58S-28_0%RAP mixture can be attributed to its use of a soft binder and no RAP.

Table 4.5: Minimum Strain Rates (m^{*}) and Power Coefficients (b)

Temperature, T (^{0}C)		54	54	54	
Pressure, P (kPa)		400	600	800	
TP (kPa)		21600	32400	43200	
Asphalt Mixtures	ID	Minimum strain rate (m^{*})			Power coefficient (b)
HWY6_PG58S-34_20% RAP	HWY 6-2	4.69	10.14	21	2.65
HWY52_PG58H-34_0% RAP	HWY 52	2.665	4.95	9.43	2.45
I 94_PG58H-34_20% RAP	I 94	3.665	6.785	12.645	2.54
HWY35_PG58S-34_20% RAP	HWY 35	1.905	3.025	4.69	2.30
HWY1_PG58S-34_15% RAP	HWY 1	2.925	6.645	13.305	2.53
HWY6_PG58S-34_25% RAP	HWY 6-1	2.76	6.265	13.55	2.51
HWY83_PG58H-34_10% RAP	HWY 83	3.76	7.69	15.07	2.57
HWY28_PG58S-28_0% RAP	HWY 28	4.975	12.285	30.38	2.71
HWY32_PG58H-34_15% RAP	HWY 32H	1.55	2.765	4.12	2.28
HWY32_PG58S-28_15% RAP	HWY 32S	2.43	4.76	8.665	2.43

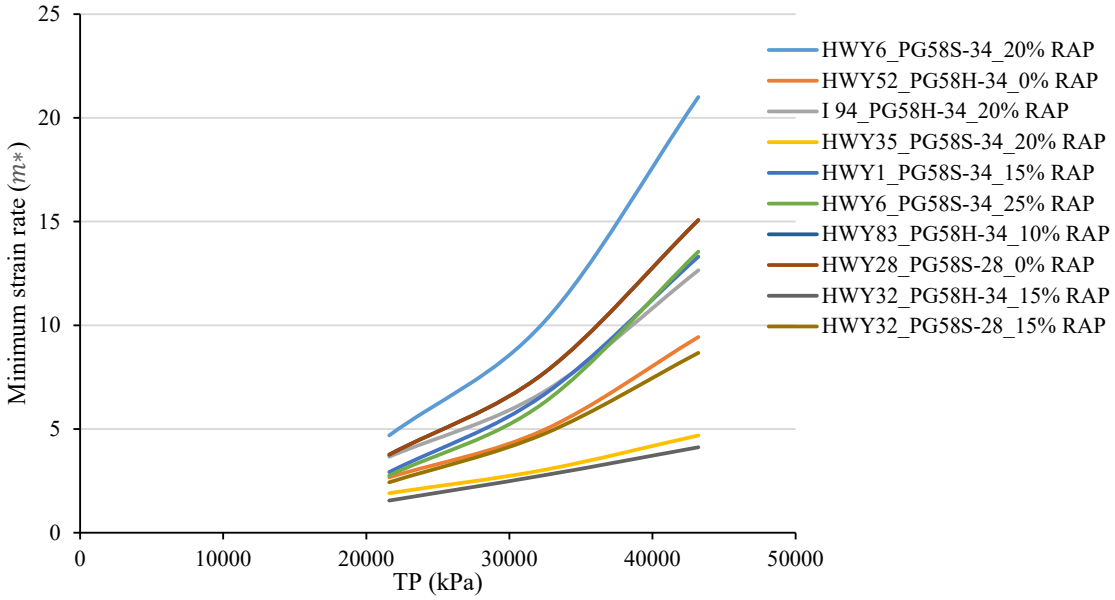

Figure 4.28: Master Curves of the 10 Asphalt Mixtures

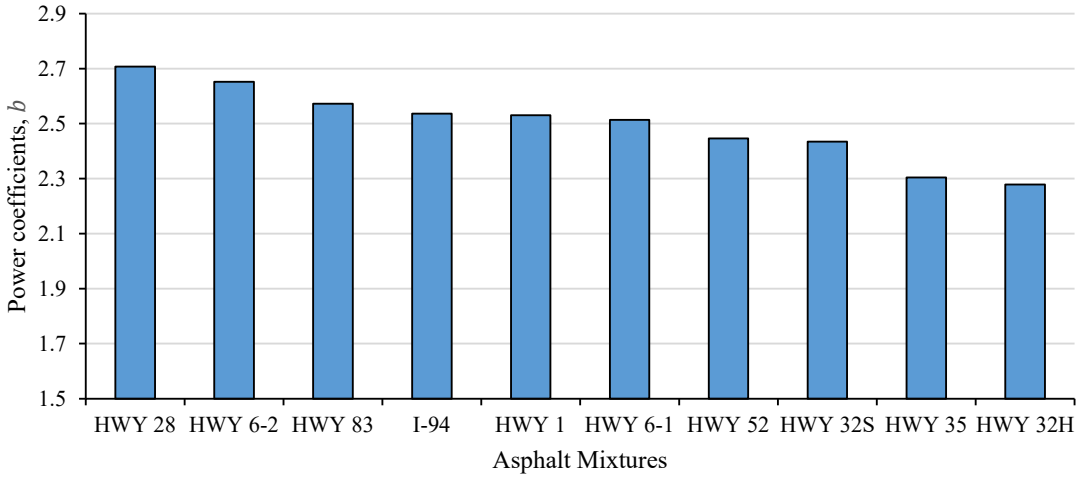

Figure 4.29: Asphalt Mixture Ranking Based on Coefficient *b*

Table 4.6 shows that RAP had a stiffening effect on all the mixtures containing RAP, as demonstrated by the increase in continuous performance PG and the traffic level. HWY 28 and HWY 52 had no RAP, and there was no change in their mixture environment PG or traffic level. The higher continuous PG exhibited by HWY 52 can be attributed to the stiff binder used in that mixture. It is important to note that the asphalt binders and the RAP used in the ten mixtures were obtained from different sources, creating a variability in the results.

Table 4.6: Minimum Strain Rates (m^*) and Power Coefficients (b)

Asphalt Mixture	ID	Continuous PG	Mixture Environment PG	Design ESAL (million)
HWY6_PG58S-34_20% RAP	HWY 6-1	61.8	58S	>1 to 3
HWY52_PG58H-34_0% RAP	HWY 52	70.6	58H	>3 to 10
I 94_PG58H-34_20% RAP	I 94	66.7	58H	>3 to 10
HWY35_PG58S-34_20% RAP	HWY 35	76.6	58E	>30
HWY1_PG58S-34_15% RAP	HWY 6-2	67.0	58H	>3 to 10
HWY6_PG58S-34_25% RAP	HWY 6-1	67.7	58H	>3 to 10
HWY83_PG58H-34_10% RAP	HWY 83	65.2	58H	>3 to 10
HWY28_PG58S-28_0% RAP	HWY 28	59.5	58S	>1 to 3
HWY32_PG58H-34_15% RAP	HWY 32H	77.7	58E	>30
HWY32_PG58S-28_15% RAP	HWY 32S	71.0	58H	>3 to 10
S=Standard traffic, H= Heavy traffic, V= Very heavy traffic, E=Extreme traffic				

Ranking the rutting susceptibility of the mixtures according to the iRLPD results revealed similarities with the FN ranking. HWY 32_PG58H-34_15%RAP and HWY35_PG58S-34_20%RAP exhibited high rutting resistance, while HWY 28_PG58S-28_0%RAP and HWY 6_PG58S-34_20%RAP exhibited low rutting susceptibility, indicating that the two tests could potentially be used interchangeably.

4.8 S-VECD Test

The S-VECD tests were performed at a loading frequency of 10Hz and a temperature of 12^0C for all eight mixes. Three replicates were tested for each mix at different strain levels, which is sufficient to rank the mixes according to their resistance to fatigue damage. Middle-failure and end-failure are two modes of failure that can occur on the test specimen during S-VECD testing, as illustrated in Figure 4.30.

Figure 4.30: Failure Locations of the S-VECD Tests: (a) middle-failure; (b) end-failure

Middle failures are desirable since they allow the LVDTs to capture damage propagation throughout the entire test. End-failures are not as good since the crack propagation develops beyond the LVDTs measurement range. Consequently, material stiffness cannot be calculated accurately, especially at the late stages of the tests. However, end-failure tests can still be used for damage characterization (Hou et al., 2010). Table 4.7 presents a summary of the test specimens, their air void percentage, strain level, number of cycles to failure (N_f), and failure locations. In this study, failure was defined as the point at which the phase angle starts to drop.

Table 4.7: Summary of S-VECD Cyclic Test Results and Failure Locations

Project	Specimen Name	Air Void (%)	Initial Strain	N_f	Failure Location
HWY 35_PG58S-34_20%RAP	35-1	7.0	160	5150	end
	35-2	6.7	160	24870	end
	35-3	6.7	160	76060	middle
HWY 32_PG58S-28_15%RAP	32S-1	7.9	160	28190	middle
	32S-2	7.8	160	14200	end
	32S-3	7.2	160	15180	middle
HWY 32_PG58H-34_15%RAP	32H-1	7.1	220	4680	middle
	32H-2	7.3	210	12720	end
	32H-3	6.8	210	21440	end
HWY 83_PG58H-34_25%RAP	83-1	7.3	220	27690	middle
	83-2	7.1	220	16430	middle
	83-3	7.0	240	15330	middle
HWY 28_PG58S-28_0%RAP	28-1	6.9	220	32860	end
	28-2	7.1	220	26040	middle
	28-3	6.6	160	>100000[a]	no failure
HWY 1_PG58S-34_15%RAP	1-1	7.0	220	19350	middle
	1-2	7.1	220	25910	middle
	1-3	7.1	220	65400	middle
HWY 6_PG58S-34_25%RAP	6-1	6.9	220	1550	end
	6-2	7.7	210	1970	middle
	6-3	7.7	180	8750	end
HWY 52_PG58H-34_0% RAP	52-1	6.8	300	60260	middle
	52-2	6.5	330	8690	middle
	52-3	6.5	330	10210	middle

[a]Test stopped at that number of loading cycle and specimend didn't fail

The pseudostiffness (C) and damage (S) are calculated according to the S-VECD model formulation (Underwood et al., 2012). Figure 4.31 summarizes the damage characteristic curves, C versus S, of the eight mixes tested. The last point on each curve signifies the pseudostiffness at failure (C_f). The asphalt mixes that displayed a higher stiffness from earlier dynamic modulus testing had higher material integrity at failure. These results are consistent with findings by Hou et al. (2010) and Norouzi and Kim (2017), which indicated that material integrity at the failure point increases as the material becomes stiffer. Therefore, higher C_f values indicate stiffer materials that are more susceptible to cracking. Out of the eight mixes

tested, HWY 35_PG58S-34_20%RAP and HWY 32_PG58S-28_15%RAP were more susceptible to fatigue cracking.

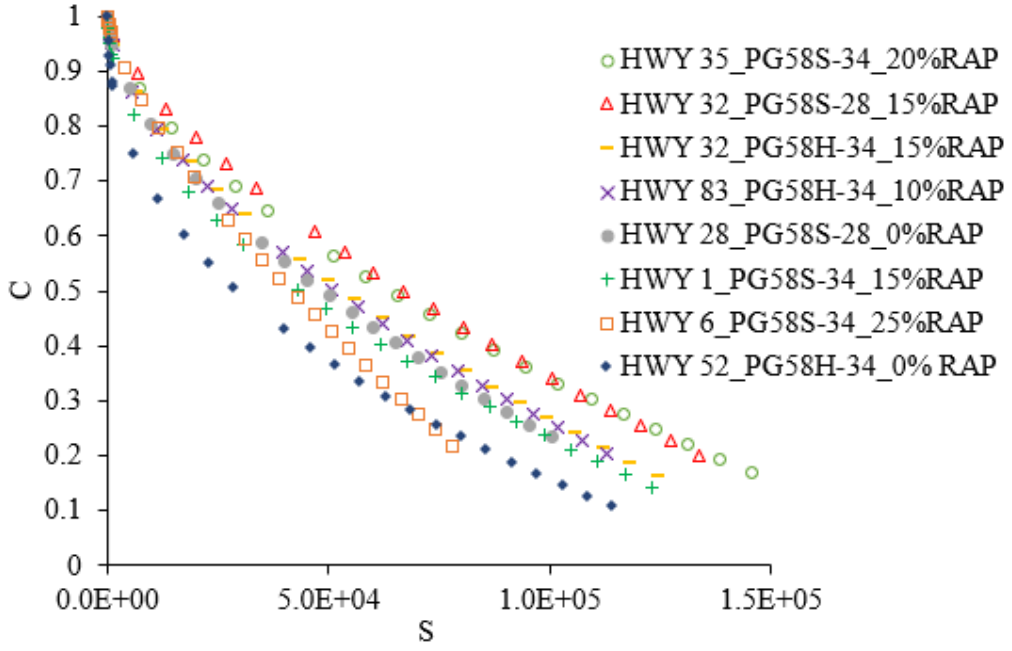

Figure 4.31: Damage Characteristic Curves

4.9 Creep Compliance

The creep compliance, D(t), was estimated from the measured dynamic modulus, |E*|, using the interconversion procedure. Figure 4.32 presents the creep compliance master curve for the 10 HMA mixes studied in this project. The two mixes with no RAP content, HWY 28 and HWY 52, had the highest creep compliance, indicating their heightened ability to dissipate thermal stresses and cycles of heating and cooling compared to the other mixes containing RAP. These findings match other studies that show RAP has a stiffening effect on asphalt mixes, reducing their thermal cracking resistance (Elkashef et al., 2018).

Figure 4.33 presents the estimated relaxation modulus master curve for the ten mixes. A steeper slope over time denotes a higher relaxation rate of the mix meaning lower thermal stresses will develop in the pavement. It is evident that HWY 28 and HWY 52 have a higher relaxation rate, while HWY 32 and both HWY 32s have the lowest relaxation rate.

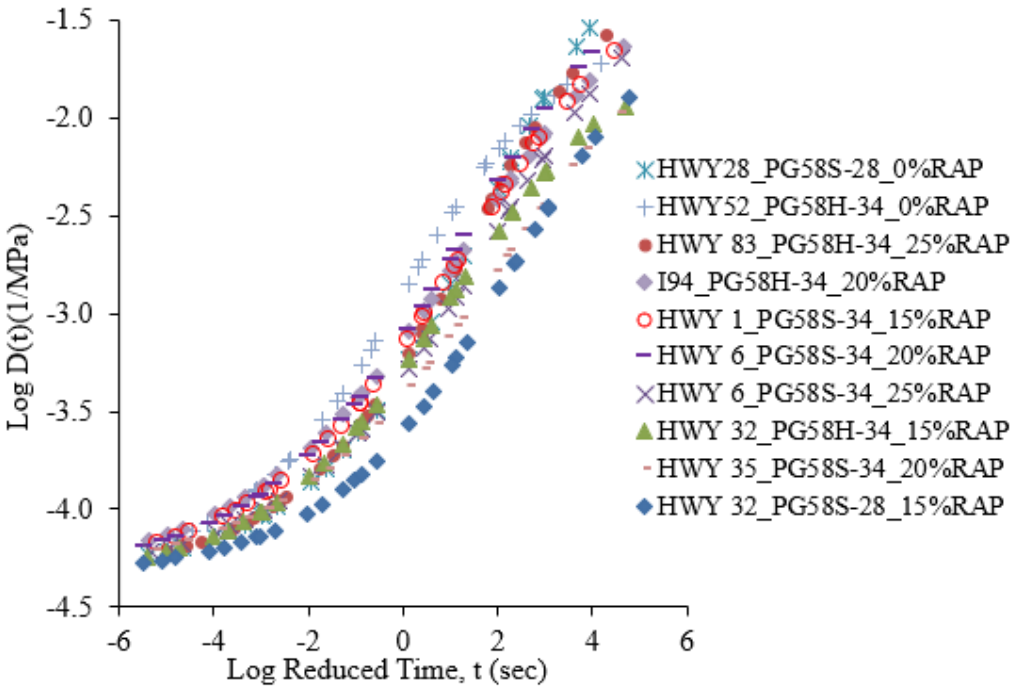

Figure 4.32: Creep Compliance Master Curve

Binder grade plays a central role in the thermal cracking resistance of an asphalt mix. The HWY 32 project used two binder grades, PG 58H-34 and PG 58S -28. The results reveal that the mix containing the stiffer binder, HWY32_PG58H-34_15%RAP, had lower creep compliance compared to HWY32_PG58H-34_15%RAP. These results seem contradictory. However, findings from the short-term (RTFO) binder grading showed that the PG58S-28 used in HWY 32 was stiffer compared to the PG58H-34 used in the same project. HWY 83 and I-94 were the only mixes with a NMAS of 9.5 mm and, it can be observed that these two mixes had a higher D(t) than the rest of the mixes containing RAP. It can be inferred that gradation has an effect on the thermal cracking resistance of asphalt mixes.

In summary, the binder grade, gradation, and RAP content were found to play an essential role in the thermal cracking resistance of the mixes.

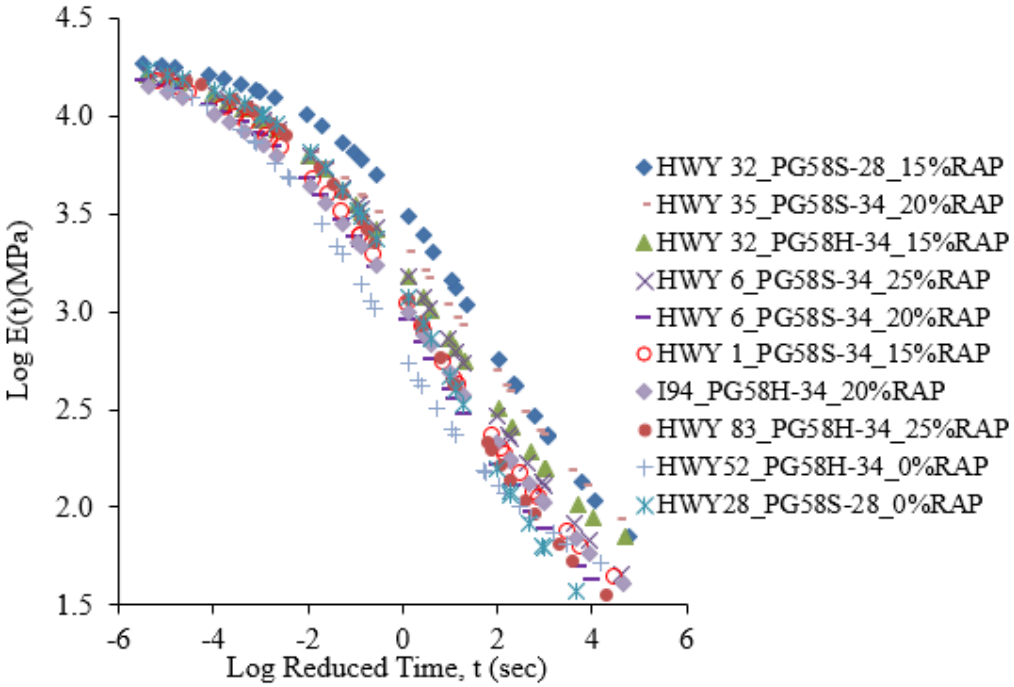

Figure 4.33: Creep Compliance Master Curve

Chapter Five

Conclusions, Recommendations, Limitations, and Future Work

5.1 Conclusions- Binder Testing

1. The measured viscosity of the binders was between the ranges of 0.170 ± 0.02 and 0.280 ± 0.03 Pa·s in all projects indicating that the sampled binders maintained their viscoelasticity even after undergoing long-term aging. However, binders with performance grade 58H-34 had higher viscosity values, especially after aging. The binders with PG grade 58H-34 are stiffer and are best suited to resist rutting. This explains their higher stiffness through the aging process.
2. The |G*| testing for the unaged binder revealed that the asphalt binder used in HWY 83, PG58H-34, had the highest |G*| values and that it could resist rutting up to a temperature of 64ºC. A significant difference was observed with the other binder with the same performance grade of PG58H-34 from HWY 32; it had the lowest |G*| values out of all the binders. The results demonstrated that the PG58H-34-HWY 32 binder could resist rutting up to 58ºC. This discrepancy illustrates the importance of undertaking local binder characterization to ascertain its performance. It is important to note that all the binders performed satisfactorily at high temperatures according to their performance grade. Binders designated as PG 58S-28 had higher δ values and, therefore, were less elastic than those designated as PG 58H-34.
3. The |G*| results for the RTFO-aged binders displayed a similar trend to those of the unaged binder. PG 58S-28-HWY 32, PG 58S-28-HWY 28, and PG 58H-34-HWY 83 displayed the highest |G*| values. PG 58H-34-HWY 52 had the lowest |G*|. All the binders failed at the same temperatures as the unaged binder, indicating that although short-term aging has a stiffening effect, the binders' viscoelastic properties remained

consistent. PG 58H-34-HWY 83 displayed should be recommended for use in highways anticipating high traffic loads because of its high |G*| and low δ.

4. PAV-aged binder testing revealed that PG 58H-34-HWY 32 and PG 58H-34-HWY 83 had the highest |G*| values, indicating that these binders underwent significant stiffening after long-term aging. PG 58H-34-HWY 52 displayed the lowest |G*|, indicating less sensitivity to aging.
5. Comparing the predicted |G*| with the RTFO-aged |G*| for the nine binders revealed a good correlation between the measured and predicted values with an R^2 higher than 0.9 for all binders. However, the model consistently underestimated the |G*| values, especially at higher temperatures.
6. A comparison between the predicted and measured δ values revealed that PG 58S-28-HWY 32, PG 58H-34-HWY 83, PG58S-28-HWY 28, and PG 58S-34-HWY 1 had good agreement with measured values with R^2 higher than 0.9 and PG 58H-34-HWY 52 and PG 58H-34-HWY 94 also shows good correlation R^2 values higher than 0.8. However, PG 58S-34-HWY 6 and PG 58H-34-HWY 32 displayed poor correlation with R^2 values lower than 0.5. The model overpredicted the δ results.
7. Using the |G*|/sinδ parameter showed that PG 58H-34-HWY 94 had the highest rutting resistance, while the MSCR test showed that PG 58S-34-HWY 1 was the most rutting-resistant binder. |G*|. sin(δ) parameter indicated that PG58H-34-HWY 52 had the highest fatigue resistance, while the LAS indicated that PG 58H-34-HWY 94 had the highest fatigue resistance. There was poor agreement between the binder grading results and the MSCR and LAS results.

5.2 Conclusions- Mix Testing

1. |E*| testing revealed that HWY35_PG58S-34_20%RAP had the highest stiffness at higher temperatures, indicating the highest rutting resistance out of all the ten mixes.

HWY 32_PG58S-28_15%RAP had higher stiffness than HWY 32_PG58H-34_15%RAP despite having a softer binder. HWY28_PG58S-28_0%RAP had the lowest stiffness at high temperatures, showing that including RAP in the mixes has a stiffening effect.

2. The Original Witczak model gave excellent prediction of the E* values for all mixes and is recommended for predicting E* values for level 3 of the MEPDG.
3. Flow number testing showed that HWY 32_PG58H-34_15%RAP displayed the highest stiffness, followed by HWY35_PG58S-34_20%RAP, and HWY 32_PG58H-34_15%RAP came in third. Although the ranking of the mixes is not similar to the E* results, it should be noted that they are the same ones that displayed higher stiffness than the rest. HWY28_PG58S-28_0%RAP had the lowest flow number, which is consistent with E* testing results.
4. Ranking the rutting susceptibility of the mixtures according to the iRLPD results revealed similarities with the FN ranking. HWY 32_PG58H-34_15%RAP and HWY35_PG58S-34_20%RAP exhibited high rutting resistance, while HWY 28_PG58S-28_0%RAP and HWY 6_PG58S-34_20%RAP exhibited low rutting susceptibility, indicating that the two tests could be used interchangeably.
5. The S-VECD testing revealed that mixes displaying a higher stiffness from earlier dynamic modulus testing had higher material integrity at failure, which indicated that material integrity at the failure point increases as the material becomes stiffer. Out of the eight mixes tested, HWY 35_PG58S-34_20%RAP and HWY 32_PG58S-28_15%RAP were more susceptible to fatigue cracking.
6. The E* values were successfully converted to creep compliance using the approximate interconversion procedure. It is important to measure creep compliance in the

laboratory to ascertain the accuracy of the predicted values before adoption into the MEPDG.

5.3 Recommendations

Based on this study, the following recommendations can be made:

- Generating A and VTS values for local binders to improve the |G*| and δ predictions and provide a substitute for laboratory measurements.
- Asphalt binders were ranked under different binder tests. Studies have shown that the LAS and MSCR tests are superior to the Superpave parameters |G*|. sin(δ) and |G*|/sin(δ). Therefore, further investigation is needed to evaluate the discrepancy obtained in these tests.
- Determine the mixes' creep compliance to ascertain the accuracy of the predicted values from the interconversion procedure.
- |E*| Predictions for level 2 were not as good as level 3. Further investigation needs to be conducted, and possibly, the binders should be measured over a more comprehensive range of loading frequency to provide a broader range of input to evaluate the model better.

5.4 Limitations

Default A and VTS parameters were used to compute viscosity values, which were then used to predict |G*| and δ values; therefore, the accuracy of these parameters is a significant determinant of the model's output. The model underestimated the |G*| values and overestimated the δ values, with some binders displaying poor agreement with measured δ values. This could be attributed to using the default A and VTS parameters as inputs in the prediction equations.

MSCR and LAS tests were conducted for five binders to compare their results to binder grading results preliminarily.

5.5 Future Work

1. The experiments were conducted on nine binders. MSCR and LAS tests will be conducted to rank the binders according to rutting and fatigue cracking (Johnson & Bahia, 2010).
2. Determination of Creep Compliance of the mixes in order to ascertain the accuracy of the predicted values obtained from the interconversion procedure.

REFERENCES

AASHTO. (2008). *Mechanistic-empirical pavement design guide: A manual of practice* (Interim). American Association of State Highway and Transportation Officials.

AASHTO. (2014a). *AASHTO TP 70-14: Standard Method of Test for Multiple Stress Creep Recovery (MSCR) Test of Asphalt Binder Using a Dynamic Shear Rheometer (DSR)*. American Association of State Highway and Transportation Officials.

AASHTO. (2014b). *AASHTO TP 101-14: Estimating Damage Tolerance of Asphalt Binders Using the Linear Amplitude Sweep*. American Association of State Highway and Transportation Officials.

AASHTO. (2017a). *AASHTO R 83: Standard Practice for Preparation of Cylindrical Performance Test Specimens Using the Superpave Gyratory Compactor (SGC)*. American Association of State Highway and Transportation Officials.

AASHTO. (2017b). *AASHTO R 84-17: Standard Practice for Developing Dynamic Modulus Master Curves for Asphalt Mixtures Using the Asphalt Mixture Performance Tester (AMPT)*. American Association of State Highway and Transportation Officials.

AASHTO. (2017c). *AASHTO T 378: Standard Method of Test for Determining the Dynamic Modulus and Flow Number for Asphalt Mixtures Using the Asphalt Mixture Performance Tester (AMPT)*. American Association of State Highway and Transportation Officials.

AASHTO. (2019). *AASHTO T 316-19: Standard Method of Test for Viscosity Determination of Asphalt Binder Using Rotational Viscometer*. American Association of State Highway and Transportation Officials.

AASHTO. (2020a). *AASHTO T 315-20 Standard Method of Test for Determining the Rheological Properties of Asphalt Binder Using a Dynamic Shear Rheometer (DSR)*. American Association of State Highway and Transportation Officials.

AASHTO. (2020b). *AASHTO TP 116-20 Standard Method of Test for Rutting and Fatigue Resistance of Asphalt Mixtures Using Incremental Repeated Load Permanent Deformation (iRLPD)*.

AASHTO. (2020c). *AASHTO TP107-18: Determining the Damage Characteristic Curve and Failure Criterion Using the Asphalt Mixture Performance Tester (AMPT) Cyclic Fatigue Test*. AASHTO TP 107, Washington, DC.

AASHTO. (2021a). *AASHTO R 28-21: Standard Practice for Accelerated Aging of Asphalt Binder Using a Pressurized Aging Vessel (PAV)*. American Association of State Highway and Transportation Officials.

AASHTO. (2021b). *AASHTO T 240-21: Standard Method of Test for Effect of Heat and Air on a Moving Film of Asphalt (Rolling Thin-Film Oven Test)*. American Association of State Highway and Transportation Officials.

Al-Khateeb, G., Shenoy, A., Gibson, N., & Harman, T. (2006). A new simplistic model for dynamic modulus predictions of asphalt paving mixtures. *Journal of the Association of Asphalt Paving Technologists*, *75*.

Andrei, D., Witczak, M. W., & Mirza, M. W. (1999). Development of a revised predictive model for the dynamic (complex) modulus of asphalt mixtures. *Development of the 2002 Guide for the Design of New and Rehabilitated Pavement Structures, NCHRP*.

ARA, E. C. D. (2004). *Guide for Mechanistic–Empirical Design of New and Rehabilitated Pavement Structures.* (NCHRP 1-37A Final Rep.). National Cooperative Highway Research Program, Transportation Research Board.

ASTM. (2015). *ASTM D4402-06: Standard Test Method for Viscosity Determination of Asphalt at Elevated Temperatures Using a Rotational Viscometer*. ASTM International.

Azari, H., & Mohseni, A. (2013). Permanent deformation characterization of asphalt mixtures by using incremental repeated load testing. *Transportation Research Record*, *2373*(1), 134–142.

Bari, J., & Witczak, M. (2006). Development of a New Revised Version of the Witczak E* Predictive Model for Hot Mix Asphalt Mixtures (With Discussion). *Journal of the Association of Asphalt Paving Technologists*, *75*.

Bari, J., & Witczak, M. W. (2007). New predictive models for viscosity and complex shear modulus of asphalt binders: For use with mechanistic-empirical pavement design guide. *Transportation Research Record*, *2001*(1), 9–19.

Bhasin, A., Button, J. W., & Chowdhury, A. (2005). *Evaluation of selected laboratory procedures and development of databases for HMA*. Texas Transportation Institute, Texas A & M University System.

Birgisson, B., Roque, R., Kim, J., & Pham, L. V. (2004). *The use of complex modulus to characterize the performance of asphalt mixtures and pavements in Florida*.

Bonaquist, R. F. (2008). *Refining the simple performance tester for use in routine practice* (Vol. 614). Transportation Research Board.

Bonaquist, R. F. (2012). *Evaluation of Flow Number (FN) as a discriminating HMA mixture property*. Wisconsin Highway Research Program.

Bonaquist, R. F., & Christensen, D. W. (2005). Practical procedure for developing dynamic modulus master curves for pavement structural design. *Transportation Research Record*, *1929*(1), 208–217.

Brown, E. R., Kandhal, P. S., Roberts, F. L., Kim, Y. R., Lee, D.-Y., & Kennedy, T. W. (2009). *Hot mix asphalt materials, mixture design, and construction*. NAPA research and education foundation.

Cao, W., Norouzi, A., & Kim, Y. R. (2016). Application of viscoelastic continuum damage approach to predict fatigue performance of Binzhou perpetual pavements. *Journal of Traffic and Transportation Engineering (English Edition)*, *3*(2), 104–115. https://doi.org/10.1016/j.jtte.2016.03.002

Ceylan, H., Schwartz, C. W., Kim, S., & Gopalakrishnan, K. (2009). Accuracy of predictive models for dynamic modulus of hot-mix asphalt. *Journal of Materials in Civil Engineering*, *21*(6), 286–293.

Christensen, D. W., Pellinen, T., & Bonaquist, R. F. (2003). Hirsch model for estimating the modulus of asphalt concrete. *Journal of the Association of Asphalt Paving Technologists*, *72*.

Colbert, B., & You, Z. (2012). The properties of asphalt binder blended with variable quantities of recycled asphalt using short term and long term aging simulations. *Construction and Building Materials*, *26*(1), 552–557. https://doi.org/10.1016/j.conbuildmat.2011.06.057

D'Angelo, J., Kluttz, R., Dongre, R. N., Stephens, K., & Zanzotto, L. (2007). Revision of the superpave high temperature binder specification: The multiple stress creep recovery test (with discussion). *Journal of the Association of Asphalt Paving Technologists*, *76*.

Diaz, L. G., & Archilla, A. R. (2013). From Testing to Design: An Easy Way Use and Interpret the Results from the Asphalt Mixture Performance Tester (AMPT). *International Journal of Pavement Research and Technology*, *6*(5), 527.

Dondi, G., Vignali, V., Pettinari, M., Mazzotta, F., Simone, A., & Sangiorgi, C. (2014). Modeling the DSR complex shear modulus of asphalt binder using 3D discrete element approach. *Construction and Building Materials*, *54*, 236–246. https://doi.org/10.1016/j.conbuildmat.2013.12.005

Dougan, C. E., Stephens, J. E., Mahoney, J., & Hansen, G. (2003). *E*-dynamic modulus test protocol: Problems and solutions*. University of Connecticut. Connecticut Transportation Institute.

Elkashef, M., Williams, R. C., & Cochran, E. (2018). Investigation of fatigue and thermal cracking behavior of rejuvenated reclaimed asphalt pavement binders and mixtures. *International Journal of Fatigue*, *108*, 90–95. https://doi.org/10.1016/j.ijfatigue.2017.11.013

Gedafa, D. S., Hossain, M., & Romanoschi, S. A. (2009). *Field verification of KDOT's Superpave mixture properties to be used as inputs in the NCHRP mechanistic-empirical pavement design guide.* Kansas. Dept. of Transportation.

Hintz, C., & Bahia, H. (2013). Simplification of Linear Amplitude Sweep Test and Specification Parameter. *Transportation Research Record: Journal of the Transportation Research Board*, *2370*(1), 10–16. https://doi.org/10.3141/2370-02

Hou, T., Underwood, B. S., & Kim, Y. R. (2010). Fatigue performance prediction of North Carolina mixtures using simplified viscoelastic continuum damage model. *Journal of the Association of Asphalt Paving Technologists*, *79*, 35–80.

Islam, M. R., Kalevela, S. A., & Nesselhauf, S. K. (2019). Sensitivity of the flow number to Mix factors of Hot-Mix Asphalt. *Infrastructures*, *4*(2), 34.

Jamrah, A., & Kutay, M. E. (2015). Investigation of Different Methods for Obtaining Asphalt Mixture Creep Compliance for Use in Pavement Mechanistic–Empirical Design Software.

Transportation Research Record: Journal of the Transportation Research Board, *2524*(1), 100–109. https://doi.org/10.3141/2524-10

Johnson, C., & Bahia, H. U. (2010). Evaluation of an accelerated procedure for fatigue characterization of asphalt binders. *Submitted for Publication in Road Materials and Pavement Design*.

Kaloush, K., Witczak, M. W., Roque, R., Brown, S., D'Angelo, J., Marasteanu, M., & Masad, E. (2002). Tertiary flow characteristics of asphalt mixtures. *Asphalt Paving Technology 2002*, 248–280.

Kim, Y. R., King, M., & Momen, M. (2005). Typical dynamic moduli values of hot mix asphalt in North Carolina and their prediction. *Transp. Res. Board 84th Annu. Meet. Compend. Pap*, 5–2568.

Kim, Y. R., & Little, D. N. (1990). One-Dimensional Constitutive Modeling of Asphalt Concrete. *Journal of Engineering Mechanics*, *116*(4), 751–772. https://doi.org/10.1061/(ASCE)0733-9399(1990)116:4(751)

Kim, Y. R., Seo, Y., King, M., & Momen, M. (2004). Dynamic modulus testing of asphalt concrete in indirect tension mode. *Transportation Research Record*, *1891*(1), 163–173.

Kutay, M. E., & Jamrah, A. (2013). *Preparation for Implementation of the Mechanistic-Empirical Pavement Design Guide in Michigan: Part 1–HMA Mixture Characterization.*

Li, Q. J., Wang, K. C. P., Yang, G., Zhan, J. Y., & Qiu, Y. (2019). Data needs and implementation of the Pavement ME Design. *Transportmetrica A: Transport Science*, *15*(1), 135–164. https://doi.org/10.1080/23249935.2018.1504254

Lou, K., Xiao, P., Kang, A., Wu, Z., & Dong, X. (2022). Effects of asphalt pavement characteristics on traffic noise reduction in different frequencies. *Transportation Research Part D: Transport and Environment*, *106*, 103259. https://doi.org/10.1016/j.trd.2022.103259

Mohammad, L. N., Kim, M., Raghavendra, A., & Obulareddy, S. (2014). *Characterization of Louisiana asphalt mixtures using simple performance tests and MEPDG.* Louisiana. Dept. of Transportation and Development.

Mohammad, L. N., Wu, Z., Myers, L., Cooper, S., & Abadie, C. (2005). A practical look at the simple performance tests: Louisiana's experience (with discussion). *Journal of the Association of Asphalt Paving Technologists*, *74*.

Norouzi, A., & Kim, Y. R. (2017). Mechanistic evaluation of fatigue cracking in asphalt pavements. *International Journal of Pavement Engineering*, *18*(6), 530–546. https://doi.org/10.1080/10298436.2015.1095909

Park, S. W., & Schapery, R. (1999). Methods of interconversion between linear viscoelastic material functions. Part I—A numerical method based on Prony series. *International Journal of Solids and Structures*, *36*(11), 1653–1675.

Pellinen, T. K. (2001). *Investigation of the use of dynamic modulus as an indicator of hot-mix asphalt performance*. Arizona State University.

Pellinen, T. K., & Witczak, M. W. (2002). Stress Dependent Master Curve Construction for Dynamic Modulus. *Journal of the Association of Asphalt Paving Technologists*, *71*, 281–309.

Tran, N., & Hall, K. (2005). *Evaluating the predictive equation in determining dynamic moduli of typical asphalt mixtures used in Arkansas*.

Underwood, B. S., Baek, C., & Kim, Y. R. (2012). Simplified Viscoelastic Continuum Damage Model as Platform for Asphalt Concrete Fatigue Analysis. *Transportation Research Record: Journal of the Transportation Research Board*, *2296*(1), 36–45. https://doi.org/10.3141/2296-04

Wang, H.-P., Guo, Y.-X., Wu, M.-Y., Xiang, K., & Sun, S.-R. (2021). Review on structural damage rehabilitation and performance assessment of asphalt pavements. *REVIEWS ON ADVANCED MATERIALS SCIENCE*, *60*(1), 438–449. https://doi.org/10.1515/rams-2021-0030

Williams, R. C., Robinette, C. J., Bausano, J., & Breakah, T. (2007). *Testing Wisconsin asphalt mixtures for the AASHTO 2002 mechanistic design procedure*.

Witczak, M. W., Roque, R., Pellinen, T. K., El-Basyouny, M., & Von Quitus, H. (2002). *Simple Performance Test for Superpave Mix Design* (465). Transportation Research Board.

Yao, H., You, Z., Li, L., Shi, X., Goh, S. W., Mills-Beale, J., & Wingard, D. (2012). Performance of asphalt binder blended with non-modified and polymer-modified nanoclay. *Construction and Building Materials*, *35*, 159–170. https://doi.org/10.1016/j.conbuildmat.2012.02.056

Yu, H., & Shen, S. (2013). A micromechanical based three-dimensional DEM approach to characterize the complex modulus of asphalt mixtures. *Construction and Building Materials*, *38*, 1089–1096. https://doi.org/10.1016/j.conbuildmat.2012.09.036

Yusoff, N. I. Md., Shaw, M. T., & Airey, G. D. (2011). Modelling the linear viscoelastic rheological properties of bituminous binders. *Construction and Building Materials*, *25*(5), 2171–2189. https://doi.org/10.1016/j.conbuildmat.2010.11.086

Zeiada, W., Liu, H., Ezzat, H., Al-Khateeb, G. G., Shane Underwood, B., Shanableh, A., & Samarai, M. (2022). Review of the Superpave performance grading system and recent developments in the performance-based test methods for asphalt binder characterization. *Construction and Building Materials*, *319*, 126063. https://doi.org/10.1016/j.conbuildmat.2021.126063

Zhang, J., Alvarez, A. E., Lee, S. I., Torres, A., & Walubita, L. F. (2013). Comparison of flow number, dynamic modulus, and repeated load tests for evaluation of HMA permanent deformation. *Construction and Building Materials*, *44*, 391–398.

Zhao, S., Liu, J., Li, P., & Saboundjian, S. (2017). Dynamic Modulus Characterization of Alaskan Asphalt Mixtures for Mechanistic-Empirical Pavement Design. *Journal of Materials in Civil Engineering*, *29*(11), 04017213. https://doi.org/10.1061/(ASCE)MT.1943-5533.0002069

Zhou, F., Scullion, T., & Sun, L. (2004). Verification and modeling of three-stage permanent deformation behavior of asphalt mixes. *Journal of Transportation Engineering*, *130*(4), 486–494.

Appendix A: Binder Complex Shear Moduli (|G*|) and Phase Angles

Tables A1, A2, and A3 present |G*| and δ values measured at unaged, short-term-aged, and long-term aged conditions. The figures highlighted in red indicate temperatures at which the binders failed to meet the threshold requirement.

Table A.1. Measured (|G*|) and Phase Angles for Unaged Binders

Binder	Temperature (°C)	|G*| (kPa)	δ Degrees	|G*|/sin(δ) (kPa)
HWY-6-PG58S-34	34	23.51	70.89	24.88
	40	10.32	71.43	10.88
	46	4.80	72.34	5.04
	52	2.35	73.63	2.45
	58	1.20	75.23	1.24
	64	0.64	77.03	0.65
HWY-83-PG58H-34	34	60.17	70.91	63.67
	40	25.22	70.86	26.70
	46	11.24	70.85	11.90
	52	5.40	71.11	5.71
	58	2.77	71.59	2.92
	64	1.48	71.86	1.56
	70	0.82	71.67	0.86
HWY-28-PG58S-28	34	50.31	80.71	50.98
	40	17.61	83.26	17.74
	46	6.58	85.32	6.60
	52	2.63	86.87	2.63
	58	1.12	88.03	1.12
	64	0.52	88.75	0.52
HWY-32-PG58H-34	34	16.91	66.98	18.37
	40	8.28	66.65	9.02
	46	4.27	67.16	4.63
	52	2.28	68.56	2.45
	58	1.24	70.65	1.32
	64	0.69	73.30	0.73
HWY-32-PG58S-28	34	52.33	80.93	52.99
	40	18.00	83.48	18.12
	46	6.70	85.51	6.72
	52	2.60	87.04	2.60
	58	1.11	88.16	1.11
	64	0.52	88.85	0.52
HWY 1-PG58S-34	34	29.22	74.53	30.31
	40	12.60	77.09	12.92

	46	5.61	79.67	5.70
	52	2.57	82.02	2.60
	58	1.23	84.00	1.23
	64	0.61	85.54	0.61
HWY 52-PG58H-34	34	18.24	67.06	19.80
	40	8.92	66.22	9.74
	46	4.61	66.00	5.05
	52	2.48	66.47	2.70
	58	1.37	67.69	1.47
	64	0.78	69.70	0.83
HWY 35-PG58S-34	34	21.56	67.75	23.29
	40	10.13	67.41	10.97
	46	5.05	67.81	5.46
	52	2.66	69.07	2.85
	58	1.45	71.10	1.54
	64	0.81	73.75	0.85
I 94-PG58H-34	34	25.41	63.42	25.36
	40	11.86	63.90	11.90
	46	6.28	64.96	6.29
	52	3.46	66.34	3.46
	58	1.95	67.55	1.95
	64	1.13	68.58	1.12
	70	0.67	69.12	0.66

Table A.2. Measured (|G*|) and Phase Angles for RTFO-Aged Binders

Binder	**Temperature (°C)**	**|G*| (kPa)**	**δ Degrees**	**|G*|/sin(δ) (kPa)**
HWY-6-PG58S-34	34	48.90	65.29	53.83
	40	22.55	65.10	24.86
	46	11.01	65.20	12.13
	52	5.67	65.80	6.22
	58	3.03	67.01	3.29
	64	1.66	68.77	1.78
HWY-83-PG58H-34	34	124.42	66.76	135.40
	40	53.03	67.32	57.47
	46	23.51	67.84	25.39
	52	11.04	68.51	11.86
	58	5.48	69.41	5.86
	64	2.85	70.60	3.02
	70	1.52	72.13	1.60
	34	132.69	73.60	138.32

HWY-28-PG58S-28	40	48.23	76.81	49.54
	46	18.24	79.92	18.52
	52	7.25	82.63	7.31
	58	3.03	84.79	3.05
	64	1.34	86.47	1.34
HWY-32-PG58H-34	34	41.64	63.74	46.43
	40	20.20	63.07	22.66
	46	10.37	62.80	11.67
	52	5.60	63.22	6.27
	58	3.11	64.47	3.45
	64	1.75	66.55	1.91
HWY-32-PG58S-28	34	133.02	74.42	138.10
	40	47.93	77.57	49.08
	46	17.84	80.60	18.08
	52	7.04	83.20	7.09
	58	2.93	85.24	2.94
	64	1.29	86.85	1.29
HWY 1-PG58S-34	34	74.65	68.96	79.98
	40	32.25	71.44	34.02
	46	14.20	74.20	14.75
	52	6.43	76.97	6.60
	58	2.97	79.59	3.02
	64	1.42	81.90	1.44
HWY 52-PG58H-34	34	44.07	63.61	49.20
	40	21.10	62.80	23.72
	46	10.73	62.26	12.13
	52	5.76	62.31	6.51
	58	3.20	63.14	3.59
	64	1.78	64.83	1.97
HWY 35-PG58S-34	34	47.02	64.34	52.16
	40	21.74	64.15	24.16
	46	10.70	64.34	11.87
	52	5.56	65.20	6.13
	58	2.98	66.87	3.24
	64	1.64	69.36	1.76
I 94-PG58H-34	34	48.85	61.28	55.71
	40	24.29	61.51	27.64
	46	12.49	62.01	14.14
	52	6.66	62.80	7.49
	58	3.68	63.86	4.10
	64	2.09	65.15	2.30
	70	1.21	66.66	1.32

Table A.3. Measured (|G*|) and Phase Angles for PAV-Aged Binders

Binder	Temperature (°C)	|G*| (kPa)	Phase angle δ	|G*|. sin(δ)z]l (kPa)
HWY-6-PG58S-34	22	469.57	61.99	414.28
	19	789.48	60.82	688.70
	16	1327.80	59.33	1140.97
	13	2235.38	57.52	1470.48
	10	3763.44	55.37	3093.81
	7	6312.51	52.93	5031.12
HWY-83-PG58H-34	22	959.68	59.67	827.78
	19	1656.70	57.17	1391.07
	16	2782.65	54.60	2266.02
	13	3983.24	51.87	3598.54
	10	7461.99	48.90	5616.05
HWY-28-PG58S-28	22	1211.75	63.83	1142.80
	19	2152.31	60.60	1997.53
	16	3666.10	57.27	3338.44
	13	6128.85	53.70	5453.37
HWY-32-PG58H-34	22	353.23	60.83	309.83
	19	583.94	59.68	507.43
	16	960.48	58.17	823.48
	13	1583.94	56.26	1333.01
	10	1624.61	54.01	2155.39
	7	4328.47	51.45	3446.60
	4	7058.58	25.03	5415.56
HWY-32-PG58S-28	22	1243.39	63.49	1112.57
	19	2229.77	60.21	1934.93
	16	3849.25	56.83	3221.66
	13	6500.04	53.26	5208.68
HWY 1-PG58S-34	22	476.07	61.64	324.70
	19	792.67	60.25	533.13
	16	1294.99	58.61	861.10
	13	2104.96	56.68	1385.58
	10	3424.55	54.46	2212.27
	7	5497.83	51.97	3491.06
	4	8767.47	49.27	5436.87
HWY 52-PG58H-34	22	440.62	62.09	389.39
	19	722.47	61.11	632.57
	16	1185.83	59.77	1024.56
	13	1953.28	58.03	1657.08
	10	3246.24	55.90	2687.99

	7	5339.19	53.45	4289.23
	4	8740.82	50.72	6765.98
HWY 35-PG58S-34	22	402.05	62.43	356.43
	19	677.63	61.22	593.99
	16	1146.10	59.68	989.36
	13	1950.64	57.70	1648.86
	10	3302.69	55.32	2716.20
	7	5550.46	52.59	4408.65
	4	9189.05	49.56	6993.40
I94-PG58H-34	19	727.49	54.88	595.00
	16	1143.13	53.25	915.93
	13	1778.12	51.48	1391.16
	10	2755.56	49.51	2095.47
	7	4270.85	47.38	2607.05
	4	6542.19	45.13	4636.52
	1	9908.15	42.82	6734.29

Appendix B: E* MEPDG Inputs

Table B1. HWY32_PG58S-28_15%RAP

Temperature (C)	|E*| MEPDG Inputs from Master Curve (ksi)					
	25 Hz	10 Hz	5 Hz	1 Hz	0.5 Hz	0.1 Hz
-10	2771	2697	2634	2455	2364	2116
4.4	2234	2084	1960	1642	1496	1150
21.1	1274	1078	935	634	522	315
37.8	450	336	265	147	112	60
54.4	110	77	59	32	25	15

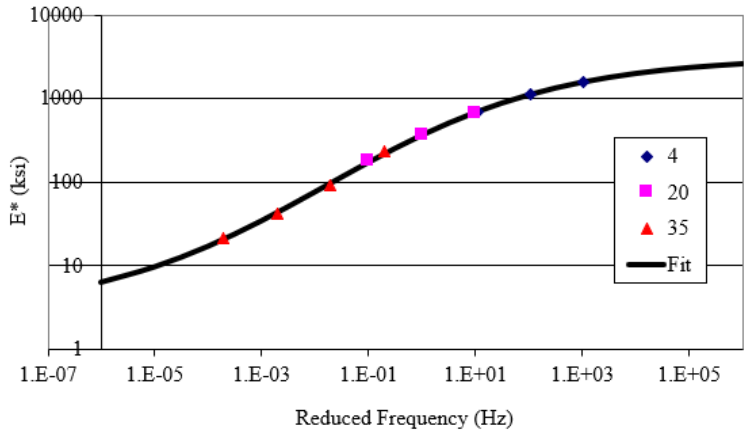

Final Parameters:	Max	3144.28	ksi
	Min	2.6753	ksi
	Beta	-0.8268	
	Gamma	-0.4637	
	EA	197846	
Fit	R^2	0.99794	
	Se/Sy	0.03206	

Figure B.1. Optimized |E*| Master Curve (HWY32_PG58S-28_15%RAP)

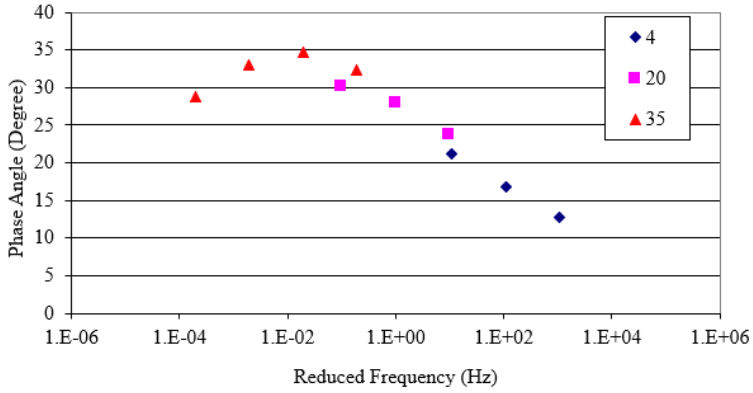

Figure B.1.1. Optimized Phase Angle Master Curve (HWY32_PG58S-28_15%RAP)

Table B2: HWY32_PG58H-34_15%RAP

	|E*| MEPDG Inputs from Master Curve (ksi)					
Temperature (C)	25 Hz	10 Hz	5 Hz	1 Hz	0.5 Hz	0.1 Hz
-10	2467	2354	2258	2006	1884	1579
4.4	1738	1559	1421	1097	962	674
21.1	788	635	530	333	268	156
37.8	233	171	134	76	59	34
54.4	60	44	35	21	17	11

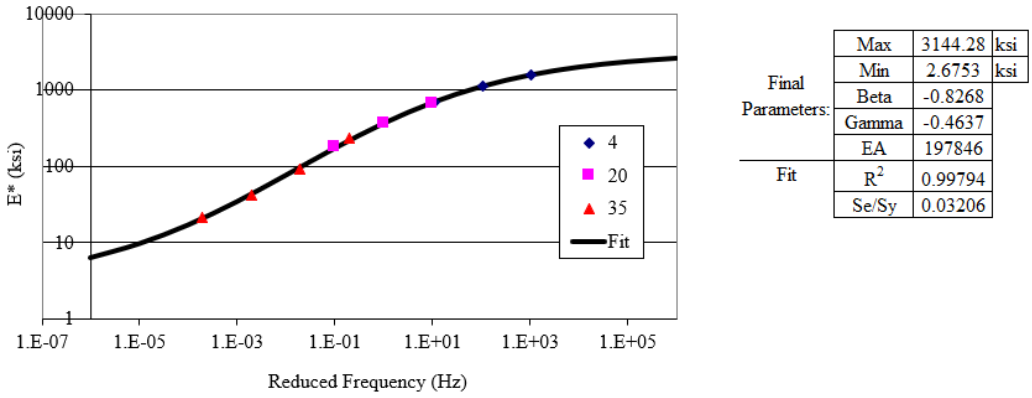

Figure B.2. Optimized |E*| Master Curve (HWY32_PG58H-34_15%RAP)

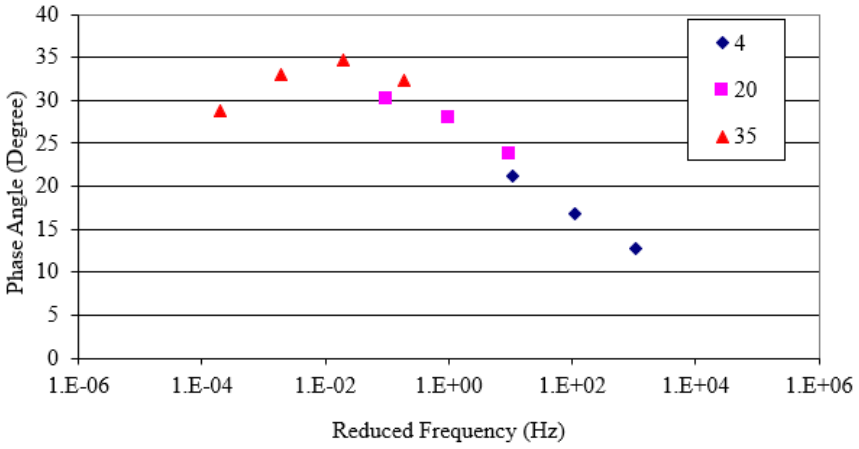

Figure B.2.1. Optimized Phase Angle Master Curve (HWY32_PG58H-34_15%RAP)

Table B.3. HWY83_PG58H-34_10%RAP

	|E*| MEPDG Inputs from Master Curve (ksi)					
Temperature (C)	25 Hz	10 Hz	5 Hz	1 Hz	0.5 Hz	0.1 Hz
-10	2462	2331	2221	1928	1787	1437
4.4	1731	1532	1377	1019	872	570
21.1	792	620	506	295	228	119
37.8	233	163	123	62	46	24
54.4	56	38	29	15	12	7

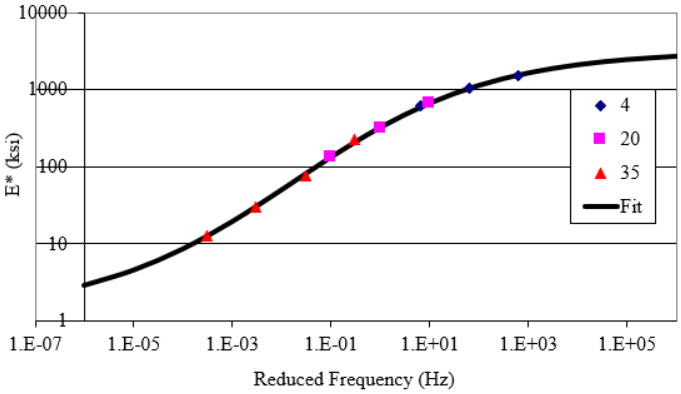

Final Parameters:	Max	3178.18	ksi
	Min	1.28079	ksi
	Beta	-0.8868	
	Gamma	-0.5036	
	EA	175709	
Fit	R^2	0.99856	
	Se/Sy	0.02686	

Figure B.3. Optimized |E*| Master Curve (HWY83_PG58H-34_10%RAP)

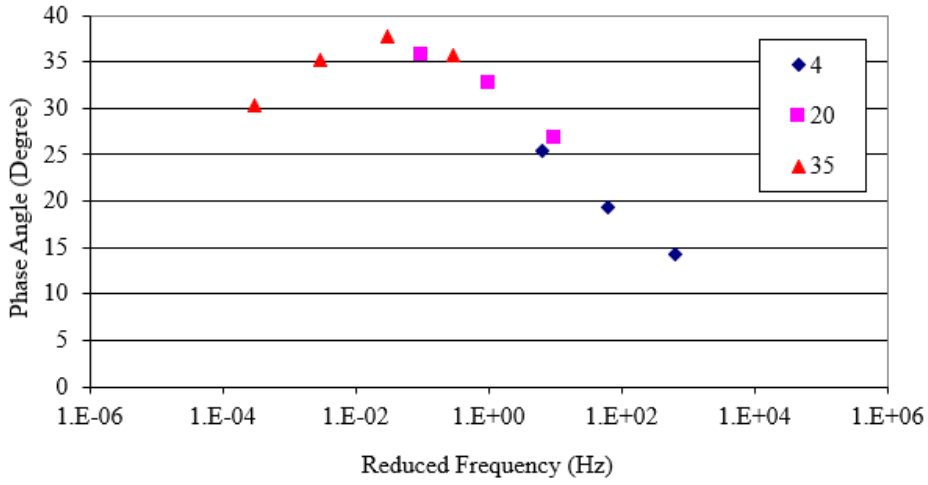

Figure B.3.1. Optimized Phase Angle Master Curve (HWY83_PG58H-34_10%RAP)

Table B.4. HWY6_PG58S-34_25%RAP

	|E*| MEPDG Inputs from Master Curve (ksi)					
Temperature (C)	25 Hz	10 Hz	5 Hz	1 Hz	0.5 Hz	0.1 Hz
-10	2465	2349	2253	1998	1876	1569
4.4	1746	1568	1429	1104	968	679
21.1	810	653	546	342	273	156
37.8	244	177	138	75	58	31
54.4	60	42	33	18	15	9

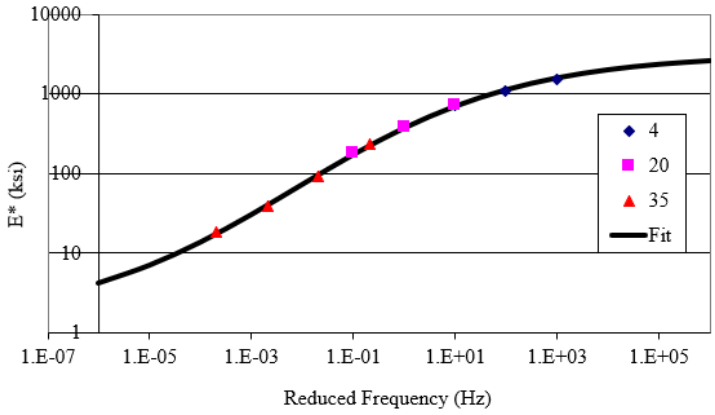

Final Parameters:	Max	3167	ksi
	Min	1.3793	ksi
	Beta	-0.966	
	Gamma	-0.455	
	EA	194029	
Fit	R^2	0.9978	
	Se/Sy	0.0329	

Figure B.4. Optimized |E*| Master Curve (HWY6_PG58S-34_25%RAP)

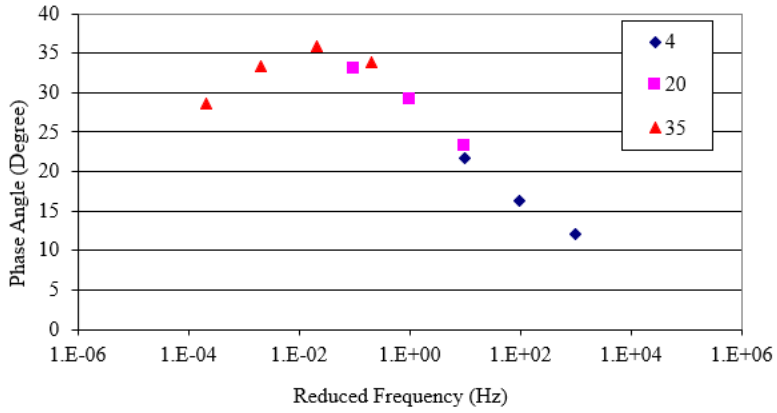

Figure B.4.1. Optimized Phase Angle Master Curve (HWY6_PG58S-34_25%RAP)

Table B.5. HWY28_PG58S-28_0%RAP

	|E*| MEPDG Inputs from Master Curve (ksi)					
Temperature (C)	**25 Hz**	**10 Hz**	**5 Hz**	**1 Hz**	**0.5 Hz**	**0.1 Hz**
-10	2573	2464	2372	2120	1995	1673
4.4	1855	1666	1516	1158	1006	681
21.1	824	648	529	308	237	122
37.8	205	141	104	50	36	18
54.4	38	25	18	9	7	4

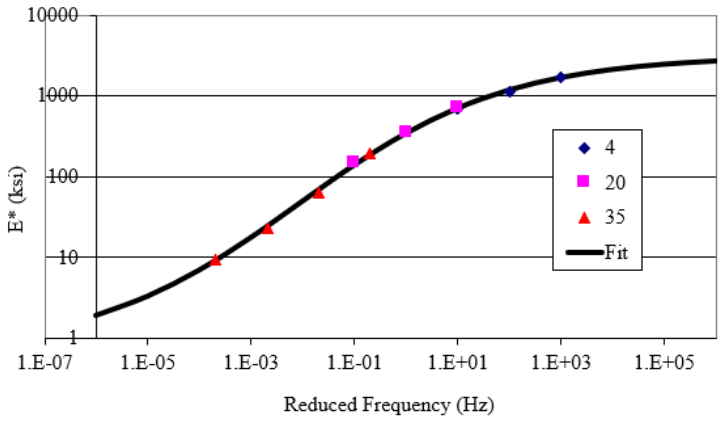

Final Parameters:	Max	3144.3	ksi
	Min	0.7	ksi
	Beta	-1.03700	
	Gamma	-0.50004	
	EA	195143	
Fit	R^2	0.99814	
	Se/Sy	0.0305	

Figure B.5. Optimized |E*| Master Curve (HWY28_PG58S-28_0%RAP)

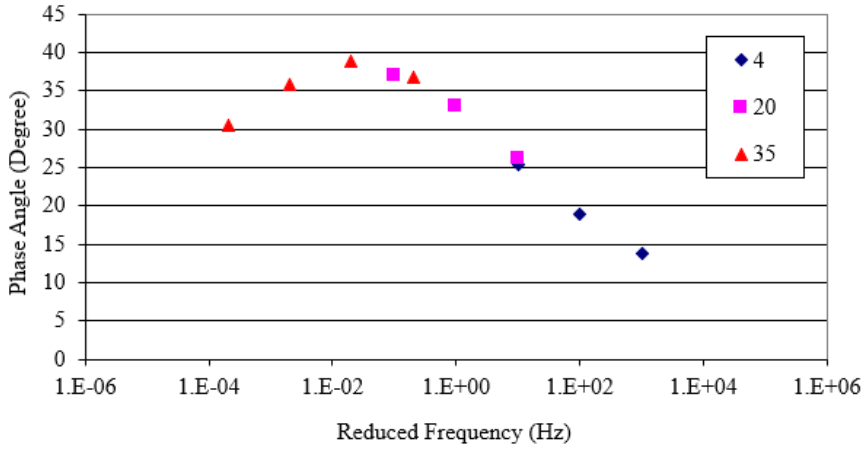

Figure B.5.1. Optimized Phase Angle Master Curve (HWY28_PG58S-28_0%RAP)

Table B.6. HWY1_PG58S-34_15%RAP

	|E*| MEPDG Inputs from Master Curve (ksi)					
Temperature (C)	25 Hz	10 Hz	5 Hz	1 Hz	0.5 Hz	0.1 Hz
-10	2264	2128	2015	1728	1596	1277
4.4	1493	1311	1173	865	743	496
21.1	634	500	411	249	197	111
37.8	185	134	104	57	44	25
54.4	48	35	27	16	13	8

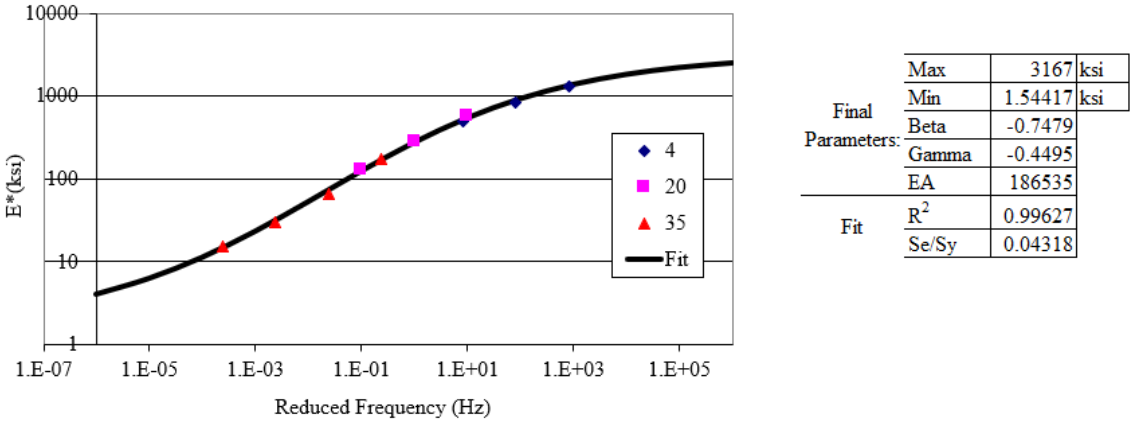

Figure B.6. Optimized |E*| Master Curve (HWY1_PG58S-34_15%RAP)

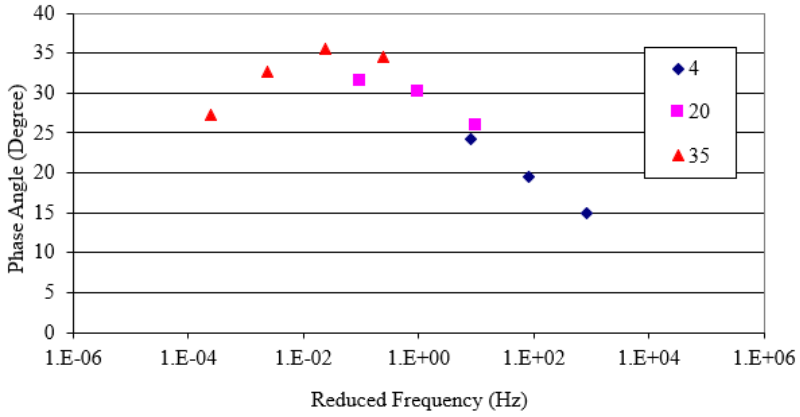

Figure B.6.1. Optimized Phase Angle Master Curve (HWY1_PG58S-34_15%RAP)

Table B.7. HWY52_PG58H-34_0%RAP

	|E*| MEPDG Inputs from Master Curve (ksi)					
Temperature (C)	25 Hz	10 Hz	5 Hz	1 Hz	0.5 Hz	0.1 Hz
-10	2142	1967	1823	1464	1303	938
4.4	1277	1067	914	599	486	282
21.1	450	331	259	141	108	58
37.8	116	82	63	35	28	17
54.4	34	25	20	13	11	8

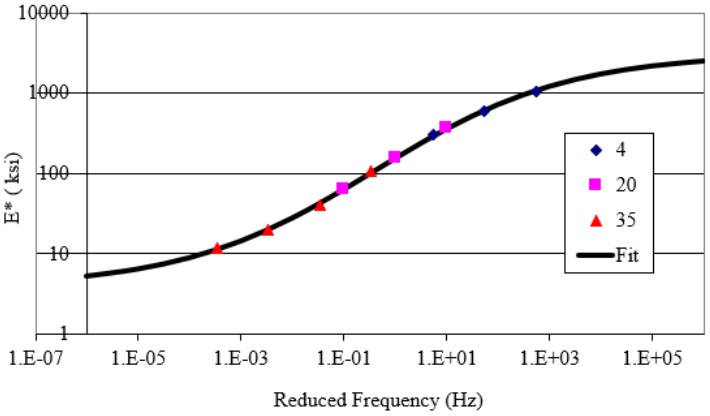

Final Parameters:	Max	3148.14	ksi
	Min	3.90461	ksi
	Beta	-0.204	
	Gamma	-0.536	
	EA	169260	
Fit	R^2	0.99816	
	Se/Sy	0.03036	

Figure B.7. Optimized |E*| Master Curve (HWY52_PG58H-34_0%RAP)

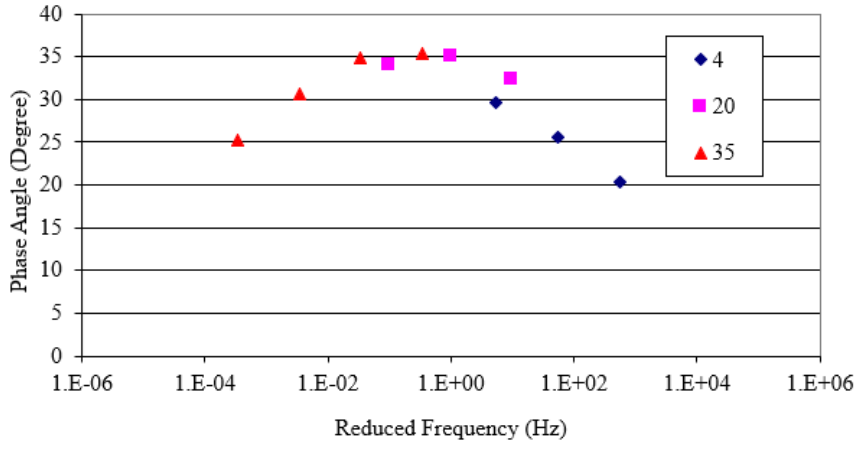

Figure B.7.1. Optimized Phase Angle Master Curve (HWY52_PG58H-34_0%RAP)

Table B.8. HWY35_PG58S-34_20%RAP

	|E*| MEPDG Inputs from Master Curve (ksi)					
Temperature (C)	**25 Hz**	**10 Hz**	**5 Hz**	**1 Hz**	**0.5 Hz**	**0.1 Hz**
-10	2403	2288	2193	1946	1830	1540
4.4	1724	1557	1427	1125	999	725
21.1	867	717	612	406	335	206
37.8	312	237	190	112	89	52
54.4	95	70	55	33	27	17

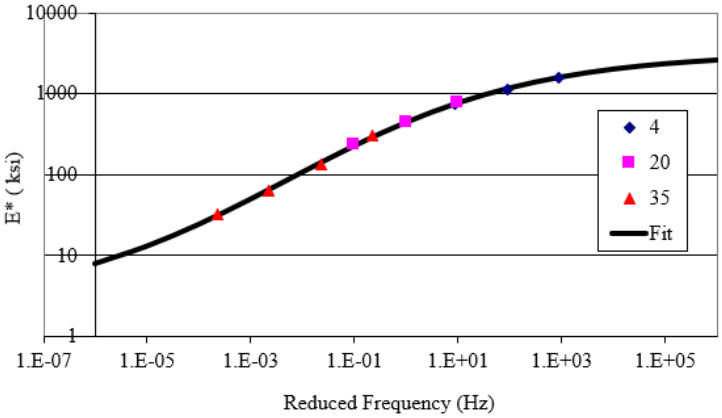

Final Parameters:	Max	3167	ksi
	Min	2.36899	ksi
	Beta	-0.9732	
	Gamma	-0.4279	
	EA	189938	
Fit	R^2	0.99802	
	Se/Sy	0.03143	

Figure B.8. Optimized |E*| Master Curve (HWY35_PG58S-34_20%RAP)

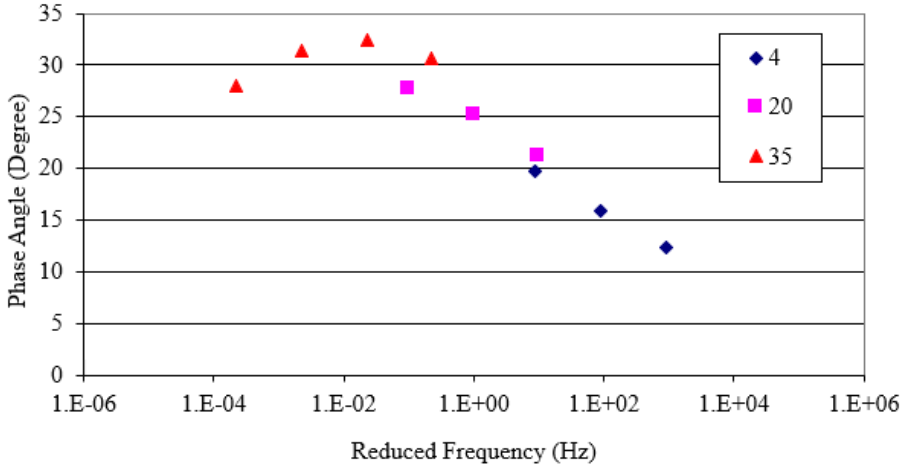

Figure B.8.1. Optimized Phase Angle Master Curve (HWY35_PG58S-34_20%RAP)

Table B.9. HWY6_PG58S-34_20%RAP

	|E*| MEPDG Inputs from Master Curve (ksi)					
Temperature (C)	25 Hz	10 Hz	5 Hz	1 Hz	0.5 Hz	0.1 Hz
-10	2328	2198	2091	1812	1682	1362
4.4	1518	1334	1194	880	754	500
21.1	592	460	374	220	172	94
37.8	145	103	79	42	32	18
54.4	32	23	18	10	8	6

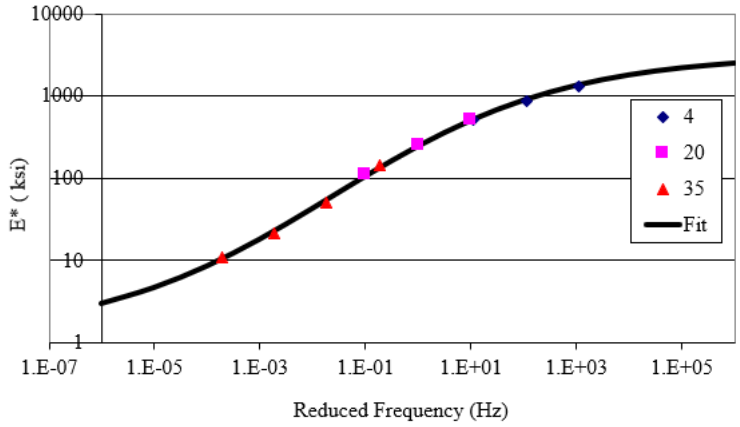

Final Parameters:	Max	3148.14	ksi
	Min	1.20394	ksi
	Beta	-0.7338	
	Gamma	-0.4564	
	EA	199642	
Fit	R^2	0.99676	
	Se/Sy	0.04026	

Figure B.9. Optimized |E*| Master Curve (HWY6_PG58S-34_20%RAP)

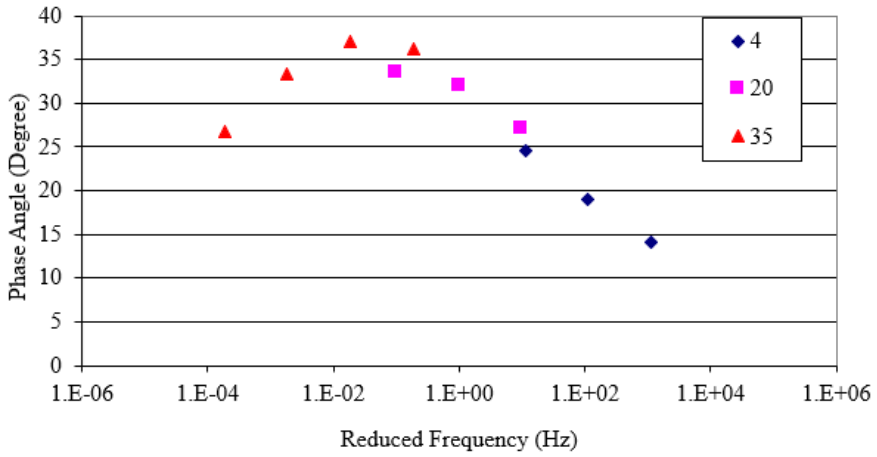

Figure B.9.1. Optimized Phase Angle Master Curve (HWY6_PG58S-34_20%RAP)

Table B.10. I94_PG58H-34_20%RAP

Temperature (C)	|E*| MEPDG Inputs from Master Curve (ksi)					
	25 Hz	10 Hz	5 Hz	1 Hz	0.5 Hz	0.1 Hz
-10	2170	2032	1920	1639	1511	1209
4.4	1376	1204	1075	793	682	459
21.1	555	438	361	222	177	102
37.8	157	115	90	51	40	23
54.4	41	30	24	14	12	8

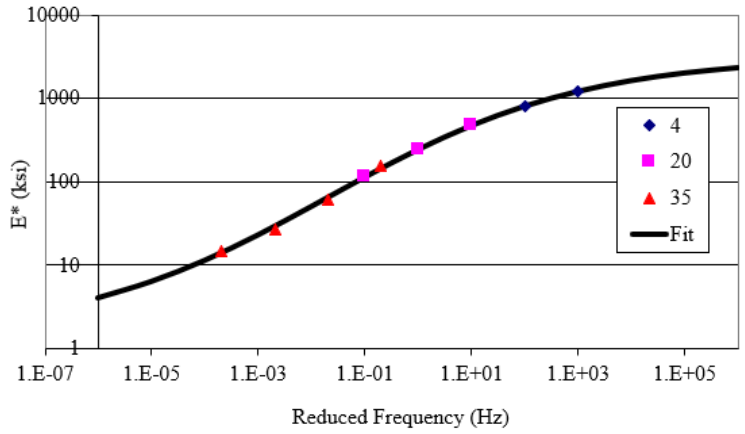

Final Parameters:	Max	3185.48	ksi
	Min	1.3518	ksi
	Beta	-0.7037	
	Gamma	-0.4205	
	EA	195008	
Fit	R^2	0.99699	
	Se/Sy	0.03877	

Figure B.10. Optimized |E*| Master Curve (I94_PG58H-34_20%RAP)

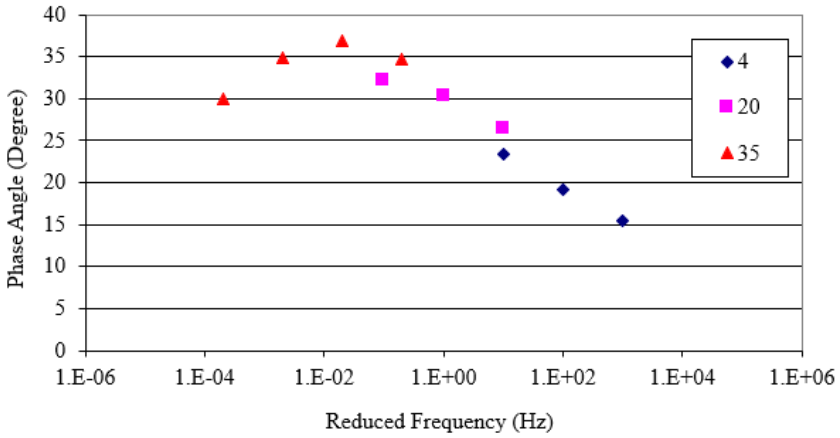

Figure B.10.1. Optimized Phase Angle Master Curve (I94_PG58H-34_20%RAP)

Appendix C: Creep Compliance

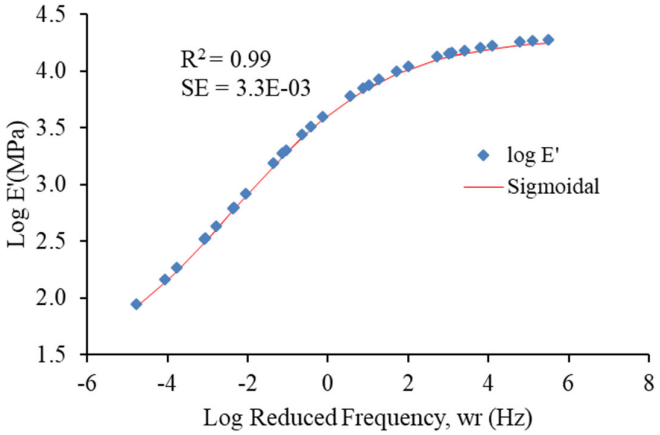

$$logE'(wr) = 4.30 - \frac{3.047}{(1 + \exp(1.226 + 0.522logwr)}$$

Figure C.1.2. Predicted E(t) Master Curve and Sigmoidal Fitting Curve (HWY32_PG58S-28_15%RAP)

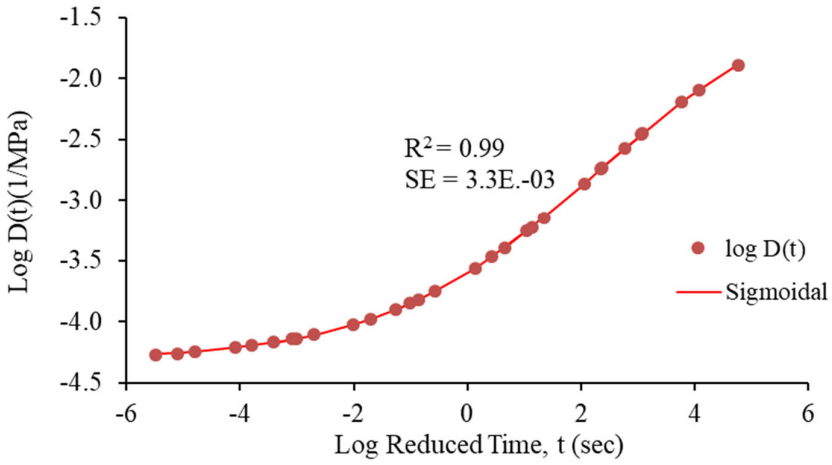

$$logD(t) = -4.321 - \frac{3.09}{(1 + \exp(1.193 - 0.525logt)}$$

Figure C.1.3. Predicted D(t) Master Curve and Sigmoidal Fitting Curve (HWY32_PG58S-28_15%RAP)

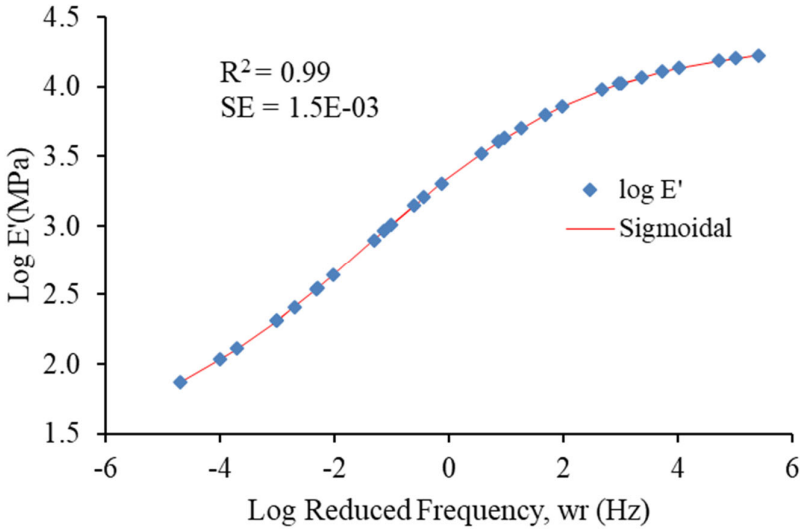

$$logE'(wr) = 4.33 - \frac{2.974}{(1 + \exp(0.709 + 0.484 logwr)}$$

Figure C.2.1. E' Master Curve and Sigmoidal Fitting Curve (HWY32_PG58H-34_15%RAP)

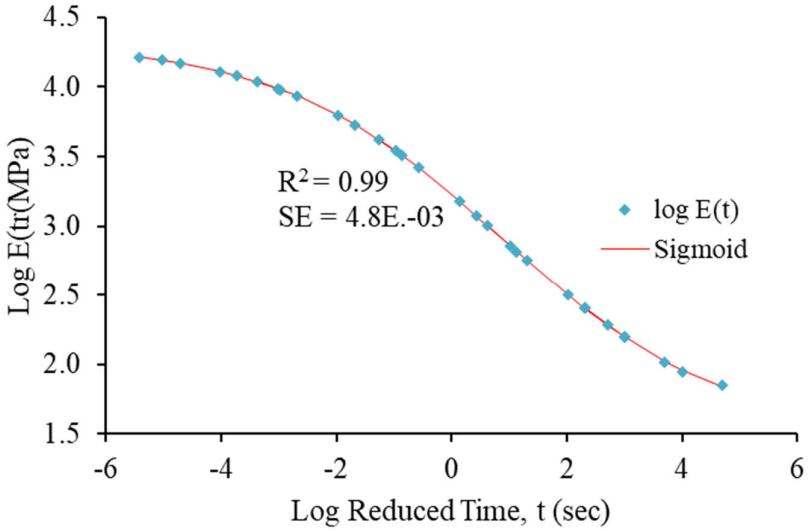

$$logE(t) = 1.492 + \frac{2.822}{(1 + \exp(-0.468 + 0.522 logt)}$$

Figure C.2.2. Predicted E(t) Master Curve and Sigmoidal Fitting Curve (HWY32_PG58H-34_15%RAP)

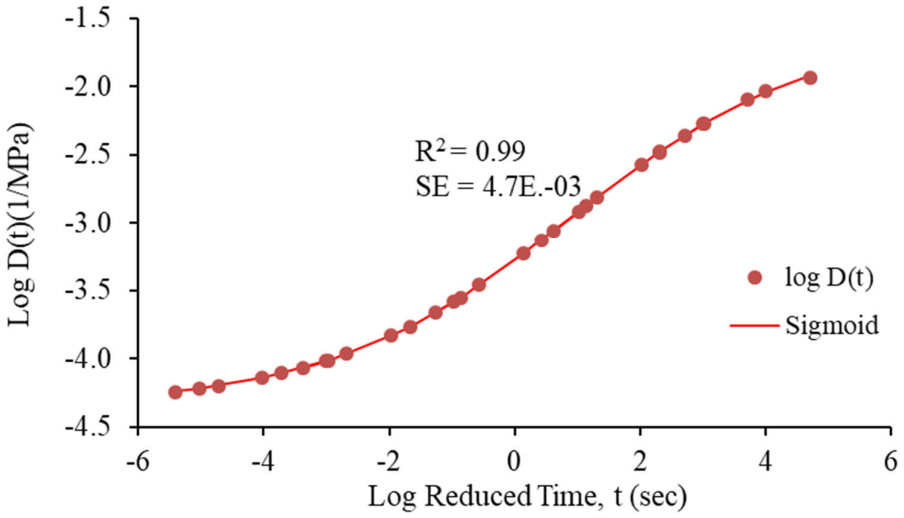

$$logD(t) = -4.339 - \frac{2.75}{(1 + \exp(0.463 - 0.52logt)}$$

Figure C.2.3. Predicted D(t) Master Curve and Sigmoidal Fitting Curve (HWY32_PG58H-34_15%RAP)

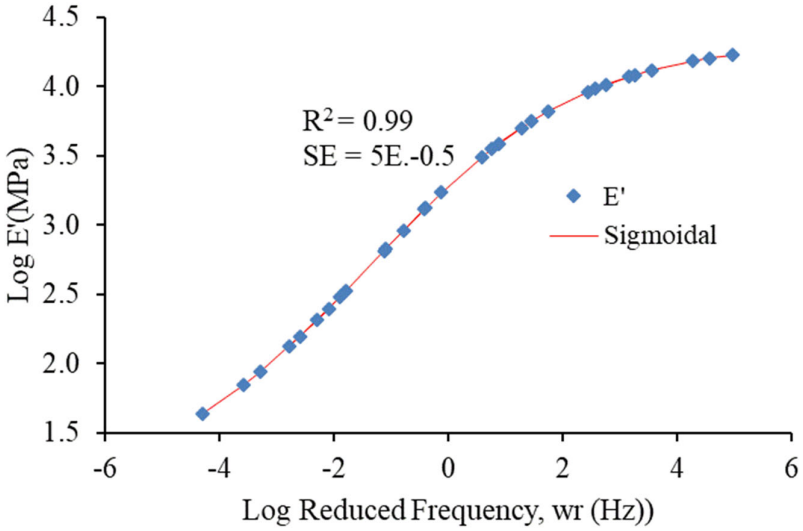

$$logE'(wr) = 4.334 - \frac{3.246}{(1 + \exp(0.733 + 0.537logwr)}$$

Figure C.1.1. E' Master Curve and Sigmoidal Fitting Curve (HWY32_PG58S-28_15%RAP)

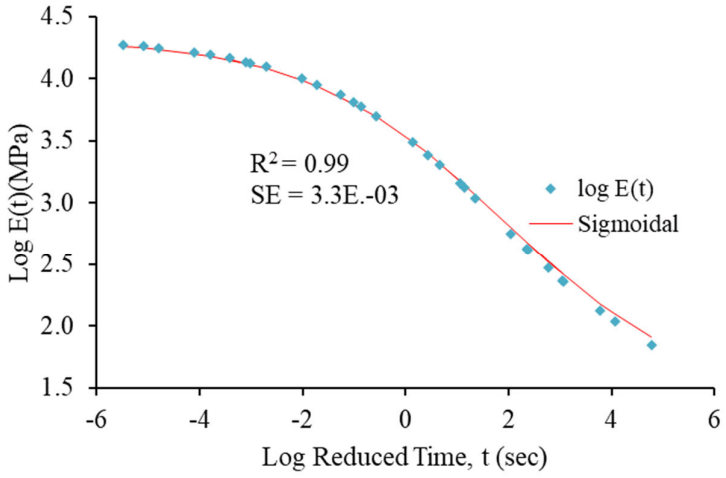

$$logE(t) = 1.371 + \frac{2.95}{(1 + \exp(-1.011 + 0.524logt)}$$

Figure C.3.1. E' Master Curve and Sigmoidal Fitting Curve (HWY83_PG58H-34_25%RAP)

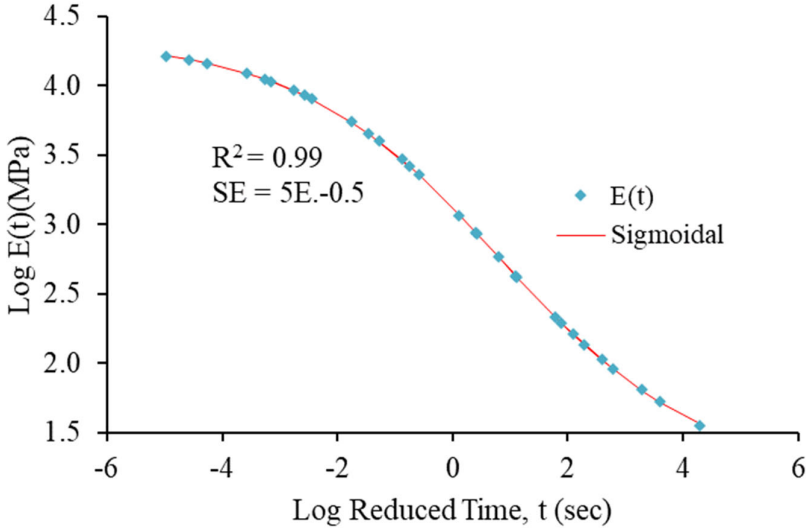

$$logE(t) = 1.186 + \frac{3.137}{(1 + \exp(-0.473 + 0.572logt)}$$

Figure C.3.2. E(t) Master Curve and Sigmoidal Fitting Curve (HWY83_PG58H-34_25%RAP)

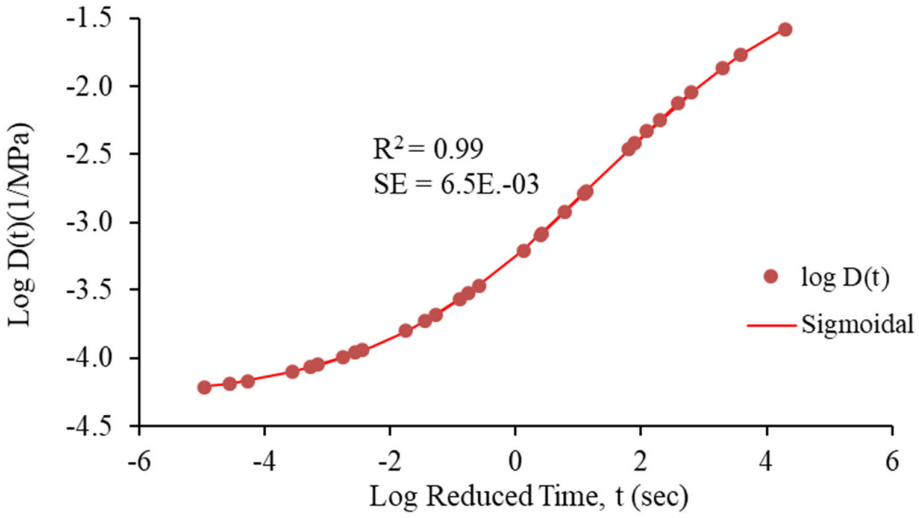

$$logD(t) = -4.306 - \frac{3.262}{(1 + \exp(0.733 - 0.533logt)}$$

Figure C.3.3. Predicted D(t) Master Curve and Sigmoidal Fitting Curve (HWY83_PG58H-34_25%RAP)

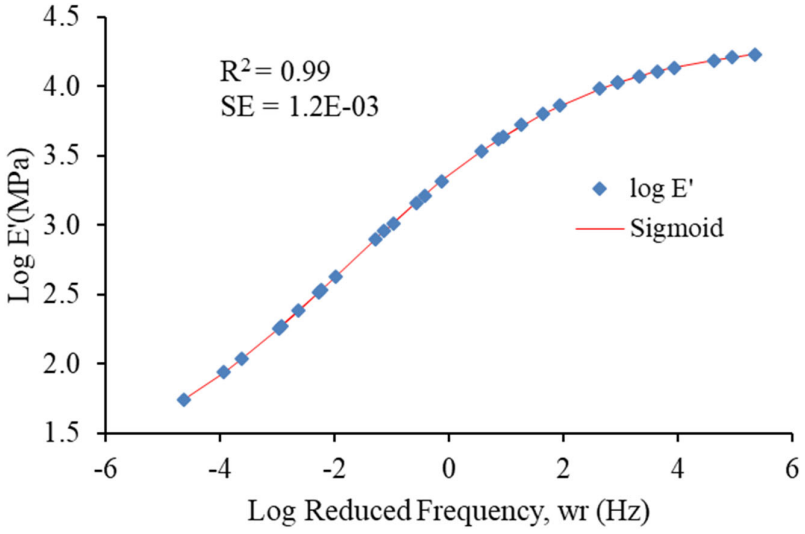

$$logE'(wr) = 4.333 - \frac{3.232}{(1 + \exp(0.843 + 0.48logwr)}$$

Figure C.4.1. E' Master Curve and Sigmoidal Fitting Curve (HWY6_PG58S-34_25%RAP)

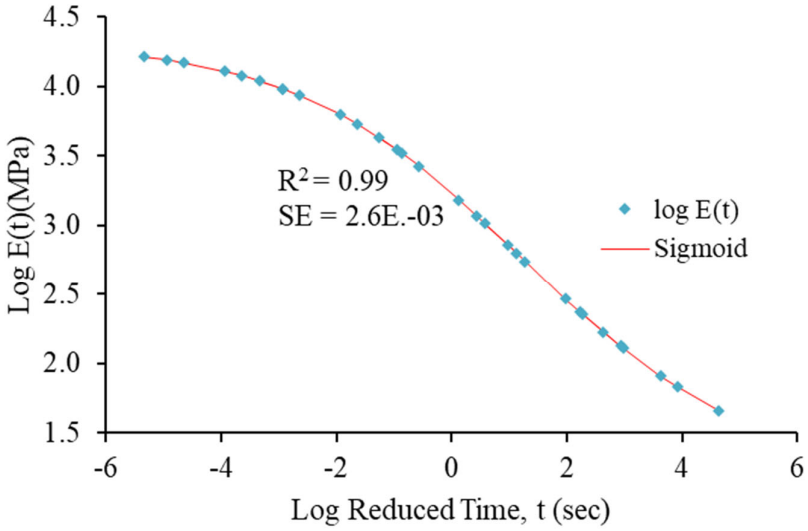

$$logE(t) = 1.186 + \frac{3.138}{(1 + \exp(-0.628 + 0.505logt)}$$

Figure C.4.2. E(t) Master Curve and Sigmoidal Fitting Curve (HWY6_PG58S-34_25%RAP)

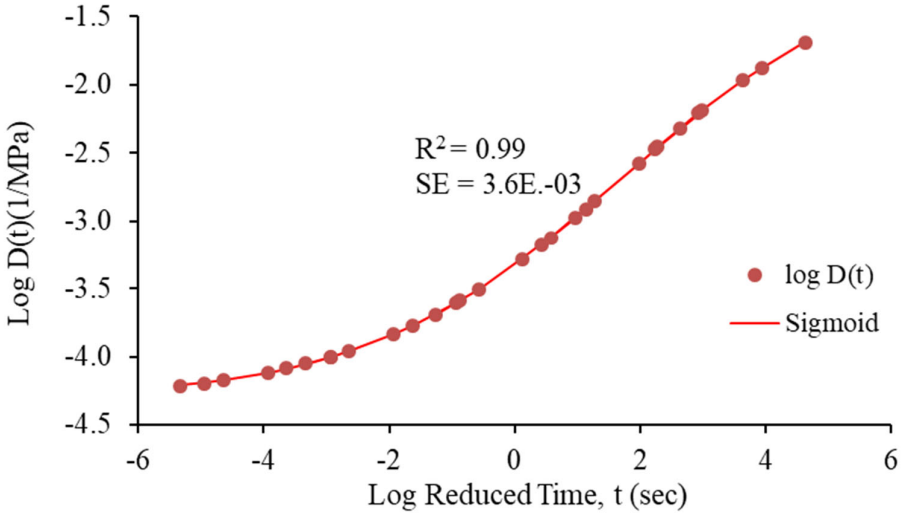

Figure C.4.3. D(t) Master Curve and Sigmoidal Fitting Curve (HWY6_PG58S-34_25%RAP)

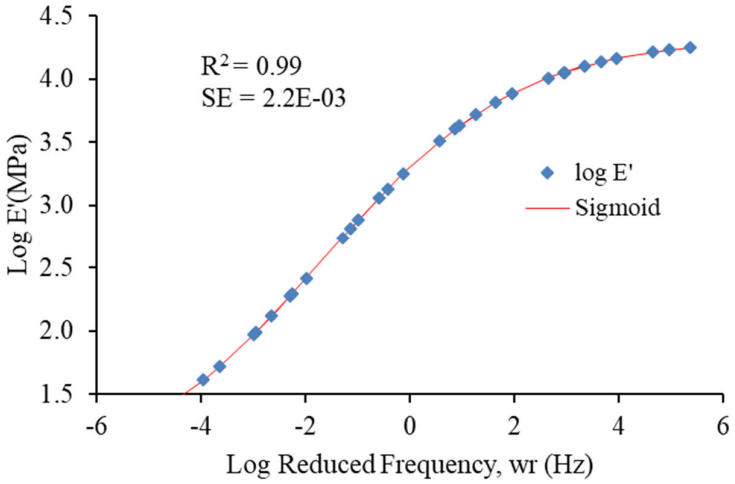

$$logE'(wr) = 4.333 - \frac{3.232}{(1 + \exp(0.843 + 0.48logwr)}$$

Figure C.5.1. E' Master Curve and Sigmoidal Fitting Curve (HWY28_PG58S-28_0%RAP)

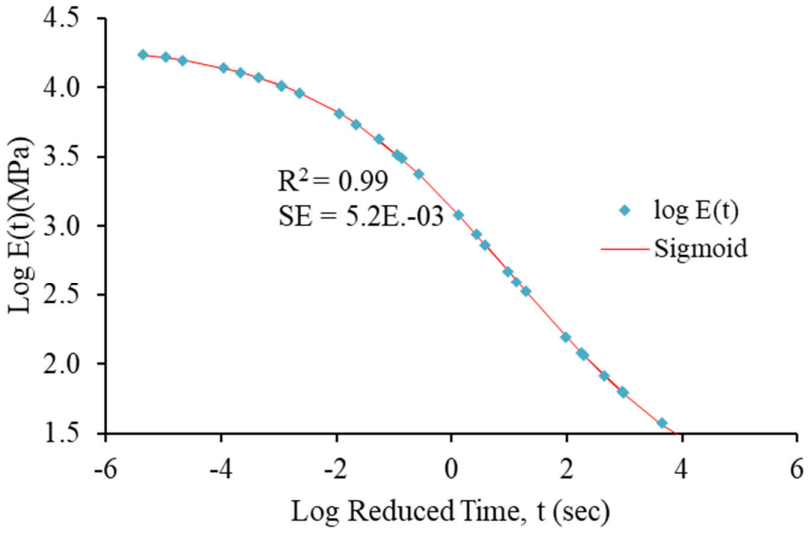

$$logE(t) = 1.186 + \frac{3.138}{(1 + \exp(-0.628 + 0.505logt)}$$

Figure C.5.2. E(t) Master Curve and Sigmoidal Fitting Curve (HWY28_PG58S-28_0%RAP)

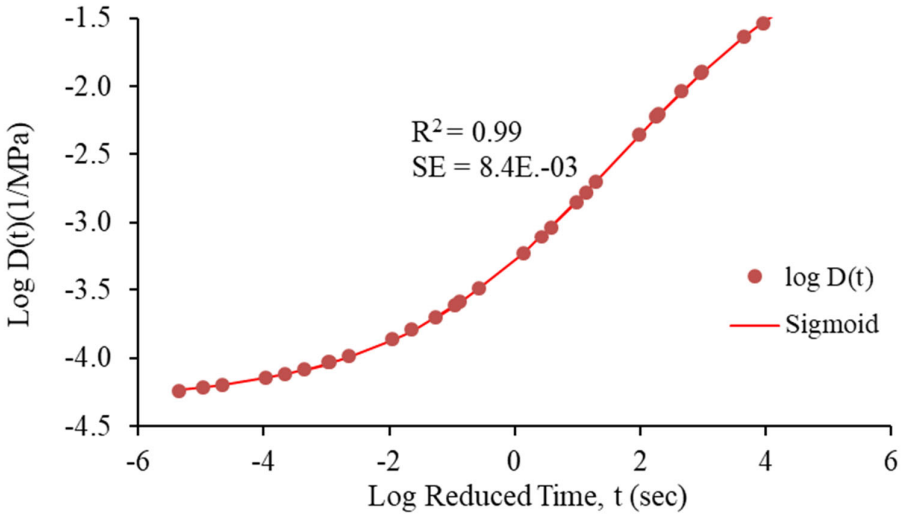

Figure C.5.3. D(t) Master Curve and Sigmoidal Fitting Curve (HWY28_PG58S-28_0%RAP)

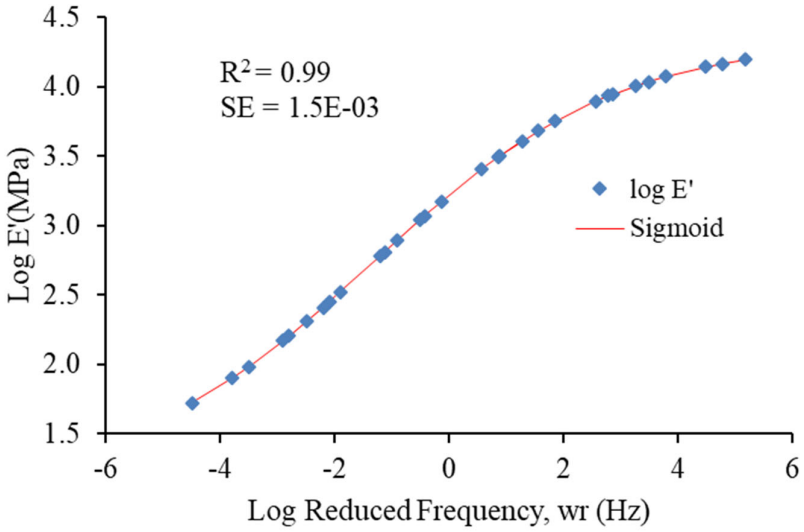

$$logE'(wr) = 1.135 + \frac{3.2}{(1 + \exp(-0.622 - 0.471 logwr)}$$

Figure C.6.1. E' Master Curve and Sigmoidal Fitting Curve (HWY1_PG58S-34_15%RAP)

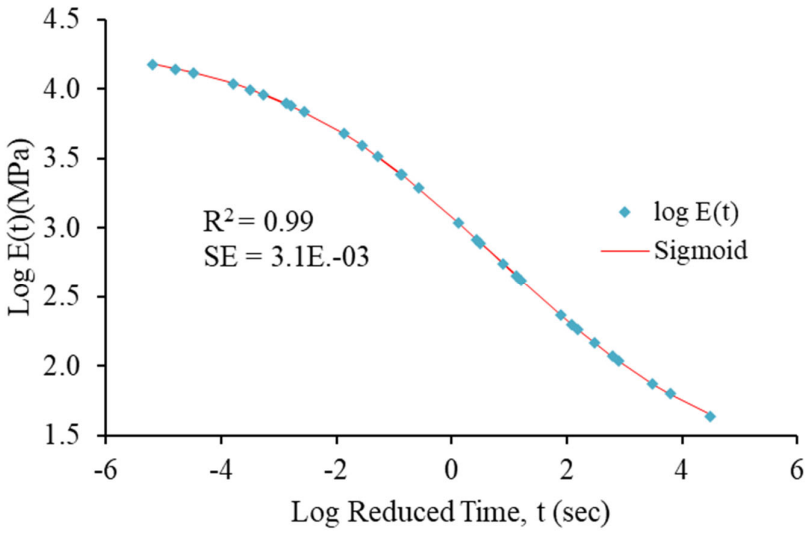

$$logE(t) = 1.211 + \frac{3.117}{(1 + \exp(-0.405 + 0.493logt)}$$

Figure C.6.2. E(t) Master Curve and Sigmoidal Fitting Curve (HWY1_PG58S-34_15%RAP)

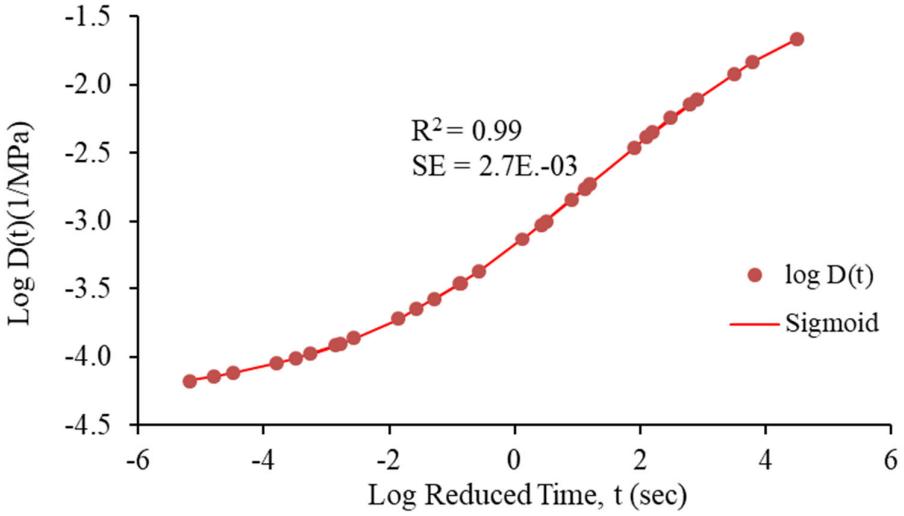

$$logD(t) = -4.312 - \frac{3.212}{(1 + \exp(0.605 - 0.48logt)}$$

Figure C.6.3. D(t) Master Curve and Sigmoidal Fitting Curve (HWY1_PG58S-34_15%RAP)

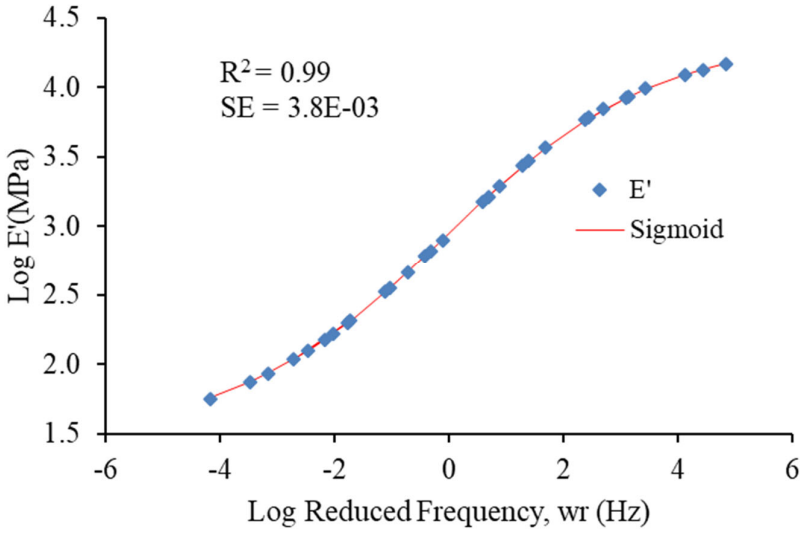

$$logE'(wr) = 1.495 + \frac{2.853}{(1 + \exp(-0.0416 - 0.55logwr)}$$

Figure C.7.1. E' Master Curve and Sigmoidal Fitting Curve (HWY52_PG58H-34_0%RAP)

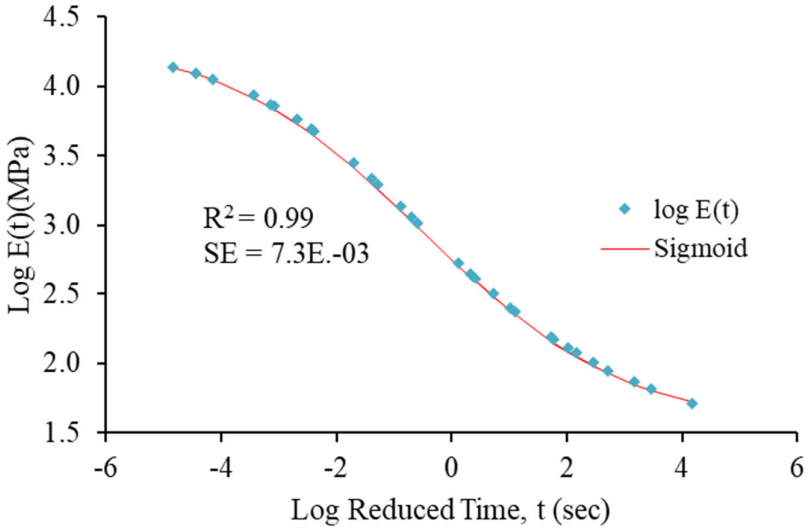

$$logE(t) = 1.542 + \frac{2.809}{(1 + \exp(0.278 + 0.574logt)}$$

Figure C.7.2. E(t) Master Curve and Sigmoidal Fitting Curve (HWY52_PG58H-34_0%RAP)

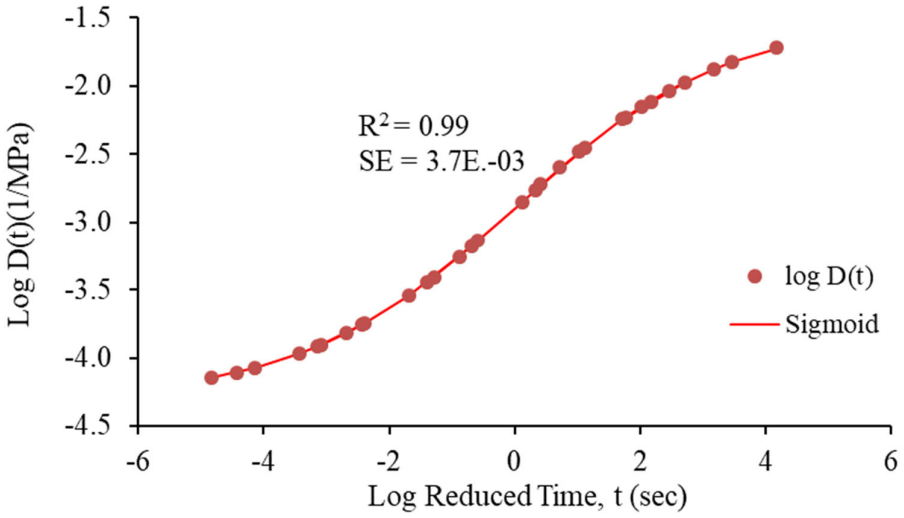

$$logD(t) = -1.51 - \frac{2.787}{(1 + \exp(0.0073 + 0.48logt)}$$

Figure C.7.3. D(t) Master Curve and Sigmoidal Fitting Curve (HWY52_PG58H-34_0%RAP)

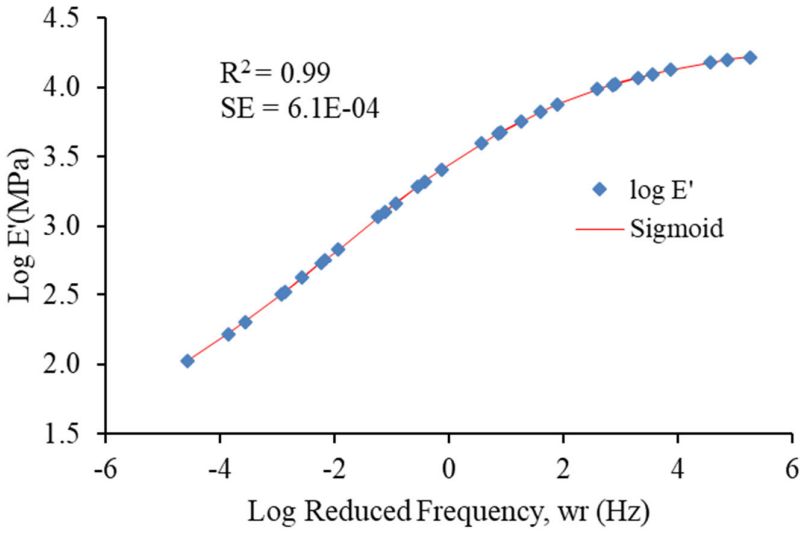

$$logE'(wr) = 1.495 + \frac{2.853}{(1 + \exp(-0.0416 - 0.55logwr)}$$

Figure C.8.1. E' Master Curve and Sigmoidal Fitting Curve (HWY35_PG58H-34_20%RAP)

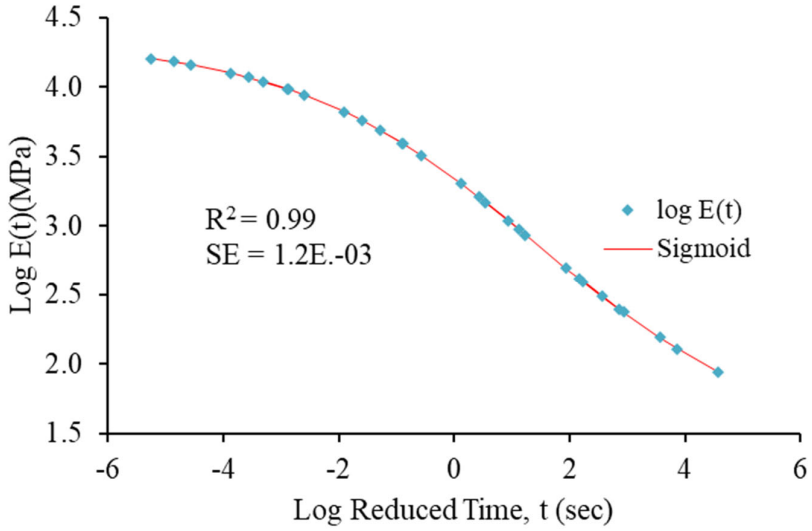

$$logE(t) = 1.542 + \frac{2.809}{(1 + \exp(0.278 + 0.574logt)}$$

Figure C.8.2. E(t) Master Curve and Sigmoidal Fitting Curve (HWY35_PG58H-34_20%RAP)

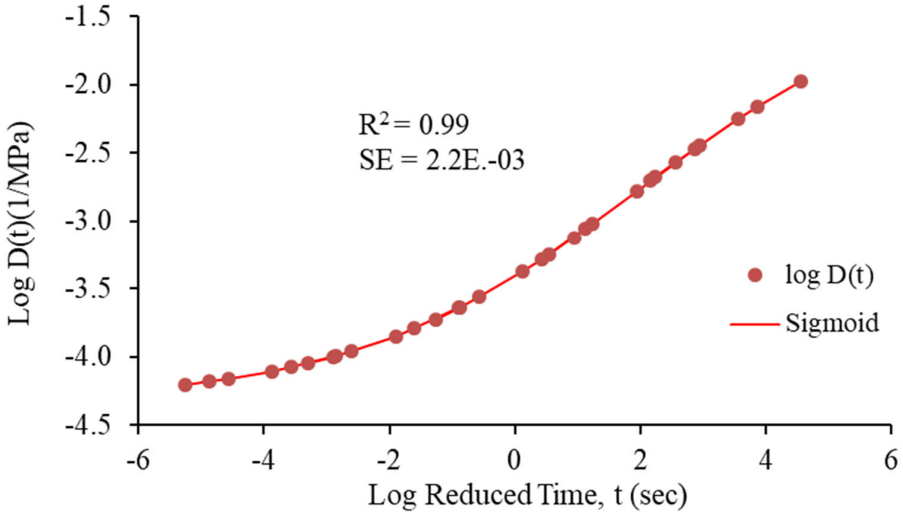

$$logD(t) = -1.51 - \frac{2.787}{(1 + \exp(0.0073 + 0.48logt)}$$

Figure C.8.3. D(t) Master Curve and Sigmoidal Fitting Curve (HWY35_PG58H-34_20%RAP)

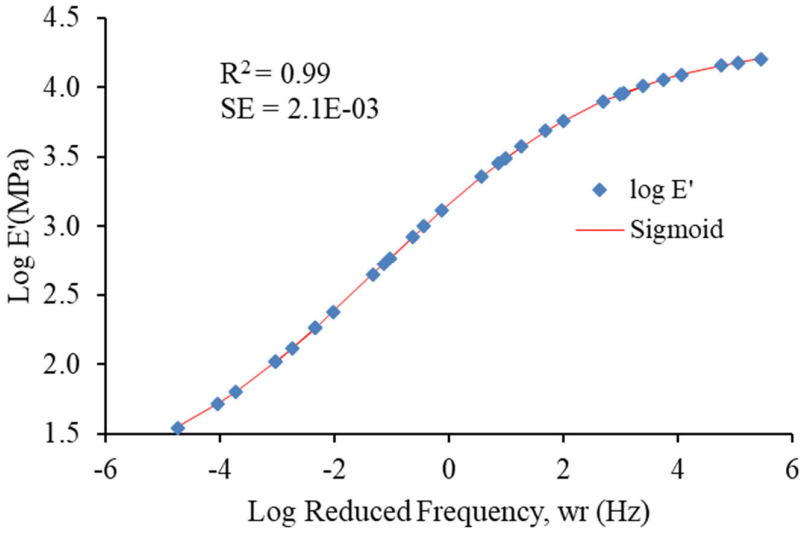

$$logE'(wr) = 1.495 + \frac{2.853}{(1 + \exp(-0.0416 - 0.55 logwr)}$$

Figure C.9.1. E' Master Curve and Sigmoidal Fitting Curve (HWY6_PG58S-34_20%RAP)

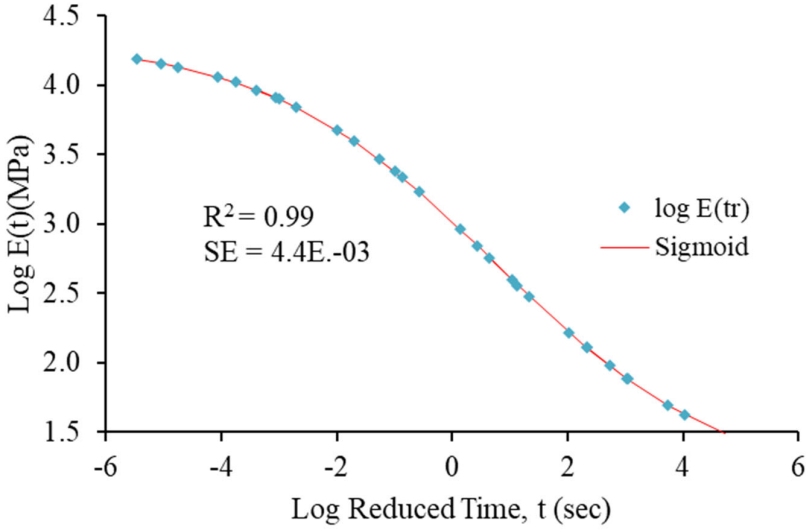

$$logE(t) = 1.542 + \frac{2.809}{(1 + \exp(0.278 + 0.574 logt)}$$

Figure C.9.2. E(t) Master Curve and Sigmoidal Fitting Curve (HWY6_PG58S-34_20%RAP)

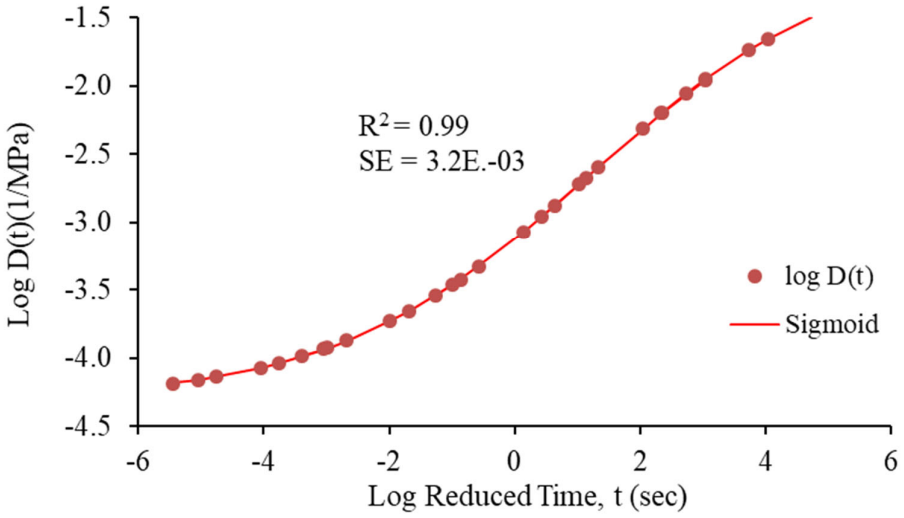

$$logD(t) = -1.51 - \frac{2.787}{(1 + \exp(0.0073 + 0.48logt)}$$

Figure C.9.3. D(t) Master Curve and Sigmoidal Fitting Curve (HWY6_PG58S-34_20%RAP)

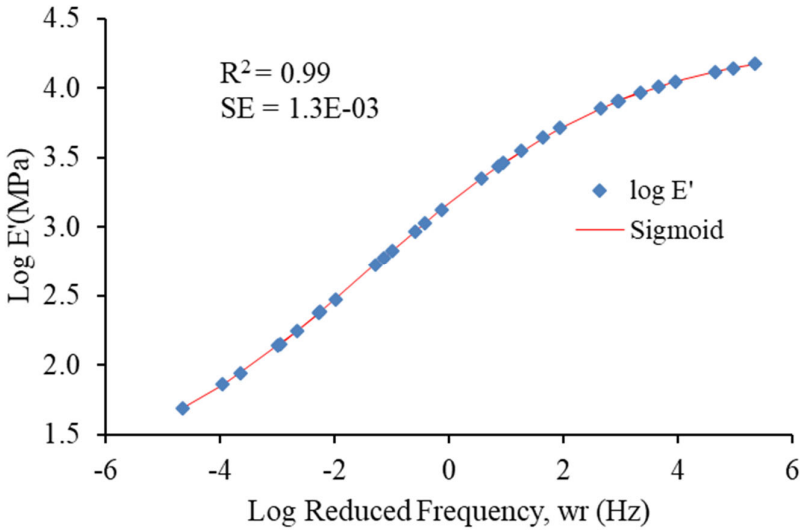

$$logE'(wr) = 1.068 + \frac{3.27}{(1 + \exp(-0.589 - 0.438logwr)}$$

Figure C.10.1. E' Master Curve and Sigmoidal Fitting Curve (I-94_PG58H-34_0%RAP)

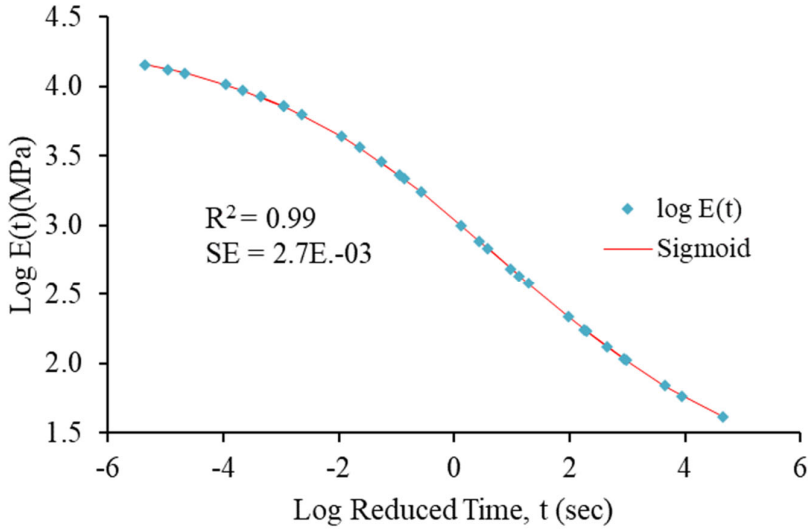

$$logE(t) = 1.139 + \frac{3.193}{(1 + \exp(-0.39 + 0.456logt)}$$

Figure C.10.2. E(t) Master Curve and Sigmoidal Fitting Curve (I-94_PG58H-34_0%RAP)

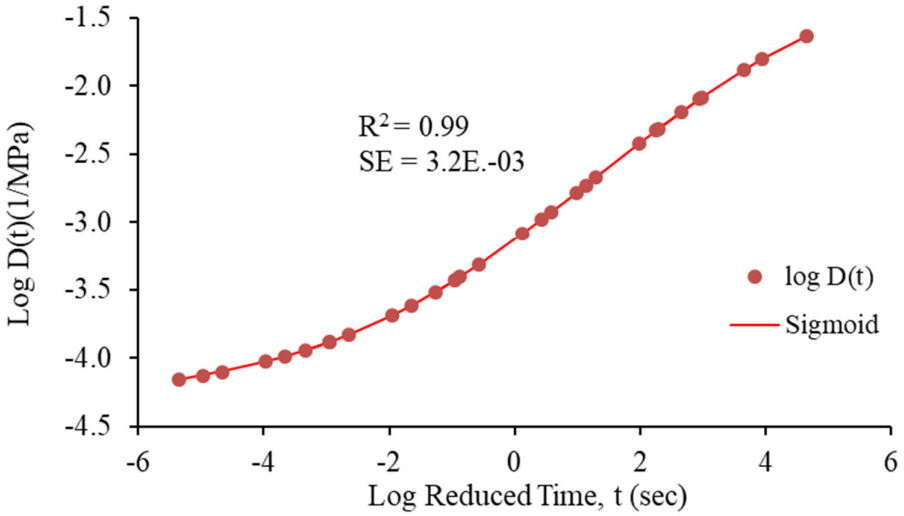

$$logD(t) = -4.318 - \frac{3.283}{(1 + \exp(0.568 - 0.444logt)}$$

Figure C.10.3. D(t) Master Curve and Sigmoidal Fitting Curve (I-94_PG58H-34_0%RAP)